

Bridging the Gap Between Safety and Real-Time Performance in Receding-Horizon Trajectory Design for Mobile Robots

Shreyas Kousik*, Sean Vaskov*, Fan Bu, Matthew Johnson-Roberson, Ram Vasudevan

October 11, 2024

Abstract

Autonomous mobile robots must operate with limited sensor horizons in unpredictable environments. To do so, they use a receding-horizon strategy to plan trajectories, by executing a short plan while creating the next plan. However, creating safe, dynamically-feasible trajectories in real time is challenging; and, planners must ensure that they are persistently feasible, meaning that a new trajectory is always available before the previous one has finished executing. Existing approaches make a tradeoff between model complexity and planning speed, which can require sacrificing guarantees of safety and dynamic feasibility. This work presents the Reachability-based Trajectory Design (RTD) method for trajectory planning. RTD begins with an offline Forward Reachable Set (FRS) computation of a robot’s motion while it tracks parameterized trajectories; the FRS also provably bounds tracking error. At runtime, the FRS is used to map obstacles to the space of parameterized trajectories, which allows RTD to select a safe trajectory at every planning iteration. RTD prescribes a method of representing obstacles to ensure that these constraints can be created and evaluated in real time while maintaining provable safety. Persistent feasibility is achieved by prescribing a minimum duration of planned trajectories, and a minimum sensor horizon. A system decomposition approach is used to increase the dimension of the parameterized trajectories in the FRS, allowing for RTD to create more complex plans at runtime. RTD is compared in simulation with Rapidly-exploring Random Trees (RRT) and Nonlinear Model-Predictive Control (NMPC). RTD is also demonstrated on two hardware platforms in randomly-crafted environments: a differential-drive Segway, and a car-like Rover. The proposed method is shown as safe and persistently feasible across thousands of simulations and dozens of hardware demos.

1 INTRODUCTION

Autonomous mobile robots, such as autonomous cars, unmanned ground vehicles, and drones, are required to operate in unpredictable environments with limited sensor horizons. To do so, they typically employ a receding-horizon strategy, wherein the robot simultaneously plans a short trajectory, then executes it while planning a subsequent trajectory. This strategy is necessary because the robot receives new sensor information as it moves through the environment. To successfully perform receding-horizon planning, the robot must guarantee safety and persistent feasibility. Planning is safe if the robot avoids collision with obstacles in the environment while executing a planned trajectory. Planning is persistently feasible if there always exists a safe trajectory or stopping maneuver before the robot completes executing the previously-planned trajectory. Therefore, the receding horizon strategy imposes a real-time requirement on trajectory planning, because the time required to generate a plan is less than or equal to the duration of the plan.

To address the requirements of safety and persistent feasibility, a three level hierarchical control architecture is often used [2, 8, 15, 16]. The high-level planner performs coarse route planning on a map using, e.g., Dijkstra’s algorithm. To construct paths rapidly, the high-level planner does not use a dynamic model of the robot and, as a result, does not make any safety guarantees. The low-level planner translates kinematic commands into torques or forces, such as transforming a velocity profile into pulse-width modulated (PWM) signal for a drive motor. This level is not concerned with the robot’s environment, and real-time applications of these controllers are widely used

This work is supported by the Ford Motor Company via the Ford-UM Alliance under award N022977; the National Science Foundation under Contract CNS-1239037; and by the Office of Naval Research under Award Number N00014-18-1-2575.

* These authors contributed equally to this work.

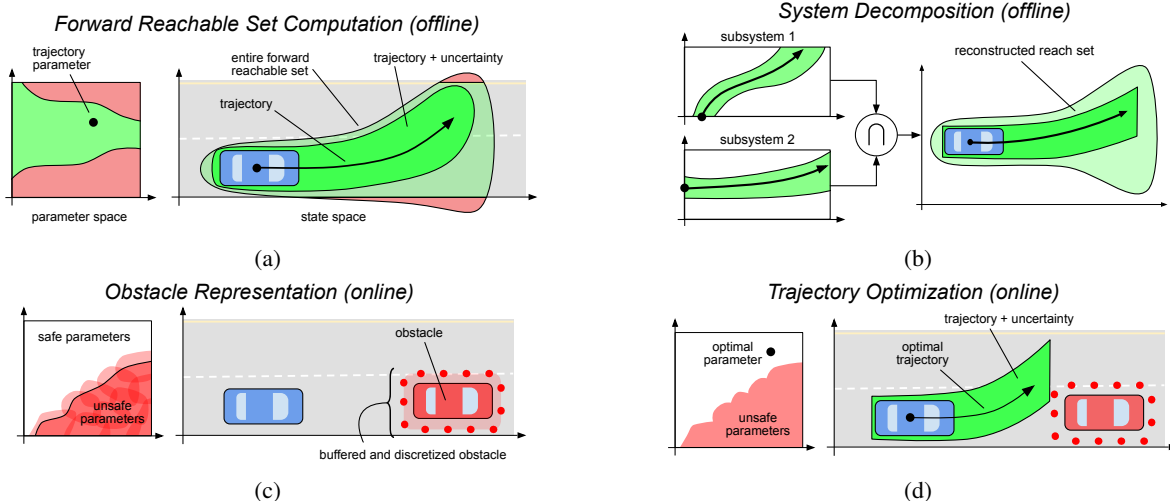


Figure 1: An illustration of the contributions of this paper. Figure 1a shows a parameterized trajectory space on the left, and the state space of the mobile robot (blue car) on the right. The bell-shaped contour on the right is the forward reachable set (FRS) corresponding to the robot attempting to track any trajectory from the parameter space. The red sections of the contour are unsafe areas, and are shown as corresponding red trajectory parameters on the left. A single trajectory parameter is chosen on the left, and is shown as a trajectory in the state space, plus the uncertainty in the robot’s model, which results in a subset of the FRS corresponding to that parameter. The proposed method extends the existing RTD method from [22] to higher-dimensional systems via a system decomposition approach adapted from [3, 4], shown in Figure 1b. For the online computation, this paper presents a method of representing obstacles discretely (Figure 1c) that allows real-time computation without sacrificing safety in Section 6. Each point in the discretized obstacle representation is mapped to the subset of all trajectory parameters that could cause the robot to reach that point. At run-time, this mapping is expressed as a finite list of nonlinear constraints for online trajectory optimization (Figure 1d), which enables real-time operation. The unsafe parameters corresponding to the discretization are a superset of the exact set of unsafe parameters corresponding to the red obstacle. Therefore, the discretized representation defines the feasible trajectory parameter space and ensures that the online trajectory optimization is safe as we prove in Section 6.4. These two contributions enable provably safe, real-time trajectory planning (Figure 1d) in Section 7.

and well-studied. The mid-level planner, called a trajectory planner, is the focus of this paper. Trajectory planners take in high-level route guidance and local environmental constraints (e.g. walls, other robots, lane boundaries), and deliver commands to the low-level planner to navigate the desired route. Typically, since the trajectory planner uses knowledge of both the environment and a robot’s dynamic model, it is relied upon for planning obstacle-avoidance maneuvers in real time. In this work, we propose a trajectory planner that is both safe and persistently feasible.

We now briefly discuss existing methods to show that, to the best of our knowledge, no trajectory planner has been shown to be safe and persistently feasible in static environments with arbitrary obstacle configuration and geometry. A trajectory planner must fulfill several characteristics to meet these requirements. It must produce dynamically feasible trajectories to ensure that the robot can actually execute a plan. It must be robust to model uncertainty of the dynamic model to ensure that a trajectory that is expected to be safe is actually safe. And, it must be able to generate solutions in real-time. Several general classes of methods, such as sample-based planning, model predictive control, or reachability-based planning, exist to address these requirements.

Sample-based methods use a temporal and/or spatial discretization of a robot’s dynamic model [6]. These methods plan trajectories by drawing samples from a robot’s control input and/or state space, and can be provably asymptotically optimal [21], though such optimality may not be critical to ensure safety or real-time performance. A widely-used example that can find feasible plans quickly is the Rapidly-exploring Random Tree (RRT) algorithm, which plans trajectories by sampling the control input space or the state space to generate nodes and grow a tree that explores the state space. To generate edges between nodes while ensuring dynamic feasibility, an RRT must either have an explicit solution for a robot’s trajectory, which is possible for some kinematic models; or must numerically integrate a dynamic model [25]. Nodes, or linearized edges between nodes, are checked for collisions with obstacles in the environment. Since dynamic models typically only represent a robot’s center of mass dynamics, obstacles in the environment must be buffered to compensate for the robot’s entire body [6]. RRT methods can compensate for uncertainty by increasing the obstacle buffer size, and, if the robot’s dynamics are linear, by propagating forward a Gaussian distribution

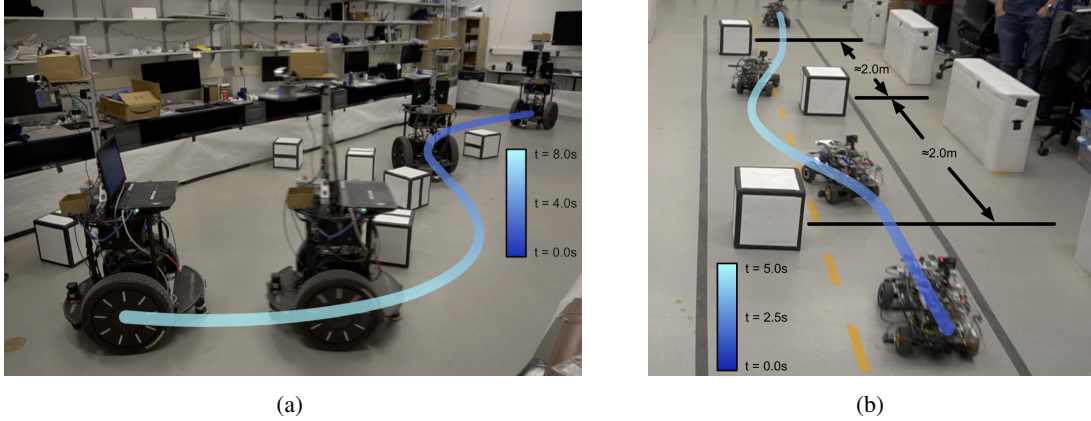


Figure 2: Example trajectories demonstrating RTD on two hardware platforms: the differential-drive Segway in Figure 2a and the car-like Rover in Figure 2b. The Segway travels at up to 1.25 m/s around box obstacles distributed randomly around a rectangular room. The Rover travels at 1.5 m/s on a mock road with randomly spaced box obstacles. Both use a planar lidar to sense the obstacles in real time. The Segway replans its trajectory every 0.5 s, and the Rover every 0.375 s, using Algorithm 2 from Section 7. Both robots safely traverse their respective scenarios despite error in each robot’s ability to track planned trajectories. Videos of the robots are available at <https://youtu.be/FJns7YpdMXQ> for the Segway and https://youtu.be/bgDEAi_Ewfw for the Rover.

of the robot’s location to check for obstacle collision [28]. When using receding-horizon planning, uncertainty can be mitigated by repropagating the tree from the robot’s current position each time step [23]. To achieve real-time performance, a balance must be struck between the dimensionality of the dynamic model, the number of obstacles considered, and the discretization fineness, which is typically done by applying a heuristic [6, 23]. The representation of constraints, in particular, to attempt to ensure real-time performance and persistent feasibility, such as a minimum time horizon or distance, are easy to check, but may impact an RRT’s performance. Persistent feasibility has been demonstrated by planning both a stopping and desired trajectory at each iteration [23]; however, planning the stopping trajectory requires additional computation and still suffers from the above trade-offs. Other sampling-based methods, such as the Fast Marching Tree (FMT), can operate in real time in high-dimensional configuration spaces [19]. However this method relies on drawing samples from the state-space. In real-time applications the dynamic feasibility of edges connecting these nodes is not enforced; hence guarantees of collision avoidance cannot be made.

Nonlinear Model Predictive Control (NMPC) methods plan trajectories by formulating an optimization program over a robot’s control inputs, with the dynamics and obstacles treated as constraints [7, 8]. The dynamics of a single point, commonly the center of mass, are represented in constraints via numerical integration and/or polynomial approximation. Obstacle avoidance is achieved by checking if the discrete points lie within a polygon or ellipse that buffers the obstacle. The discretization fineness affects both the dynamic feasibility and safety of the solution, which is an unideal tradeoff since decreasing the step size increases computation time [38]. Real-time applications of NMPC rely on precomputing a dynamically feasible reference trajectory, linearizing the robot’s dynamics, and/or exploiting the structure of the environment, which can all be difficult to pre-define in complex environments [10]. Another example, Robust NMPC, treats the nonlinear parts of a robot’s dynamic model as a bounded disturbance [13], but relies on linearizing about a precomputed reference trajectory which can be difficult to generate for complex environments. Viability kernels have been computed to establish persistent feasibility for MPC [26]; however, these kernels have to be computed offline for a known environment. Recent pseudo-spectral methods approximate the NMPC program with polynomial functions to increase performance and computational efficiency [38]; nevertheless, these methods tradeoff between runtime and accuracy of the polynomial approximation.

Recent reachability-based approaches using funnel libraries have been proposed for real-time trajectory planning in the presence of uncertainty and arbitrary obstacles [29]. These approaches pre-compute a finite library of “funnels” that capture reachable sets of positions a robot might realize while tracking a reference trajectory. However, the funnels are computed about trajectories discretized in time, but this method does not address how fine the time discretization should be to ensure safety. Furthermore, the effectiveness of this method depends on the amount and type of trajectories in the precomputed library. Other reachability-based approaches employ the Hamilton-Jacobi-Bellman (HJB) equation to compute sets of safe feedback controllers in the presence of bounded disturbance [5]. These approaches rely upon

state-space discretization. The HJB framework has also been used recently to precompute error bounds for a high-dimensional nonlinear system tracking a trajectory designed for a low-dimensional system by MPC or RRT [17]. By augmenting obstacles with this pre-defined error bound, this approach can ensure the safety of a controller for the high-dimensional system if a feasible path is generated for the low-dimensional system. This method achieves rapid replanning, but assumes the underlying RRT or MPC planner is always able to find a feasible solution in the allotted planning time.

Prior work by the authors introduced a Reachability-based Trajectory Design (RTD) method to address the limitations of RRT, NMPC, funnel library, and HJB methods. The method computes a forward reachable (FRS) set in state space that captures the motion of a robot over a continuum of parameterized trajectories while accounting for tracking error [22]. Obstacles are represented as semi-algebraic sets, and intersected with the FRS to determine sets of safe trajectories. Unfortunately this set intersection process cannot be completed in real-time. Additionally, computation of the FRS is limited by system dimension; hence it was applied to a differential-drive unicycle model following Dubins paths.

As depicted in Figure 1, the present work contains three contributions, which address the shortcomings of the prior RTD method and demonstrate its application. First, we adapt system decomposition techniques, which have been effectively applied to reduce computational memory requirements for Backwards Reachable Sets [3, 4], to RTD and forward reachability. Second, we present a method for representing obstacles with discrete, finite sets, which enables provably safe, real-time planning. Third, we demonstrate RTD on two autonomous mobile robots to illustrate that the method is safe and persistently feasible. The platforms are a differential-drive “Segway” and a car-like “Rover,” depicted in Figures 2a and 2b respectively.

The paper is organized as follows. Section 2 introduces notation and key assumptions. Section 3 describes the general method for offline computation of the FRS. Section 4 presents the system decomposition technique to compute the FRS for higher-dimension systems. Section 5 prescribes conditions required to ensure safety and persistent feasibility. Section 6 presents a method for representing obstacles that enables safe, real-time planning. Section 7 describes the online receding-horizon trajectory optimization procedure. Section 8 describes the application of RTD to the Segway and Rover. Section 9 presents results of a simulation comparing RTD to RRT and NMPC for the Segway and Rover. Section 10 describes the hardware demonstrations on the FRS on the Segway and Rover.

2 PRELIMINARIES

This section introduces the notation used throughout the paper, the dynamic models used to describe the robot and to plan trajectories, and assumptions about the robot and its environment.

2.1 Notation

Sets are italicized and capitalized. For a set K , its boundary is ∂K , its closure is $\text{cl}(K)$, its complement is K^C , its interior is $\text{int}(K)$, and its cardinality is $|K|$. The power set of K is $\mathcal{P}(K)$. The set of continuous (resp. absolutely continuous) functions on a compact set K is $C(K)$ (resp. $AC(K)$). The Lebesgue measure on K is denoted by λ_K , and the volume of K is $\text{vol}(K) = \int_K \lambda_K$. The ring of polynomials in x is $\mathbb{R}[x]$, and the degree of a polynomial is the degree of its largest multinomial; the degree of the multinomial x^α , $\alpha \in \mathbb{N}$ is $|\alpha| = \|\alpha\|_1$. $\mathbb{R}_d[x]$ is the set of polynomials in x with degree d . The vector of coefficients of a polynomial p is denoted $\text{vec}(p)$. For a pair of vector-valued functions f and g with domain \mathbb{R}^n , the notation \circ denotes the elementwise product: $f \circ g = [f_1 \cdot g_1, \dots, f_n \cdot g_n]^\top$.

For points, sets, and functions, subscripts are used to indicate an index, subspace or subset. Let $\mathbb{R}_{>0}$ (resp. $\mathbb{R}_{\geq 0}$) denote the set $(0, \infty)$ (resp. $[0, \infty)$). For a state space Z with state $\zeta \in Z$: Z_0 indicates a set of initial conditions, and Z_j indicates a lower-dimensional subspace j of Z , where j can be an index or a coordinate of the state ζ . When referring to states, subscripts are used to indicate a particular index or subspace the state belongs to. For example ζ_i can be used to indicate the i^{th} component of ζ , or if Z_j indicates a lower-dimensional subspace j of Z then $\zeta_j \in Z_j$ indicates a state in subspace j . Superscripts are associated with the degree of a function or dimension of a space, for example f^d may refer to a polynomial function, f , of maximum degree d . Note one important exception: for the set of polynomials $\mathbb{R}_d[x]$, d appears as a subscript, to avoid confusion with the superscript on \mathbb{R} commonly used to indicate dimension.

2.2 Dynamic Models

Our approach controls a robot described by a high-fidelity model using a feedback controller to track parameterized trajectories generated by a lower dimensional trajectory-producing model. Each trajectory is of time duration T , and planning is performed in a receding horizon fashion, where a new trajectory is chosen every τ_{plan} seconds. Planning over the low-dimensional space of trajectory parameters enables our trajectory planner to operate in real-time. Safety is achieved by bounding trajectory tracking error, and by formulating a reachability-based constraint for obstacle avoidance.

Let the high-fidelity model have a state vector $\zeta_{\text{hi}} \in Z_{\text{hi}}$, feedback controller $u : [0, T] \times Z_{\text{hi}} \rightarrow U$, and dynamics at time $t \in [0, T]$ described by:

$$\dot{\zeta}_{\text{hi}}(t) = f_{\text{hi}}(t, \zeta_{\text{hi}}(t), u(t, \zeta_{\text{hi}}(t))), \quad (1)$$

where $f_{\text{hi}} : [0, T] \times Z_{\text{hi}} \times U \rightarrow \mathbb{R}^{n_{Z_{\text{hi}}}}$, $T > 0$, $Z_{\text{hi}} \subset \mathbb{R}^{n_{Z_{\text{hi}}}}$ and $U \subset \mathbb{R}^{n_U}$. We call T the planning time horizon.

Let the trajectory-producing model be written as:

$$\begin{bmatrix} \dot{\zeta}_{\text{des}}(t) \\ \dot{k}(t) \end{bmatrix} = \begin{bmatrix} f(t, \zeta_{\text{des}}(t), k(t)) \\ 0 \end{bmatrix} \quad (2)$$

where $f : [0, T] \times Z \times K \rightarrow \mathbb{R}^{n_Z}$. A trajectory produced by this model in the space Z is called a desired trajectory. The trajectory states ζ_{des} belong to a subspace $Z \subset Z_{\text{hi}}$, and the parameters k are drawn from a set $K \subset \mathbb{R}^{n_K}$. The parameters k are fixed over the planning time horizon $[0, T]$, as we describe in Section 7. Note that, to lighten notation, we drop the state and input arguments in the dynamics when they are clear from context. For example, we may write $f_{\text{hi}}(t, \zeta_{\text{hi}}, u)$ instead of $f_{\text{hi}}(t, \zeta_{\text{hi}}(t), u(t, \zeta_{\text{hi}}(t)))$.

Assumption 1. *The dynamics f_{hi} from (1) are Lipschitz continuous in t , ζ_{hi} , and u . The dynamics f from (2) are Lipschitz continuous in t , ζ , and k . Since planning occurs in a loop, a new trajectory parameter k can be chosen every τ_{plan} seconds, i.e. the desired trajectory can vary discretely from one planning iteration to the next.*

Assumption 2. *The sets U , Z_{hi} , Z , and K are compact. The robot's set of initial conditions are represented as a compact set $Z_{\text{hi},0} \subset Z_{\text{hi}}$ for the high-fidelity model, and $Z_0 \subset Z$ in the shared states of the trajectory-producing model.*

2.2.1 Required States

Now, we point out several states that must be in the space Z_{hi} for RTD. In this work we focus on ground applications where the robot's pose and environment can be represented in 2-D, i.e. the space \mathbb{R}^2 with coordinates denoted x and y .

Definition 3. *Let $X \subset Z$ denote the xy-subspace of Z . We also refer to X as the spatial coordinates of the robot's body. Let X_0 denote the projection of Z_0 into the xy-subspace. We call X_0 the robot's footprint at time 0.*

All of the points on the robot's body lie in the state space X , with initial condition set X_0 at time $t = 0$. Therefore, the high-fidelity dynamics in (1) must include the dynamics of every point on the robot's body. However, dynamic models typically only describe the position of a single point on the robot (typically the center of mass) [6], and the dynamics of the rest of the robot's body are written relative to this point, because the robot is treated as a rigid body. To perform safe trajectory planning, it is insufficient to ensure that just a single point on the robot avoids collision with obstacles; therefore, we must consider the dynamics of the robot's entire body, leading to the following assumption.

Assumption 4. *Since the robot is traveling in the plane, we assume that the trajectory-producing state vector ζ contains a pair of states $[x_c, y_c]^T$ that describe the position of the center of mass of the robot. These states occupy a subspace $X_c \subset X$, which we call the center of mass coordinates. We further assume that the robot is a rigid body. Let θ be the robot's heading. The motion of every point on the robot's body are given by the states $[x, y]^T \in X$ with the following dynamics:*

$$\begin{aligned} \dot{x} &= \dot{x}_c - \dot{\theta} \cdot (y - y_c) \\ \dot{y} &= \dot{y}_c + \dot{\theta} \cdot (x - x_c). \end{aligned} \quad (3)$$

The equations of rigid body motion in (3) are available in any introductory dynamics course, e.g., [44, Lecture 7].

Remark 5. Assumption 4 requires the trajectory-producing dynamics (2) to describe the motion of the robot's entire body, not just its center of mass. This means that (2) includes a pair of states for $[x_c, y_c]^\top$, and a pair of states for $[x, y]^\top$ with dynamics (3). So, the dimension of the trajectory-producing state space Z is at least 4. However, there are two cases where the dynamics of every point $[x, y]^\top$ can be treated as identical to $[x_c, y_c]^\top$ for the purpose of obstacle avoidance. The first case is when the robot has a circular footprint, so rotating the robot's body does not change the subset of X that the robot occupies. The second case is when the robot's footprint does not have any yaw motion, in which case $\dot{\theta} = 0$ in (3).

Note that treating all points on the robot's body as $[x_c, y_c]^\top$ is useful because, the higher the dimension of the dynamics (2), the more difficult it is to compute trajectory plans in real time (see, e.g., [17, 22, 21]). Section 6 (see Definition 46) provides more detail on the motion of the robot's footprint through time.

Next, we place assumptions on the robot's speed and yaw rate.

Assumption 6. We assume that the robot has a speed state v in its high-fidelity state vector ζ_{hi} . The robot is limited to a scalar max speed (its rate of travel in the subspace X), denoted v_{max} . If the robot has a yaw rate state, it is limited to a scalar maximum absolute yaw rate, denoted ω_{max} .

Recall that by Assumption 4, the robot has 2-D spatial coordinates of its center of mass $[x_c, y_c]^\top$, with dynamics in the high-fidelity model f_{hi} from (1). If f_{hi} has no speed state, then we append the coordinate $v = \sqrt{\dot{x}_c^2 + \dot{y}_c^2}$ to the state ζ_{hi} , which now evolves in the space $Z_{\text{hi}} \times [0, v_{\text{max}}]$, which preserves the compactness of the state space in Assumption 2. Note that we do not require a yaw rate state; as noted in Remark 5, without a yaw rate state, the robot's entire body only translates in X .

We now present an example of the high-fidelity dynamics (1).

Example 7. Consider the Segway, depicted in Figure 2a. This type of differential-drive robot can be described by a high-fidelity model:

$$\underbrace{\frac{d}{dt} \begin{bmatrix} x_c(t) \\ y_c(t) \\ \theta(t) \\ \omega(t) \\ v(t) \end{bmatrix}}_{\zeta_{\text{hi}}(t)} = \underbrace{\begin{bmatrix} v(t) \cos \theta(t) \\ v(t) \sin \theta(t) \\ \omega(t) \\ \gamma(t, \zeta_{\text{hi}}(t)) \\ \alpha(t, \zeta_{\text{hi}}(t)) \end{bmatrix}}_{f_{\text{hi}}(t, \zeta_{\text{hi}}(t), u(t, \zeta_{\text{hi}}(t)))}, \quad (4)$$

where x_c and y_c describe the robot's center of mass as in Assumption 4 and the control input is $u = [\gamma, \alpha]^\top$. In this case, the robot has a circular footprint, so all points on the robot can be described by the center of mass dynamics as per Remark 5. The control input is given by:

$$\gamma(t, \zeta_{\text{hi}}(t)) = \min\{\bar{\gamma}, \max\{\underline{\gamma}, (\beta_\gamma(\omega_{\text{des}}(t) - \omega(t)) + \beta_\theta(\theta(t) - \theta_{\text{des}}(t)))\}\} \quad (5)$$

$$\alpha(t, \zeta_{\text{hi}}(t)) = \min\{\bar{\alpha}, \max\{\underline{\alpha}, (\beta_\alpha + \beta_v)(v_{\text{des}}(t) - v(t))\}\}. \quad (6)$$

Here, $[\underline{\gamma}, \bar{\gamma}]$ (resp. $[\underline{\alpha}, \bar{\alpha}]$) is the range of possible commanded yaw (resp. longitudinal) acceleration. The parameters β_γ , β_α , β_θ , and β_v are nonnegative scalars. The control input performs feedback about a desired heading θ_{des} , desired yaw rate ω_{des} , and desired speed v_{des} .

See Section 8.1 for the values of β_γ , β_α , β_θ , β_v used for the Segway hardware in Figure 2a and the simulation in Section 9.

The previous discussion introduces a variety of subspaces of the robot's state space Z_{hi} . To better understand the relationship between these various subspaces, we define projection operators, adapted from [3, Section III A, (15,16,18)]:

Definition 8. The projection operator $\text{proj}_{Z_i} : \mathcal{P}(Z) \rightarrow \mathcal{P}(Z_i)$ maps sets from the higher-dimensional space Z to a lower-dimensional subspace $Z_i \subseteq Z$. For a set made up of a single point, $\zeta \in Z$, proj_{Z_i} is defined as:

$$\text{proj}_{Z_i}(\zeta) = \zeta_i, \quad (7)$$

where ζ_i contains the components of ζ that lie in subspace Z_i . For a set, $S \subseteq Z$, proj_{Z_i} is defined as:

$$\text{proj}_{Z_i}(S) = \{\zeta_i \in Z_i : \exists \zeta \in S \text{ s.t. } \text{proj}_{Z_i}(\zeta) = \zeta_i\}. \quad (8)$$

Similar to proj_{Z_i} , let the operator $\text{proj}_Z : \mathcal{P}(Z_{\text{hi}}) \rightarrow \mathcal{P}(Z)$ project points or sets from the high-fidelity model state space into the lower-dimensional, trajectory-producing space.

We also define $\text{proj}^{-1} : \mathcal{P}(Z) \rightarrow \mathcal{P}(Z)$ to be the back-projection operator from a subset, $S_i \subseteq Z$, to the full space, Z is defined as:

$$\text{proj}^{-1}(S_i) = \{\zeta \in Z : \exists \zeta_i \in S_i \text{ s.t. } \text{proj}_{Z_i}(\zeta) = \zeta_i\}. \quad (9)$$

Note that the projection operator is continuous [32, Theorem 18.2(b)]. Note that S_i can be a subset of a subspace $Z_i \subseteq Z$. As an example of Definition 8, the operator $\text{proj}_X : \mathcal{P}(Z) \rightarrow \mathcal{P}(X)$ projects points or sets into the xy -subspace, so $X = \text{proj}_X(Z)$. If $\zeta \in Z$, then proj_X maps ζ to $[\zeta_x, \zeta_y]^\top \in X$ where ζ_x and ζ_y are the x and y components of ζ respectively. To simplify exposition, we abuse notation and also use proj_X to project directly from Z_{hi} to the xy -subspace X , as opposed to composing proj_X with proj_Z , when the intent is clear from context.

2.2.2 Bounding Sources of Error

Now we address the robot's ability to track trajectories. The robot, described by the high-fidelity model, uses a feedback controller to follow trajectories produced by the trajectory-producing model. Recall that the trajectories are parameterized by k , so given $k \in K$, the robot is able to generate a feedback controller for k

$$u_k : [0, T] \times Z_{\text{hi}} \rightarrow U \quad (10)$$

to track the desired trajectory. When controlled by u_k , we say that the high-fidelity model tracks k as a shorthand to mean that the high-fidelity model tracks the trajectory parameterized by k . The method presented is agnostic to the type of feedback used (e.g., PID, LQR, MPC). Our approach requires that that we can quantify and bound all error observed when tracking the parameterized trajectories. There are two sources of error. The first comes from model uncertainty between the high-fidelity model and the actual robot; during online planning, this is expressed as state estimation error. The second comes from the fact that the high-fidelity model cannot perfectly track desired trajectories from (2); we call this tracking error. We place bounds on the state estimation error and tracking error as follows.

Assumption 9. Let $k \in K$ be arbitrary and u_k the corresponding feedback controller as in (10). Suppose the robot is at time t , with estimated state $\zeta_{\text{hi},0} \in Z_{\text{hi},0}$, and recall that T is the planning time horizon. The robot's future state prediction ζ_{pred} at any $t' \in [t, t+T]$ is given by forward-integrating the high-fidelity model to get the trajectory $\zeta_{\text{hi},0} : [0, T] \rightarrow Z_{\text{hi}}$:

$$\zeta_{\text{pred}}(t'; \zeta_{\text{hi},0}, k) = \zeta_{\text{hi},0} + \int_t^{t'} f_{\text{hi}}(\tau, \zeta_{\text{pred}}(\tau), u_k(\tau, \zeta_{\text{pred}}(\tau))) d\tau. \quad (11)$$

We assume the robot has a state estimator such that the state estimation error in the robot's spatial coordinates x and y is bounded for every $t' \in [t, t+T]$ where T is the time horizon of the robot's planned trajectories. In other words, there exist $\varepsilon_x, \varepsilon_y \geq 0$ such that the position of the actual robot is within ε_x (resp. ε_y) of its estimated position in the x (resp. y) coordinate. Note that this is trivially satisfied by picking large ε_x and ε_y .

Next, we place a bound on the trajectory tracking error:

Assumption 10. For each $i \in \{1, \dots, n_Z\}$, there exists a bounded function $g_i : [0, T] \times Z \times K \rightarrow \mathbb{R}$ such that:

$$\max_{\zeta_{\text{hi}} \in A_\zeta} |f_{\text{hi},i}(t, \zeta_{\text{hi}}, u_k(t, \zeta_{\text{hi}})) - f_i(t, \zeta, k)| \leq g_i(t, \zeta, k), \quad (12)$$

for all $\zeta \in Z$, $t \in [0, T]$, and $k \in K$ where $A_\zeta := \{\zeta_{\text{hi}} \in Z_{\text{hi}} \mid \text{proj}_Z(\zeta_{\text{hi}}) = \zeta\}$ is the set in which the high-fidelity model matches the trajectory-producing model in all the shared states. We call $g = [g_1, \dots, g_{n_Z}]^\top$ the tracking error function. As with f and f_{hi} in Assumption 1, we assume that g is Lipschitz continuous in t , ζ , and k .

The existence of the tracking error function means that the error in the shared states (in $Z \subset Z_{\text{hi}}$) is bounded while the robot is tracking any desired trajectory given by (2). The tracking error function can be determined empirically by simulating the high-fidelity model or by applying Sums-Of-Squares (SOS) optimization techniques [24]. The construction of such a function is not the focus of this paper. See Figure 3 for an example of g for the Segway from Example 7, and Appendix 14 for the exact forms of the error functions for the Segway and Rover from Figure 2.

We now relate these types of error to understand how to ensure safety of the actual robot. First, note that the state estimation error affects the robot’s ability to perform feedback around trajectories using the high-fidelity model. The trajectory tracking error is then determined by the high-fidelity model’s ability to track parameterized trajectories, leading to the following remark.

Remark 11. *By Assumption 9, every point on the actual robot’s body lies within a box of size $\varepsilon_x \times \varepsilon_y$ of the same point on the robot’s body described by using the high-fidelity model for state estimation. Suppose an obstacle is a subset of X , and that we expand it by $\pm\varepsilon_x$ and $\pm\varepsilon_y$ in the x - and y -directions respectively, before performing trajectory planning. If we ensure safety of the high-fidelity model (despite tracking error) relative to this expanded obstacle, then we know that the actual robot is safe.*

By Remark 11, to make the actual robot safe, we must ensure that the high-fidelity model is safe while planning with the trajectory-producing model (2). We explicitly define the “expanded obstacle” in Section 5. Expanding an obstacle alone does not ensure safety, because we still have to represent the obstacle in a way that can be used to plan trajectories that avoid it at runtime; we address this in Section 6. Moreover, we still have to compensate for the tracking error that results from planning trajectories for the high-fidelity model (1) with the trajectory-producing model (2). To relate these two models, we introduce the “trajectory-tracking model” as follows.

Let $L_d := L^1([0, T], [-1, 1]^{nz})$ denote the space of absolutely integrable functions from $[0, T]$ to $[-1, 1]^{nz}$. We include g in the trajectory-producing dynamics to create the trajectory-tracking model with dynamics:

$$\dot{\zeta}(t, \zeta(t), k, d) = f(t, \zeta(t), k) + g(t, \zeta(t), k) \circ d(t) \quad (13)$$

where $d \in L_d$, so $d(t) \in [-1, 1]^{nz}$ almost everywhere $t \in [0, T]$ can be chosen to describe worst-case error behavior. Recall that \circ denotes the element-wise product. We can use d to make the trajectory-producing model “match” the high-fidelity model in the shared states:

Lemma 12. *Suppose $\zeta_{\text{hi},0} \in Z_{\text{hi},0}$, $k \in K$, and $\zeta_0 = \text{proj}_Z(\zeta_{\text{hi},0})$. Then there exists $d \in L_d$ such that the high-fidelity model and the trajectory-tracking model agree on the shared state space Z :*

$$\text{proj}_Z(f_{\text{hi}}(t, \zeta_{\text{hi}}(t), u_k(t, \zeta_{\text{hi}}(t)))) = \dot{\zeta}(t, \zeta(t), k, d(t)) \quad \forall t \in [0, T], \quad (14)$$

where ζ_{hi} (resp. ζ) is a trajectory produced by (1) (resp. (13)) with initial condition $\zeta_{\text{hi},0}$ (resp. ζ_0).

Proof. From Assumption 10 and (12), recall that g bounds the maximum possible absolute error in each shared state for all $t \in [0, T]$. Therefore, almost everywhere $t \in [0, T]$, we can pick $d(t) \in [-1, 1]^{nz}$ such that

$$\text{proj}_Z(f_{\text{hi}}(t, \zeta_{\text{hi}}(t), u_k(t, \zeta_{\text{hi}}(t)))) - f(t, \zeta(t), k) = g(t, \zeta(t), k) \circ d(t), \quad (15)$$

then rearrange to fulfill (14). ■

We illustrate the trajectory-tracking model with an example.

Example 13. *Consider the high-fidelity model for the Segway from Example 7. This model can track (with error) Dubins paths parameterized by a desired yaw-rate, which we relabel k_1 , and desired speed, relabeled k_2 ; these trajectory parameters obey the max yaw rate and speed as in Assumption 6. The trajectory-tracking model is:*

$$\frac{d}{dt} \underbrace{\begin{bmatrix} x(t) \\ y(t) \end{bmatrix}}_{\zeta(t)} = \underbrace{\begin{bmatrix} k_2 - k_1(y(t) - y_{c,0}) \\ k_1(x(t) - x_{c,0}) \end{bmatrix}}_{f(t, \zeta, k)} + \underbrace{\begin{bmatrix} g_x(t) \cdot d_x(t) \\ g_y(t) \cdot d_y(t) \end{bmatrix}}_{g(t, \zeta, k) \circ d(t)}, \quad (16)$$

where, at the beginning of each planning iteration, $x_{c,0}$ and $y_{c,0}$ are the initial position of the center of mass in a global reference frame that is rotated so the positive x -direction points in the robot’s longitudinal direction of travel. Therefore, the initial heading is $\theta(0) = 0$, and $\theta_{\text{des}}(t) = k_1 t$; since the heading is only a function of time, it does not need to be included in the trajectory-producing model. So, in this case, $Z = X$. Recall that the trajectory parameters $[k_1, k_2]^T \in K$ are constant over the planning time horizon $[0, T]$ as per (2), so their dynamics are omitted from (16).

See Figure 8 for example trajectories produced by this model, and Figure 3 for example tracking error functions g_x and g_y . See Appendix 14 for the exact form of the tracking error functions.

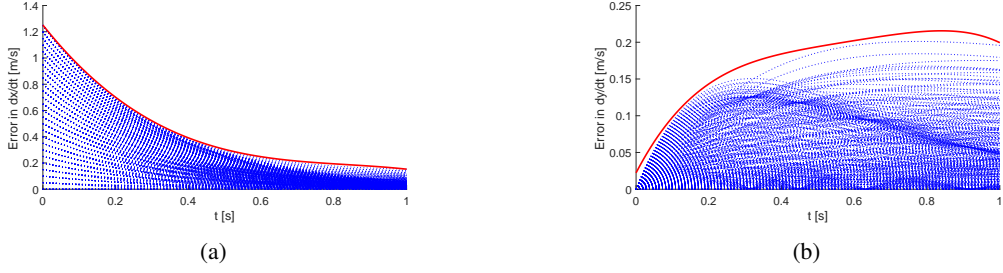


Figure 3: Error in \dot{x} (Figure 3a) and \dot{y} (Figure 3b) of the Segway’s high-fidelity model (4) when tracking Dubins paths generated as in Example 13. The robot has a maximum yaw rate of 1 rad/s and a maximum speed of 1.25 m/s. Error is the expression $|\dot{f}_{hi,i}(t, \zeta_{hi}, u_k(t, \zeta_{hi})) - \dot{f}_i(t, \zeta, k)|$ in Assumption 10, where i selects the x and y components of ζ_{hi} and ζ . The blue dashed lines are example error trajectories created by sampling possible initial conditions. The solid red lines represent the functions g_x and g_y , which bound all of the error trajectories. See Example 76 in Appendix 14 for exact form of g .

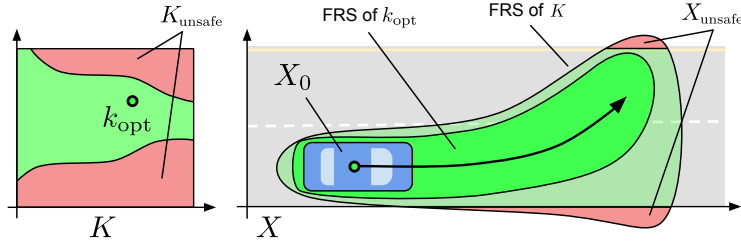


Figure 4: An illustration of the general approach to trajectory planning with RTD. The blue autonomous robot’s trajectory parameter space K is on the left, and the xy -subspace X of its state space is on the right. The bell-shaped contour in X shows the total extent of the forward reachable set (FRS), corresponding to the entirety of K . In X , the red areas are unsafe, and the green areas are safe; the corresponding trajectory parameters are colored and labeled appropriately on the left. A safe parameter k_{opt} (black circle filled with green) is selected in K , and the corresponding trajectory (black arrow) and corresponding subset of the FRS in X (bright green contour) are shown on the right.

3 Forward Reachable Set Computation

The Reachability-based Trajectory Design (RTD) method for provably safe planning has two steps:

1. Precompute a Forward Reachable Set (FRS) that captures all possible trajectories and associated parameters over a time interval $[0, T]$.
2. Perform trajectory optimization online over a user-specified cost function to select trajectory parameters $k \in K$ that are safe, meaning if the robot follows a trajectory parameterized by k , it will not collide with an obstacle.

The method is illustrated in Figure 4. This section describes the first step of RTD, with minor modifications from the original paper [22]. We discuss how to choose the time horizon T to ensure persistent feasibility in Section 5.

Note that, in [22], an additional step called set intersection is presented, and is performed during online operation before the trajectory optimization step. Set intersection uses SOS programming to intersect obstacles, represented as semi-algebraic sets, with the FRS, resulting in a polynomial approximation of the safe set of trajectory parameters. This intersection procedure is found to be too slow for real-time trajectory planning with 1-D obstacles (see [22, Section V] for more details). In Section 6.1, we briefly discuss the set intersection procedure to motivate the rest of Section 6, wherein we modify the obstacle representation to enable real-time performance without compromising safety guarantees.

3.1 Problem Formulation

The FRS contains positions in the xy -subspace X that are reachable by a robot described by the high-fidelity model (1) while tracking trajectories produced by the trajectory-producing model (2), despite tracking error, over a time

horizon T . Formally, we define the FRS:

$$\begin{aligned} \mathcal{X}_{\text{FRS}} = \{ & (x, k) \in X \times K \mid \exists \zeta_0 \in Z_0, \tau \in [0, T], \text{ and } d \in L_d \\ & \text{s.t. } x = \text{proj}_X(\tilde{\zeta}(\tau)), \text{ where } \dot{\tilde{\zeta}}(t) = f(t, \tilde{\zeta}(t), k) + g(t, \tilde{\zeta}(t), k) \circ d(t) \\ & \text{a.e. } t \in [0, T] \text{ and } \tilde{\zeta}(0) = \zeta_0\}. \end{aligned} \quad (17)$$

To understand the gap between the high-fidelity model and the trajectory-producing model, we rely upon a pair of linear operators, $\mathcal{L}_f, \mathcal{L}_g : AC([0, T] \times Z \times K) \rightarrow C([0, T] \times Z \times K)$ which act on a test function v as follows:

$$\mathcal{L}_f v(t, \zeta, k) = \frac{\partial v}{\partial t}(t, \zeta, k) + \sum_{i=1}^n \frac{\partial v}{\partial \zeta_i}(t, \zeta, k) f_i(t, \zeta, k) \quad (18)$$

$$\mathcal{L}_g v(t, \zeta, k) = \sum_{i=1}^n \frac{\partial v}{\partial \zeta_i}(t, \zeta, k) g_i(t, \zeta). \quad (19)$$

With these operators, we can compute the FRS by solving the following linear program, adapted from [30, Section 3.3, Program (D)]. The program has been altered for forward reachability, for uncertainty propagation in place of control synthesis, and to restrict the decision variable w to $X \subset Z$.

$$\inf_{v, w, q} \int_{X \times K} w(x, k) d\lambda_{X \times K} \quad (D)$$

$$\text{s.t. } \mathcal{L}_f v(t, \zeta, k) + q(t, \zeta, k) \leq 0, \quad \forall (t, \zeta, k) \in [0, T] \times Z \times K \quad (D1)$$

$$\mathcal{L}_g v(t, \zeta, k) + q(t, \zeta, k) \geq 0, \quad \forall (t, \zeta, k) \in [0, T] \times Z \times K \quad (D2)$$

$$-\mathcal{L}_g v(t, \zeta, k) + q(t, \zeta, k) \geq 0, \quad \forall (t, \zeta, k) \in [0, T] \times Z \times K \quad (D3)$$

$$q(t, \zeta, k) \geq 0, \quad \forall (t, \zeta, k) \in [0, T] \times Z \times K \quad (D4)$$

$$-v(0, \zeta, k) \geq 0, \quad \forall (\zeta, k) \in Z_0 \times K \quad (D5)$$

$$w(x, k) \geq 0, \quad \forall (x, k) \in X \times K \quad (D6)$$

$$w(x, k) + v(t, \zeta, k) - 1 \geq 0, \quad \forall (t, \zeta, k) \in [0, T] \times Z \times K \quad (D7)$$

where $x = \text{proj}_X(\zeta)$. The given data in the problem are f, g, Z, Z_0, K , and T . The infimum is taken over $(v, w, q) \in C^1([0, T] \times Z \times K) \times C(X \times K) \times C([0, T] \times Z \times K)$. It is shown in [30, Theorem 3] that feasible solutions to (D) conservatively approximate \mathcal{X}_{FRS} . We adapt this result in the following lemma:

Lemma 14. *If (v, w, q) satisfies the constraints in (D), then v is non-positive and decreasing along trajectories of the trajectory-tracking system (13). In other words, let $\zeta \in Z$ and $x = \text{proj}_X(\zeta)$; then $(x, k) \in \mathcal{X}_{\text{FRS}}$ implies that $\exists t \in [0, T]$ such that $v(t, \zeta, k) \leq 0$.*

Proof. Notice that $v(0, \zeta, k) \leq 0$ for all $\zeta \in Z_0$ and $k \in K$ by (D5). So, for any $\tau \in [0, T]$, $k \in K$, and $d \in L_d$, we have:

$$v(\tau, \zeta(\tau), k) = v(0, \zeta(0), k) + \int_0^\tau (\mathcal{L}_f v(t, \zeta(t), k) + \mathcal{L}_g v(t, \zeta(t), k) \circ d(t)) dt \quad (20)$$

$$\leq v(0, \zeta(0), k) + \int_0^\tau (\mathcal{L}_f v(t, \zeta(t), k) + q(t, \zeta(t), k)) dt \quad (21)$$

$$\leq v(0, \zeta(0), k), \quad (22)$$

where (20) follows from the Fundamental Theorem of Calculus; (21) follows from (D2) and (D3); and (22) follows from (D1). \blacksquare

The result of Lemma 14 and constraint (D7) is that the 1-superlevel set of any feasible w contains \mathcal{X}_{FRS} [22, Lemma 11]. In fact, the solution to this infinite dimensional linear program allows one to compute \mathcal{X}_{FRS} :

Lemma 15. [30, Theorem 4] *Let (v, w, q) be a feasible solution to (D). The 1-superlevel set of w contains \mathcal{X}_{FRS} . Furthermore, there is a sequence of feasible solutions to (D) whose second component w converges from above to an indicator function on \mathcal{X}_{FRS} in the L^1 -norm and almost uniformly.*

3.2 Implementation and Memory Usage

A method to solve Problem (D) using SOS optimization is presented in [22]. In this section, we explore the implementation of (D), and the memory required to do so. For higher-dimensional systems, this motivates the system decomposition approach in Section 4. To implement (D), we require the following assumptions:

Assumption 16. *The functions f and g are polynomials of finite degree in $\mathbb{R}[t, \zeta, k]$.*

Note that, by Assumption 10, if f is Taylor-expanded to be a polynomial, then g also bounds the corresponding error in the Taylor-expansion of f .

Assumption 17. *The sets K , Z , and Z_0 have semi-algebraic representations:*

$$K = \{k \in \mathbb{R}^{n_K} \mid h_{K_i}(k) \geq 0, \forall i = 1, \dots, n_K\} \quad (23)$$

$$Z = \{\zeta \in \mathbb{R}^{n_Z} \mid h_{Z_i}(\zeta) \geq 0, \forall i = 1, \dots, n_Z\} \quad (24)$$

$$Z_0 = \{\zeta \in Z \mid h_{0_i}(\zeta) \geq 0, \forall i = 1, \dots, n_0\} \quad (25)$$

where $h_{K_i} \in \mathbb{R}[k]$ and $h_{0_i}, h_{Z_i} \in \mathbb{R}[\zeta]$. Since X and X_0 are projected (as in Definition 8, using proj_X) from semi-algebraic sets, they can also be represented semi-algebraically:

$$X = \{p \in \mathbb{R}^2 \mid h_x(p) \geq 0, h_y(p) \geq 0\} \quad (26)$$

$$X_0 = \{p \in X \mid h_{x_0}(p) \geq 0, h_{y_0}(p) \geq 0\}. \quad (27)$$

Assumption 17 is not prohibitive since common boxes and ellipses, and even non-convex sets, have semi-algebraic representations (see, e.g., [30]). Typically, Z , X_0 , and Z_0 are box- or ellipse-shaped. The parameter space K can be represented by a box or ellipse; more complex restrictions of the parameters can be enforced in the online optimization program described in Algorithm 2. Also note that, for the SOS program posed next, we require that there exists $N \in \mathbb{N}$ such that, for any $q = (t, \zeta, \zeta_0, k) \in [0, T] \times Z \times Z_0 \times K$, the value of $N - \|q\|_2^2 \geq 0$ [24, Theorem 2.15]. This is trivially satisfied since $[0, T]$, Z , Z_0 , and K are compact by Assumption 2.

3.2.1 Computing the FRS

To solve (D), we follow the implementation in [22, Section 4]. We construct a sequence of convex SOS programs indexed by $l \in \mathbb{N}$ by relaxing the continuous function in (D) to polynomial functions with degree truncated to $2l$. The inequality constraints in (D) then transform into SOS constraints, so (D) becomes a Semi-Definite Program (SDP) [37]. To formulate this problem, let $h_T = t(T - t)$, and $H_T = \{h_T\}$. Recalling the definitions in Assumption 17, for Z , Z_0 , and K , collect the polynomials that represent them in the sets $H_Z = \{h_{Z_1}, \dots, h_{Z_{n_Z}}\}$, $H_{Z_0} = \{h_{0_1}, \dots, h_{0_{n_0}}\}$, $H_K = \{h_{K_1}, \dots, h_{K_{n_K}}\}$, and $H_X = \{h_x, h_y\}$.

Let $Q_{2l}(H_T, H_Z, H_K) \subset \mathbb{R}_{2l}[t, \zeta, k]$ be the set of polynomials $p \in \mathbb{R}_{2l}[t, \zeta, k]$ (i.e., of total degree less than or equal to $2l$) expressible as:

$$p = s_0 + s_1 h_T + \sum_{i=1}^{n_Z} s_{i+2} h_{Z_i} + \sum_{i=1}^{n_K} s_{i+n_Z+2} h_{K_i}, \quad (28)$$

for some polynomials $\{s_i\}_{i=0}^{n_Z+n_K+1} \subset \mathbb{R}_{2l}[t, \zeta, k]$ that are SOS of other polynomials. Note that every such polynomial is non-negative on $[0, T] \times Z \times K$ (see [24, Theorem 2.14]). Similarly, define $Q_{2l}(H_{Z_0}, H_K) \subset \mathbb{R}_{2l}[\zeta, k]$, and $Q_{2l}(H_X, H_K) \subset \mathbb{R}_{2l}[x, k]$, where $x = \text{proj}_X(\zeta)$.

Employing this notation, the l^{th} -order relaxed SOS programming representation of (D), denoted (D^l) , is defined as

follows:

$$\begin{aligned}
& \inf_{v^l, w^l, q^l} y_{X \times K}^T \text{vec}(w^l) && (D^l) \\
& \text{s.t. } -\mathcal{L}_f v^l - q^l && \in Q_{2d_f}(H_T, H_Z, H_K) \\
& \quad \mathcal{L}_g v^l + q^l && \in Q_{2d_g}(H_T, H_Z, H_K) \\
& \quad -\mathcal{L}_g v^l + q^l && \in Q_{2d_g}(H_T, H_Z, H_K) \\
& \quad q^l && \in Q_{2l}(H_T, H_Z, H_K) \\
& \quad -v^l(0, \cdot) && \in Q_{2l}(H_{Z_0}, H_K) \\
& \quad w^l && \in Q_{2l}(H_X, H_K) \\
& \quad w^l + v^l - 1 && \in Q_{2l}(H_T, H_Z, H_K),
\end{aligned}$$

where the infimum is taken over the vector of polynomials $(v^l, w^l, q^l) \in \mathbb{R}_{2l}[t, \zeta, k] \times \mathbb{R}_{2l}[x, k] \times \mathbb{R}_{2l}[t, \zeta, k]$, with $x = \text{proj}_X(\zeta)$. The vector $y_{X \times K}$ contains moments associated with the Lebesgue measure $\lambda_{X \times K}$, so $\int_{X \times K} w(x, k) d\lambda_{X \times K} = y_{X \times K}^T \text{vec}(w)$ for $w \in \mathbb{R}_{2l}[x, k]$ [30]. The numbers d_f and d_g are the smallest integers such that $2d_f$ and $2d_g$ are respectively greater than the total degree of $\mathcal{L}_f v^l$ and $\mathcal{L}_g v^l$. To implement (D^l) , we consider the dual program, which is an SDP [24].

Remark 18. *It can be shown that Lemma 14 holds for functions that satisfy the constraints of (D^l) [30, Theorem 6]. Additionally, one can apply the last constraint in (D^l) to prove that the 1-superlevel set of any feasible w^l is an outer approximation to X_{FRS} [30, Theorem 7]. Furthermore, one can prove that w^l converges from above to an indicator function on X_{FRS} in the L^1 -norm [30, Theorem 6].*

3.2.2 Sums-of-Squares Memory Usage

In this paper, the FRS is computed with Spotless [43], a MATLAB-based SOS toolbox. Spotless transforms the SOS optimization program into an SDP, which is solved with MOSEK [31]. As the degree l increases, the approximation of the FRS becomes a provably less conservative outer approximation of X_{FRS} [30, Theorem 7]. However, solving (D^l) is memory intensive, as the number of free variables is a function of the number the coefficients of all the monomials in (v^l, w^l, q^l) and of the s polynomials (as in (28)) in each constraint of (D^l) . Let $n = n_Z + n_K + 1$ denote the total dimension (including time) of the trajectory-producing system, (2). The number of monomials in each decision variable polynomial of degree $2l$ and dimension n is $\binom{2l+n}{n}$ (see, e.g., the `monomials` function in Spotless [43]). The number of free variables per SOS constraint of degree $2l$ is $\frac{1}{2} \binom{l+n}{n} \left(\binom{l+n}{n} + 1 \right)$, which is the number of unique entries in a symmetric, positive semi-definite matrix with $\binom{l+n}{n}$ rows (see, e.g., [37, Section 4.2]). So, for a SOS program with N_{dv} decision variable polynomials and N_{cons} SOS constraints, the number of free variables is upper-bounded by

$$N_{\text{free}} = N_{\text{dv}} \cdot \binom{2l+n}{n} + N_{\text{cons}} \cdot \frac{1}{2} \binom{l+n}{n} \left(\binom{l+n}{n} + 1 \right). \quad (29)$$

Each free variable in (D^l) is stored as a 64-bit double. The memory required by (D^l) grows as $O((n+1)^l)$ for fixed l and $O(m^{+1})$ for fixed n [30, Section 4.2].

Now, recall that Program (D^l) has 3 polynomial decision variables and 7 SOS constraints. For a problem with $n = 5$ and $l = 6$, we have N_{free} is approximately 2.2×10^5 by (29). This is, in practice, the largest problem we can solve, because MOSEK is a second-order conic solver, so it is memory-limited since it computes the Hessian of each SOS constraint [31, Section 11.4], which is proportional to $(N_{\text{free}})^2$ (see, e.g., [34, Chapter 14]). A system dimension of $n = 5$ is sufficient for models such as the Segway's trajectory-tracking model (16) in Example 7. In practice, solving (D^l) for $n = 6$ is intractable for $l \geq 4$. As we show in the next section, a model for the Rover in Figure 2b that is capable of performing car-like lane change maneuvers requires $n = 6$. This motivates the system decomposition approach in Section 4, where we can solve two separate $n = 5$ FRS computations, then combine them into an $n = 6$ problem with fewer SOS constraints.

4 System Decomposition

Motivated by the memory issues presented in Section 3.2.2, this section presents a method to apply the FRS computation to higher-dimensional systems. Consider Example 7, where the trajectory-producing model in (16) creates arcs with constant speed and yaw rate. In some applications, it is beneficial to plan with more complicated trajectories. For example a passenger vehicle on a road would plan lane change, lane keeping, and lane return maneuvers, requiring a higher-dimensional model than the one that produces arcs. As noted in Section 3.2.2, for fixed relaxation degree l , increasing the dimension n of the trajectory-producing model increases memory usage of (D^l) as $O((n+1)^l)$ [30, Section 4.2].

This section adapts a general method from [3, 4] for computing backwards reachable sets by system decomposition. We adapt the method to forward reachability, illustrate how to apply SOS programming, and analyze the memory savings that result from using system decomposition. This type of decomposition applies when the robot’s dynamic model can be split into subsystems of lower dimension. We focus on the case with two subsystems, though the approach generalizes to any finite number. As in [3, 4], after separating the system, we compute a reachable set for each subsystem, then reconstruct the reachable set for the full system by intersecting the subsystem reachable sets. We begin with a practical example of trajectory-producing dynamics with a system dimension that makes computing the FRS intractable as discussed in Section 3.2.2.

Example 19. Recall the Rover from Figure 2b. This robot uses the following bicycle model as the trajectory-producing model (2), with states $\zeta = [x_c, y_c, \theta]^T \in Z \subset \mathbb{R}^3$ where x_c and y_c track the center of mass as in Remark 5.

$$\frac{d}{dt} \begin{bmatrix} x_c(t) \\ y_c(t) \\ \theta(t) \end{bmatrix} = \begin{bmatrix} k_3 \cos(\theta(t)) - l_r \omega(t, k) \sin(\theta(t)) \\ k_3 \sin(\theta(t)) + l_r \omega(t, k) \cos(\theta(t)) \\ \omega(t, k) \end{bmatrix} \quad (30)$$

$$\omega(t, k) = -2 \frac{T_h k_1 + k_2}{T_h^2} t + k_1 \quad (31)$$

where ω is yaw rate, k_3 is longitudinal speed, and l_r is the distance from the robot’s rear-wheel to center of mass. The trajectory parameters, $k \in K \subset \mathbb{R}^3$, produce lane change, lane keeping, and lane return maneuvers for an autonomous car driving on a straight road. T_h is the time required to complete a lane change, at which the robot heading realigns with the road; k_1 determines the initial yaw rate of the trajectory; and k_2 is the initial heading of the robot.

To understand this parameterization, integrate (31) over time with initial condition $\theta(0) = k_2$ to get the robot’s heading:

$$\theta(t) = -\frac{T_h k_1 + k_2}{T_h^2} t^2 + k_1 t + k_2 \quad (32)$$

Notice that k_1 determines the final lateral displacement of the robot. Sample maneuvers generated by (30) and (31) are depicted in Figure 5. This parameterization captures lane change, lane keeping, and lane return maneuvers. The total dimension of (30), including time, is $n = n_Z + n_K + 1 = 7$, which is intractable for the FRS computation as in Section 3.2. However, the full system (30) is separable into “self-contained subsystems,” which we use in this section to compute the FRS of the full system.

The Rover’s footprint X_0 (as in Definition 3) is a rectangle, which we call an “expanded footprint,” that is large enough to contain all possible headings θ that the Rover can achieve. This means that, as in Remark 5, we let the dynamics of every point in the Rover’s footprint be equal to the dynamics of the center of mass. Though this approach is conservative, it makes it possible to decompose the system into self-contained subsystems. Recall that every point on the Rover’s body is subject to the rigid-body dynamics (3) in which the x and y states are coupled; however, these states are decoupled in (30) for the expanded footprint. Note that the Rover’s high-fidelity model (as in (1)) and controller for tracking Example 19’s trajectory-producing model are presented in Section 8.2.

4.1 Self-Contained Subsystems

This section describes how to decompose the trajectory-producing model (2) into two subsystems. We follow the methodology in [4, Section III A], adapting the notation and dynamics to system (2), which we refer to as the “full system.” Let the state, $\zeta \in Z$, be partitioned as $\zeta = (z_1, z_2, z_c)$ with $z_1 \in \mathbb{R}^{n_1}$, $z_2 \in \mathbb{R}^{n_2}$, $z_c \in \mathbb{R}^{n_c}$, $n_1, n_2 > 0$, $n_c \geq 0$, and

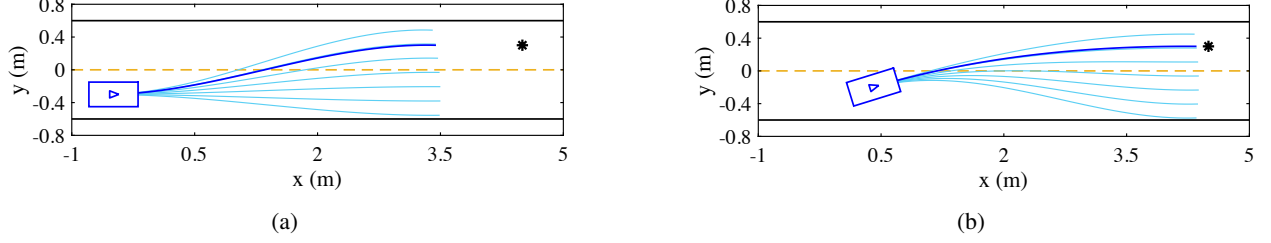


Figure 5: Sample of lane change trajectories generated by (30) with the control law in (31). The blue rectangle containing a triangle “pointer” represents the Rover and its initial heading. Initial headings of 0.0 and 0.3 are shown in subfigures (a) and (b), respectively. In subfigure (a), the Rover is driving straight in its lane and the sample trajectories consists of lane keeping and lane change maneuvers. In subfigure (b), the Rover has begun a lane change, and the sample trajectories consist of lane return maneuvers, and trajectories that complete a lane change. The parameters used are $T_h = 2$ s, $k_3 = 2$ m/s. The light blue trajectories are generated with a sample of values of k_1 and plotted over a time horizon of 2 s. The dark blue trajectory is the optimal trajectory to reach a desired waypoint (black asterisk).

$n_1 + n_2 + n_c = n_Z$. The states z_1 and z_2 belong to subsystems 1 and 2, respectively, and the states in z_c belong to both subsystems. Therefore, the dynamics can be written:

$$\begin{aligned}
 \dot{z}_1(t) &= f_1(t, z_1(t), z_2(t), z_c(t), k) \\
 \dot{z}_2(t) &= f_2(t, z_1(t), z_2(t), z_c(t), k) \\
 \dot{z}_c(t) &= f_c(t, z_1(t), z_2(t), z_c(t), k) \\
 \dot{k}(t) &= 0.
 \end{aligned} \tag{33}$$

Next define the subsystem states and spaces $\zeta_1 = (z_1, z_c) \in Z_1 \subset \mathbb{R}^{n_1+n_c}$ and $\zeta_2 = (z_2, z_c) \in Z_2 \subset \mathbb{R}^{n_2+n_c}$. The subspaces $Z_1, Z_2 \subset Z$ are compact and have semi-algebraic representations. Just as in Assumption 17, the initial conditions and state space of subsystem i are defined as:

$$Z_{0,i} = \{\zeta_i \in \mathbb{R}^{n_i+n_c} : h_{0_j}(\text{proj}^{-1}(\zeta_i)) \geq 0, \forall j = 1, \dots, n_0\} \tag{34}$$

$$Z_i = \{\zeta_i \in \mathbb{R}^{n_i+n_c} : h_{Z_j}(\text{proj}^{-1}(\zeta_i)) \geq 0, \forall j = 1, \dots, n_Z\} \tag{35}$$

for $i = 1, 2$. Recall that proj^{-1} is the back-projection operator from any subspace Z_i into Z as in (9). These definitions lead to the following lemma, which confirms that the projection and back-projection operators work “as expected” in mapping between Z and Z_i :

Lemma 20. [3, Section IV, Lemma 1] *Let $\zeta \in Z$, $\zeta_i = \text{proj}_{Z_i}(\zeta)$, and $S_i \subseteq Z_i$ for some subsystem, i . Then $\zeta_i \in S_i \iff \zeta \in \text{proj}^{-1}(S_i)$.*

Next, we restate the definition of a self-contained subsystem:

Definition 21. [4, Definition 5] *Consider the following special case of (33):*

$$\begin{aligned}
 \dot{z}_1(t) &= f_1(t, z_1(t), z_c(t), k) \\
 \dot{z}_2(t) &= f_2(t, z_2(t), z_c(t), k) \\
 \dot{z}_c(t) &= f_c(t, z_c(t), k) \\
 \dot{k}(t) &= 0.
 \end{aligned} \tag{36}$$

We call each of the subsystems with states defined as $\zeta_i = (z_i, z_c)$, for $i = 1, 2$, a self-contained subsystem (SCS). We call (36) the full system.

The SCS’s in (36) show that the evolution of each subsystem depends only on the subsystem states: $\dot{\zeta}_i$ depends only on $\zeta_i = (z_i, z_c, k)$. Notice that the trajectory parameters k can appear in both SCS’s. Given some initial condition

$\zeta_0 \in Z_0$, let, $\zeta : [0, T] \rightarrow Z$ be a trajectory of the full system (36). Similarly, if $\zeta_i : [0, T] \rightarrow Z_i$ is the trajectory of subsystem i , then ζ_i satisfies the following subsystem dynamics for all $t \in [0, T]$:

$$\begin{aligned} \dot{\zeta}_i(t) &= \begin{bmatrix} f_i(t, z_i(t), z_c(t), k) \\ f_c(t, z_c(t), k) \end{bmatrix} \\ \dot{k}(t) &= 0. \end{aligned} \quad (37)$$

Trajectories of the full system are related to the trajectories of the subsystem via the projection operator, $\text{proj}_{Z_i}(\zeta(t)) = \zeta_i(t)$, from (7) [4, Equation (12)].

To account for tracking error, each error function, g_i from Assumption 10, must be defined independently for each subsystem; meaning subsystems 1 and 2 are still SCS. The error function is added to (36) as defined below:

$$\begin{aligned} \dot{z}_1(t) &= f_1(t, z_1(t), z_c(t), k) + g_1(t, z_1(t), z_c(t), k) d(t) \\ \dot{z}_2(t) &= f_2(t, z_2(t), z_c(t), k) + g_2(t, z_2(t), z_c(t), k) d(t) \\ \dot{z}_c(t) &= f_c(t, z_c(t), k) + g_c(t, z_c(t), k) d(t) \end{aligned} \quad (38)$$

In the remainder of this section, we assume subsystems 1 and 2, with states $\zeta_1 = (z_1, z_c)$ and $\zeta_2 = (z_2, z_c)$, have dynamics defined in (38). Subsystems 1 and 2 are SCS's, and Lemma 20 and (7) hold.

Example 22. Recall the Rover's trajectory-producing model in (30). Solving (D^1) for this model is memory intensive since the total dimension is $n = 7$, as discussed at the end of Section 4.3. However, we can decompose this system into two separate SCS's:

$$\dot{\zeta}_1(t) = \begin{bmatrix} k_3 \cos(\theta(t)) - l_r \omega(t, k) \sin(\theta(t)) \\ \omega(t, k) \end{bmatrix} \quad (39)$$

$$\dot{\zeta}_2(t) = \begin{bmatrix} k_3 \sin(\theta(t)) + l_r \omega(t, k) \cos(\theta(t)) \\ \omega(t, k) \end{bmatrix} \quad (40)$$

where $\zeta_1 = [x, \theta]^\top \in Z_1$ and $\zeta_2 = [y, \theta]^\top \in Z_2$. We produce the trajectory-tracking model (13) for each SCS, by including error functions g_1 and g_2 as in Assumption 10; these are reported for the Rover in Section 8.2.

4.2 FRS Reconstruction

Since subsystems 1 and 2 are SCS's, an FRS can be found for each using (D) . Denote the two applications of (D) as (D_1) and (D_2) , respectively. This section proves that the intersection of the back-projections of the FRS's of each subsystem is an outer approximation to the FRS of the full system. We refer to the intersection of back-projections as reconstruction, which we implement with SOS programming.

Let (v_1, w_1, q_1) (resp. (v_2, w_2, q_2)) be a feasible solution to (D_1) (resp. (D_2)). An outer approximation of X_{FRS} can be reconstructed with the following optimization program:

$$\inf_{v_r, w_r} \int_{X \times K} w_r(x, k) d\lambda_{X \times K} \quad (41)$$

$$w_r(x, k) + v_r(t, \zeta, k) \geq 0 \quad \forall (t, \zeta, k) \in X \times Z \times K \quad (42)$$

$$-v_r(t, \zeta, k) + v_1(t, \zeta_1, k) + v_2(t, \zeta_2, k) \geq 0 \quad \forall (t, \zeta, k) \in [0, T] \times Z \times K \quad (43)$$

$$w_r(x, k) + 1 \geq 0 \quad \forall (x, k) \in X \times K, \quad (44)$$

where $x = \text{proj}_X(\zeta)$. Theorem 23 proves that the solution to (41) contains the FRS.

Theorem 23. Let (v_r, w_r) be a feasible solution to (41), then X_{FRS} is a subset of the 0-superlevel set of w_r .

Proof. Let $\zeta_0 \in Z_0$, $k \in K$, and $d \in L_d$ be arbitrary such that $\zeta : [0, T] \rightarrow Z$ is a trajectory of the full system (36). Let $\zeta_1(t) = \text{proj}_{Z_1}(\zeta(t))$ give the corresponding trajectory of subsystem 1, and similarly ζ_2 gives the trajectory of subsystem 2. Recall that (v_1, w_1, q_1) is a feasible solution to (D_1) , which is (D) solved with the dynamics of subsystem 1. By Lemma 14, $v_1(t, \zeta_1(t), k)$ is non-positive and decreasing along the trajectory ζ_1 for every $t \in [0, T]$, and similarly $v_2(t, \zeta_2(t), k) \leq 0$ for ζ_2 . Therefore, $v_1(t, \zeta_1, k) + v_2(t, \zeta_2, k) \leq 0$ along both trajectories, ζ_1 and ζ_2 . By Lemma 20, since

the full system (36) is decomposable, $\zeta(t) \in \text{proj}^{-1}(\zeta_1(t)) \cap \text{proj}^{-1}(\zeta_2(t))$. This means that, by (43), $v_r(t, \tilde{\zeta}, k) \leq 0$ for any $\tilde{\zeta} \in \text{proj}^{-1}(\zeta_1(t)) \cap \text{proj}^{-1}(\zeta_2(t))$. This implies that $v_r(t, \zeta(t), k) \leq 0$ along the trajectory ζ for all $t \in [0, T]$, i.e. v_r is non-positive and decreasing along trajectories of the full system (36). Then, by (42), $w_r(x, k) \geq 0$ if $x = \text{proj}_X(\zeta(t))$. Since ζ_0 , k , and d were arbitrary, we are done. \blacksquare

Note that the notion of intersecting the back-projections of the subsystem FRS's is implied by the fact that $v_1 + v_2$ is non-positive along trajectories of the full system. However, $v_1 + v_2$ can also be non-positive on points in the state space that are not reached by the full system; in other words, this method is conservative. We show on the Rover hardware in Section 10 that this conservatism does not lead to poor performance in practice. Figure 6 shows the intersection of back-projections of the subsystem FRS's for the Rover.

4.3 Implementation

In Section 3.2 solving (D) is shown to be intractable for systems such as (30) from Example 19. Here, we implement a relaxation of (41) with SOS polynomials. We show that the system decomposition method reduces the upper bounds on memory usage.

Suppose $l \in \mathbb{N}$, and suppose (v_1^l, w_1^l, q_1^l) and (v_2^l, w_2^l, q_2^l) are feasible solutions to (D_1^l) and (D_2^l) , which are (D^l) applied to Subsystems 1 and 2 respectively. Recall the sets H_T, H_Z, H_K , and H_X from Section 3.1, which contain the polynomials defining the sets $[0, T]$, Z , K , and X respectively. Let $\alpha \in \mathbb{N}$ and $\alpha \geq l$. We pose the following SDP to reconstruct the FRS:

$$\begin{aligned} \inf_{v_r^\alpha, w_r^\alpha} \quad & y_{X \times K}^\top \text{vec}(w_r^\alpha) & (45) \\ & w_r^\alpha + v_r^\alpha & \in Q_{2\alpha}(H_T, H_Z, H_K) \\ & -v_r^\alpha + v_1^l + v_2^l & \in Q_{2\alpha}(H_T, H_Z, H_K) \\ & w_r^\alpha + 1 \geq 0 & \in Q_{2\alpha}(H_X, H_K) \end{aligned}$$

where $x = \text{proj}_X(\zeta)$, $w_r^\alpha \in \mathbb{R}_{2\alpha}[x, k]$, and $v_r^\alpha \in \mathbb{R}_{2\alpha}[t, \zeta, k]$. As in (D^l) , the vector $y_{X \times K}$ contains moments associated with the Lebesgue measure $\lambda_{X \times K}$, so $\int_{X \times K} w_r^\alpha(x, k) d\lambda_{X \times K} = y_{X \times K}^\top \text{vec}(w_r^\alpha)$ for $w \in \mathbb{R}_{2\alpha}[x, k]$ [30].

The proposed system decomposition approach reduces memory usage in two ways. First, solving (D^l) for each subsystem reduces the problem dimension for fixed degree, which exponentially reduces memory usage [30, Section 4.2]. Second, the reconstruction program (45), has 3 SOS constraints compared to 7 in (D^l) , so we expect (45) to use approximately 3/7 of the memory that (D^l) requires. Let $n = n_Z + n_K + 1$ denote the total problem dimension as in Section 3.2.2. Recall (29), which computes the number of free variables in (D^l) , which dictates memory usage. Solving (D^l) with $n = 7$ and $l = 3$ results in N_{free} that is approximately 6.0×10^4 , which is the largest degree we found tractable in practice on a computer with 1.5 TB of RAM. However, this produces a conservative outer approximation of the FRS as depicted in Figure 7. For comparison, $n = 7$ and $l = 4$ results in N_{free} of approximately 2.2×10^5 for (D^l) . On the other hand, solving (D^l) with $n = 6$ and $l = 4$ for two subsystems results in N_{free} of approximately 1.0×10^5 per subsystem. Then, solving (45) with $n = 7$ and $l = 5$ results in N_{free} of approximately 4.1×10^4 .

5 Conditions for Safety and Persistent Feasibility

In this section, we state properties of a robot's environment, sensors, computation speed, and braking behavior that are required to ensure that planning with RTD is safe and persistently feasible. We lower bound the planning time horizon in Remark 33. The main result in this section is Theorem 35, which provides a lower bound on sensor performance to guarantee safety and persistent feasibility.

5.1 Obstacles and Sensors

Definition 24. An obstacle is a compact, connected subset of X that must be avoided by the robot, and is assumed to be static with respect to time. At any instance in time, there is a finite, maximum number of obstacles n_{obs} within the robot's sensor horizon.

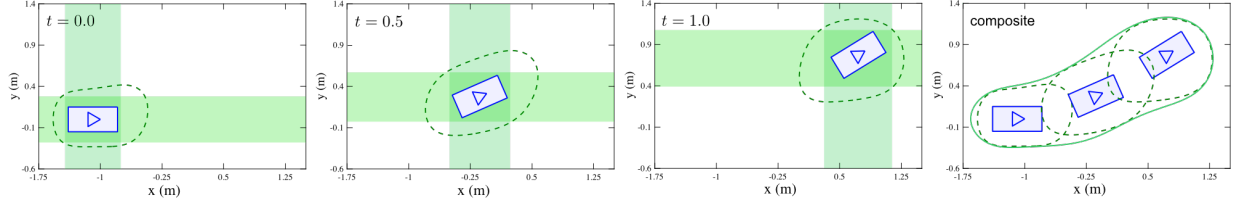


Figure 6: Example of the system decomposition and reconstruction for the FRS of the Rover's trajectory-producing system (30). The robot is the blue rectangle with a triangle indicating its heading. The FRS and robot at 0.0, 0.5, and 1.0 s following a trajectory with parameters $k = (1.1 \text{ rad/s}, 0.0 \text{ rad}, 2.0 \text{ m/s})$ are depicted from left to right. The green bars show back-projections of the 0 sub-level sets of v_i^4 by (D_i^4) for $i = 1, 2$. The interior of the dashed green contour is the 0 sub-level set of v_r^5 computed with (45). The far right figure shows the same level sets of v_r^5 , along with the 0 super-level set of w_r^5 as a solid line. Notice that the 0-level set of w_r^5 outer-approximates all of the 0-level sets of v_r^5 .

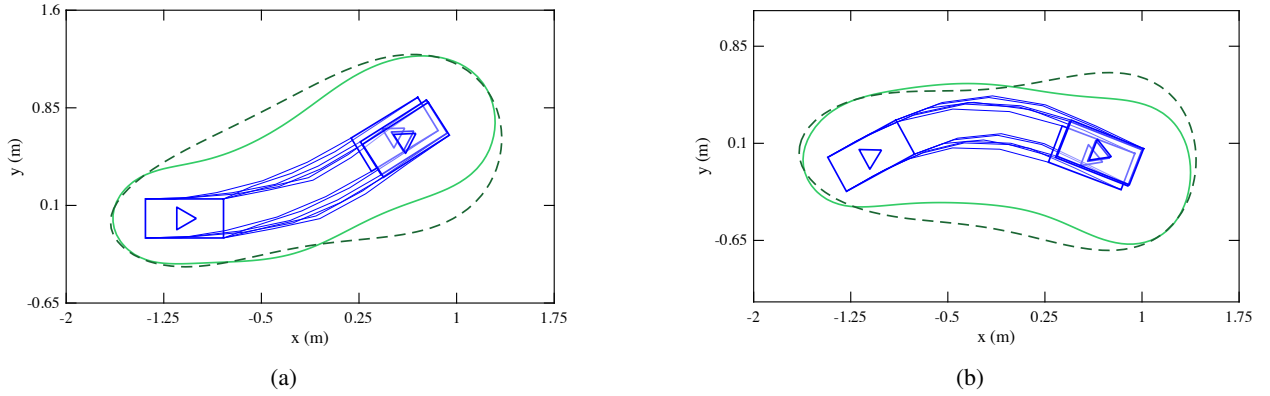


Figure 7: Comparison of reach sets computed for lane change trajectories produced by (30). The dark green, dashed contours represent the 1-level set of w^3 computed for the full system. The light green contours represent the 0-level set of w_r^5 , computed using the system decomposition and reconstruction methods. For each FRS, the robot's footprint is a bounding box that captures the robot's pose (blue rectangle) for any heading in $[-0.5, 0.5]$ rad. The reach sets are computed with a time horizon of 1 s. Notice that the FRS computed with system decomposition is almost entirely contained within the FRS that does not use system decomposition; so, system decomposition reduces conservatism by enabling the computation of a higher-degree FRS. The blue trajectories are generated by simulating the high-fidelity model described in Example 19 for a range of initial velocities and yaw rates. Subfigure (a) shows the trajectory parameter $k = [1.1 \text{ rad/s}, 0.0 \text{ rad}, 2.0 \text{ m/s}]^T$ with initial velocities and yaw rates of $\{1.0, 1.5, 2.0\} \text{ m/s}$ and $\{-0.65, 0.00, 1.50\} \text{ rad/s}$. Subfigure (b) shows the trajectory parameter $k = [-1.5 \text{ rad/s}, 0.5 \text{ rad}, 2.0 \text{ m/s}]^T$ with initial velocities and yaw rates of $\{1.0, 1.5, 2.0\} \text{ m/s}$ and $\{-1.5, 0.0\} \text{ rad/s}$.

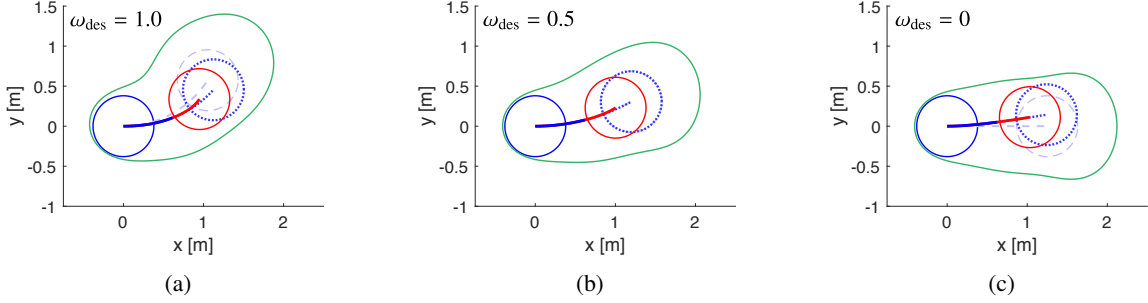


Figure 8: The Segway robot, with dynamics described in Example 7, while tracking trajectories planned in the xy -subspace X using the trajectory-producing model (16). The robot begins with $[x_0, y_0]^T = [0, 0]^T$ and the initial heading $\theta(0) = 0$ rad pointing to the “right.” The robot has a circular footprint with radius 0.38 m, and the initial state in all three subfigures is $[x_c, y_c, \theta, \omega, v]^T = [0 \text{ m}, 0 \text{ m}, 0 \text{ rad}, 0.5 \text{ rad/s}, 1.25 \text{ m/s}]^T$, plotted in X as the solid blue circle. The desired yaw rate ω_{des} (the trajectory parameter k_1 in Example 31), is listed in each subfigure; the desired speed (the parameter k_2 in Example 31) is $v_{\text{des}} = 1.25$ m/s in all three subfigures. The desired trajectory, with time horizon $T = 1$ s, is shown in dashed light blue, with the robot’s footprint in dashed light blue plotted at the end. The robot’s center-of-mass trajectory (of the high-fidelity model (4) under the action of the tracking controller u_k in (5) and (6)) is shown in solid blue until, at $t = 0.5$ s, the robot begins using the braking controller from (53) and (54) in Example 31. The braking trajectory is solid red; the robot is plotted in red where it comes to a stop. The trajectory of the robot using u_k for $t \in [0.5, 1]$ s (as opposed to switching to u_{brake}) is shown in dotted blue. The green contour is the FRS spatial projection for each ω_{des} (using the map π_X^l from (47) with $l = 6$ and the FRS computed for (16)). Notice that the braking trajectory stays within the FRS, as required by Assumption 32.

Without loss of generality, we assume that the number of obstacles within the robot’s sensor horizon at every instance in time is equal to n_{obs} . If there are fewer than n_{obs} obstacles, then we treat the remaining obstacles as the empty set. We now define how the robot senses obstacles.

Assumption 25. *The robot has a finite sensor horizon D_{sense} , which is a radius around the robot within which all obstacles are observed. Occlusions and unexplored areas outside the sensor horizon are treated as static obstacles at each planning instance. During operation, obstacles appear from outside the robot’s sensor horizon and are sensed as soon as they are within the horizon; obstacles do not spontaneously appear within the sensor horizon.*

In addition to describing how obstacles are perceived, we also assume there is a maximum amount of computation time available to sense an obstacle and design a trajectory:

Assumption 26. *The time required to process sensor data has a finite upper bound, τ_{process} . In addition, there is a maximum allowed execution time for trajectory planning, τ_{trajopt} . We define the planning time $\tau_{\text{plan}} = \tau_{\text{process}} + \tau_{\text{trajopt}}$. We also require that the planning time horizon T is greater than or equal to τ_{plan} . Recall Assumption 9; there exists $\tau > 0$ such that, at each time t , the robot’s current state estimate and future state prediction are bounded by $\varepsilon_i \geq 0$ in each state $\zeta_{\text{hi},i}$ for all time in $[t, t + \tau]$. We assume that $\tau \geq \tau_{\text{plan}}$.*

In practice, most modern obstacle detectors have a bounded processing time for camera, lidar, or radar data [20, 27]. Though we do not prove that the trajectory planning time of the proposed method is bounded, we do enforce a time limit of τ_{plan} on online computation, after which it is terminated. We also require that the following obstacle processing step happens before trajectory planning.

Assumption 27. *By Assumption 9, the robot’s current state estimate is bounded by ε_x in the x -coordinate and ε_y in the y -coordinate. We assume that any sensed obstacle $X_{\text{sense}} \subset X$ is expanded by $\pm\varepsilon_x$ (resp. $\pm\varepsilon_y$) in the x (resp. y) direction before being passed to the trajectory planner, i.e.*

$$X_{\text{obs}} = X_{\text{sense}} \oplus \left\{ [-\varepsilon_x, \varepsilon_x] \times [-\varepsilon_y, \varepsilon_y] \right\} \quad (46)$$

is the set passed to the trajectory planner, where \oplus indicates the Minkowski sum, i.e., $A \oplus B = \{a + b \mid a \in A, b \in B\}$.

As noted in Remark 11, by Assumption 27, if we were able to plan trajectories with the high-fidelity model, then any trajectory with its spatial component outside of X_{obs} as in (46) would be safe despite state estimation error.

5.2 Safety and Persistent Feasibility

Here, we address what it means for RTD to be safe and persistently feasible. Recall that RTD uses a receding-horizon strategy wherein it selects a new parameter k at each planning iteration. We create a “non-intersection condition” for safety in each planning iteration by stating how a safe subset of the FRS must not intersect with any obstacles. We then prescribe how the robot must brake, and how long its sensor horizon must be, to ensure persistent feasibility between planning iterations.

5.2.1 The Non-Intersection Condition for Safety

For safety, first note that we compute an FRS for trajectories of the trajectory-tracking model (13), as shown in [22] and in Section 3 of this paper. We can think of the FRS as a map that associates trajectory parameters in K with reachable points in X . Suppose that the tuple (v, w, q) is an optimal solution to (D) from Section 3.1. Then by Lemma 15, $w : X \times K \rightarrow \{0, 1\}$ is an indicator function on \mathcal{X}_{FRS} . Define the FRS spatial projection map $\pi_X : K \rightarrow \mathcal{P}(X)$ that acts on a parameter $k \in K$ as

$$\pi_X(k) = \{x \in X \mid w(x, k) = 1\}, \quad (47)$$

which returns the set in X of all points that are reachable by the robot’s trajectory-tracking model (13) at any time in $[0, T]$. This map lets us define safety in each plan:

Definition 28. *Suppose that $X_{\text{obs}} \subset X$ is a set of obstacles as in Definition 24. Then, at each planning iteration, we must pick a k for which the FRS does not intersect any obstacles, i.e., $\pi_X(k) \cap X_{\text{obs}} = \emptyset$. This non-intersection condition defines safety when planning with RTD.*

Now, recall that we cannot solve (D) exactly; but, suppose that the tuple (v^l, w^l, q^l) is an optimal solution to (D^l) from Section 3.1 for some fixed degree $l \in \mathbb{N}$. As per Remark 18, 1-superlevel sets of $w^l : X \times K \rightarrow \mathbb{R}$ contain \mathcal{X}_{FRS} . The map $\pi_X^l : K \rightarrow \mathcal{P}(X)$ is defined as:

$$\pi_X^l(k) = \{x \in X \mid w^l(x, k) \geq 1\}. \quad (48)$$

By Remark 18, for any $k \in K$, $\pi_X^l(k) \supseteq \pi_X(k)$, i.e., this map over-approximates the FRS. Therefore, $k \in K$ is safe for the high-fidelity model to track if $\pi_X^l(k) \cap X_{\text{obs}} = \emptyset$.

Definition 29. *Any k for which $\pi_X^l(k) \cap X_{\text{obs}} = \emptyset$ is called a safe plan.*

See Algorithm 2 in Section 7 for how we use this non-intersection condition online.

5.2.2 Braking and Sensing for Persistent Feasibility

Next, we define persistent feasibility using the idea that the robot must brake “along” a previously-planned safe trajectory. First, recall that each trajectory parameterized by k is of duration T . Suppose that X_{obs} is an obstacle and, at time 0, we have a safe plan given by k_0 , as in Definition 29. We only know that k_0 is safe for $t \in [0, T]$, but persistent feasibility requires us to ensure safety for all $t \geq 0$. While tracking k_0 , the robot must simultaneously plan its next trajectory, i.e., find some k_1 for which $\pi_X^l(k_1) \cap X_{\text{obs}} = \emptyset$. By Assumption 26, the robot has a duration of $\tau_{\text{plan}} < T$ to find k_1 . If a safe k_1 is not found by τ_{plan} , the only way for the robot to be safe for all $t > \tau_{\text{plan}}$ is to brake to a stop. Since $\pi_X^l(k_0) \cap X_{\text{obs}} = \emptyset$, we require that the robot brakes within the set $\pi_X^l(k_0)$, i.e., it brakes “within the FRS.” This section describes how we ensure that the braking maneuver when applied at τ_{plan} can always be applied to ensure safety.

We begin by defining “braking” and “non-braking” trajectories. Recall that, for any $k \in K$, the robot is able to generate a feedback controller u_k as in (10). So, for any $\zeta_{\text{hi},0} \in Z_{\text{hi},0}$ and $k \in K$, the robot’s non-braking trajectory, given by the high-fidelity model, (1) can be written as $\zeta_{\text{hi}} : [0, T] \rightarrow Z_{\text{hi}}$ for which

$$\zeta_{\text{hi}}(t; \zeta_{\text{hi},0}, k) = \zeta_{\text{hi},0} + \int_0^t f_{\text{hi}}(t, \zeta_{\text{hi}}(t), u_k(t, \zeta_{\text{hi}}(t))) dt. \quad (49)$$

We now state how the robot brakes:

Assumption 30. At time 0, let the robot, with high-fidelity dynamics (1), be at an arbitrary initial condition $\zeta_{hi,0}$ and about to track an arbitrary $k \in K$. We assume that there exists a finite braking time given by $\tau_{brake} : Z_{hi,0} \times K \rightarrow \mathbb{R}_{\geq 0}$, within which the robot comes to a stop under the action of the braking controller,

$$u_{brake} : [0, \infty) \times Z_{hi} \rightarrow U. \quad (50)$$

If the braking controller is applied at τ_{plan} then for any $\hat{\tau} > \tau_{plan} + \tau_{brake}(\zeta_{hi,0}, k)$ the robot will be stopped:

$$\text{proj}_V(f_{hi}(\hat{\tau}, \zeta_{brake}(\hat{\tau}), u_{brake}(\hat{\tau}), \zeta_{brake}(\hat{\tau}))) = 0, \quad (51)$$

where $V \subset Z_{hi}$ is the subspace of the state space corresponding to the yaw rate and speed states as described in Assumption 6.

In Assumption 30, the robot's braking time τ_{brake} is finite for every initial condition and trajectory parameter. So, there exists a maximum stopping time τ_{stop} , given by:

$$\tau_{stop} = \max_{\zeta_{hi,0} \in Z_{hi,0}, k \in K} \tau_{brake}(\zeta_{hi,0}, k), \quad (52)$$

where the maximum is achieved because $Z_{hi,0}$ and K are compact by Assumption 2. We can use τ_{stop} to design a braking controller as in the following example.

Example 31. Consider again the Segway's high-fidelity model from Example 7. Notice that the yaw and longitudinal speed dynamics are decoupled with respect to the control inputs. Therefore, we can find τ_{stop} as in (52) by measuring the time it takes for the robot to stop from any initial condition where the speed is $v(0) = v_{max}$ as in Assumption 6, and the desired speed $v_{des} = 0$ is passed to the longitudinal acceleration controller (6).

With τ_{stop} established, we can design a braking controller. Suppose that the robot is applying a controller as in (5) and (6) to track a trajectory with desired yaw rate k_1 and desired speed k_2 , over the time span $t \in [0, \tau_{plan})$. Then, for $t \in [\tau_{plan}, \tau_{plan} + \tau_{stop}]$, the controller $u_{brake} = [\gamma_{brake}, \alpha_{brake}]^T$ is applied, given by

$$\gamma_{brake}(t, \zeta_{hi}) = \min\{\bar{\gamma}, \max\{\underline{\gamma}, ((\tau_{plan} + \tau_{stop}) - t) \cdot (\beta_\gamma(k_1 - \omega(t)) + \beta_\theta(\theta(t) - \theta_{des}(t)))\}\} \quad (53)$$

$$\alpha_{brake}(t, \zeta_{hi}) = \min\{\bar{\alpha}, \max\{\underline{\alpha}, (\beta_\alpha + \beta_v)(0 - v(t))\}\}. \quad (54)$$

where $\theta_{des}(t) = k_1 t$ as before. As $t \rightarrow (\tau_{plan} + \tau_{stop})$, this controller brakes to a desired speed of 0, and linearly decreases the yaw acceleration that would be commanded by u_k in (5).

Now, we formally state what is meant by braking "within the FRS."

Assumption 32. Consider an arbitrary initial condition $\zeta_{hi,0}$ at time 0, and arbitrary $k \in K$. Suppose the robot, described by the high-fidelity dynamics (1), tracks k for $t \in [0, \tau_{plan})$, then applies the braking controller (50) for $t \geq \tau_{plan}$. We assume that, at every $t \in [\tau_{plan}, \tau_{plan} + \tau_{brake}(\zeta_{hi,0}, k)]$, the spatial component of the robot's braking trajectory $\zeta_{brake} : [0, T] \rightarrow Z_{hi}$ lies within the set of points reachable by trajectory-tracking model:

$$\text{proj}_X(\zeta_{brake}(t)) \in \pi_X(k). \quad (55)$$

Note that, since $\zeta_{hi,0}$ is arbitrary, Assumption 32 requires every point on the robot's body stays within $\pi_X(k) \subset X$ when braking, as per Assumption 4. Notice that Assumption 32 can only be fulfilled if the time horizon T is long enough that, for any k , the non-braking trajectories in the set $\pi_X(k)$ are spatially longer than the robot's maximum braking distance corresponding to that k . We can satisfy this as follows.

Remark 33. Recall τ_{stop} from (52). In [22, Theorem 10], τ_{stop} is used to lower-bound the planning time horizon T . If T is larger than $\tau_{plan} + \tau_{stop}$, and the robot at time 0 has a safe plan of length $\tau_{plan} + \tau_{stop}$, then the robot always has enough time to brake if it cannot find a new safe trajectory within τ_{plan} . Note that τ_{stop} may be large; if $T \geq \tau_{plan} + \tau_{stop}$, the robot will travel farther along a non-braking trajectory than along a braking trajectory from the same initial condition. However, we can pick $T < \tau_{plan} + \tau_{stop}$ empirically, by ensuring that T is long enough such that, for any $k \in K$, the robot travels at least as far as its braking distance along a non-braking trajectory of duration T .

We illustrate how to pick $T < \tau_{plan} + \tau_{stop}$ by continuing the previous Segway example.

Example 34. Consider computing an FRS for the Segway from Example (7) with $v_{\max} = 1.25$ m/s and $\tau_{\text{plan}} = 0.5$ s. On the hardware, we find empirically that stopping from 1.25 m/s requires $\tau_{\text{stop}} \approx 1.5$ s, over a stopping distance of no more than 0.625 m. If we set $T = \tau_{\text{plan}} + \tau_{\text{stop}}$, the robot's non-braking trajectories would be up to $T \cdot v_{\max} = 2.5$ m long. However, suppose we choose a number $\tau_v = (0.625 \text{ m}) / (1.25 \text{ m/s}) = 0.5$ s, and then set $T = \tau_{\text{plan}} + \tau_v = 1$ s. Then, non-braking trajectories would be at most 1.25 m long, which leaves enough distance in the FRS for the robot to stop if it begins braking after traveling for $\tau_{\text{plan}} \cdot v_{\max} = 0.625$ m.

A detailed discussion of τ_v is in Appendix 12.

Now, to ensure that the robot is safe for all t , i.e., that the trajectory planning procedure is persistently feasible, we need to enforce a lower bound on the robot's sensor horizon D_{sense} (from Assumption 25). This is to ensure that the robot senses obstacles that are far enough away that it can plan a safe non-braking trajectory of duration T every τ_{plan} seconds. The following result is a modified version of [22, Theorem 10].

Theorem 35. Let $X_{\text{obs}} \subset X$ be a set of obstacles as in Definition 24. Let v_{\max} be the robot's maximum speed as in Assumption 6. Let τ_{plan} be the planning time as in Assumption 26. Suppose that T is large enough that Assumption 32 holds; so, for any $\zeta_{\text{hi},0} \in Z_{\text{hi},0}$ and any $k \in K$, the spatial component of the robot's braking trajectory lies within $\pi_X(k)$. At time 0, suppose that the robot has a safe plan $k_0 \in K$ (as in Definition 29). Recall that ε_x and ε_y are the robot's maximum state estimation error in the x and y coordinates of X as in Assumption 9, and let $\varepsilon = \sqrt{\varepsilon_x^2 + \varepsilon_y^2}$. Suppose the sensor horizon D_{sense} obeys Assumption 25 and satisfies

$$D_{\text{sense}} \geq (T + \tau_{\text{plan}}) \cdot v_{\max} + 2\varepsilon. \quad (56)$$

Then, the robot can find either find a new safe plan every τ_{plan} seconds, or can brake safely if no new safe plan is found.

Proof. In this proof, we check that the robot can brake within any safe plan, and that it can sense obstacles far away enough to safely plan around them.

First, we check that the robot can begin braking safely at any time $t = j \cdot \tau_{\text{plan}}$ where $j \in \mathbb{N}$. Recall that the robot replans over each time horizon $[j \cdot \tau_{\text{plan}}, (j+1) \cdot \tau_{\text{plan}}]$, so it will either have a new safe plan k_j or will begin braking at each $t = j \cdot \tau_{\text{plan}}$. We know that the robot is safe over $t \in [0, T]$ by the premises, and it can brake safely (i.e., within $\pi_X(k_0)$ by Assumption 32). Similarly, if the robot has a safe plan of duration T at $t = j \cdot \tau_{\text{plan}}$, then the robot can still brake safely if a new safe plan cannot be found before $(j+1) \cdot \tau_{\text{plan}}$.

Now, we check that the sensor horizon in (56) is large enough for the robot to sense all possible obstacles that are reachable at each $t = j \cdot \tau_{\text{plan}}$ despite state estimation error. Recall that the obstacles are static by Definition 24 and that, by Assumption 9, at any time t , the robot can predict its future position at $t + \tau_{\text{plan}}$ to within a box of size $\varepsilon_x \times \varepsilon_y$. Also recall that, by Assumption 27, a sensed obstacle X_{sense} is expanded as in (46) to the set X_{obs} to compensate for state estimation error. So, at each time $t = j \cdot \tau_{\text{plan}}$ the robot must plan with respect to all obstacles that are reachable within the time horizon T from the robot's future position at $t = (j+1) \cdot \tau_{\text{plan}}$. This means that a safe plan k_{j+1} found over the time horizon $[j \cdot \tau_{\text{plan}}, (j+1) \cdot \tau_{\text{plan}}]$ must avoid all obstacles within the distance $D_T = T \cdot v_{\max} + \varepsilon$ of the robot's future position at $t = (j+1) \cdot \tau_{\text{plan}}$. Notice that the maximum possible distance between the robot's position at $j \cdot \tau_{\text{plan}}$ and at $t = (j+1) \cdot \tau_{\text{plan}}$ is $D_{\text{plan}} = \tau_{\text{plan}} \cdot v_{\max} + \varepsilon$. Therefore, at each time $t = j \cdot \tau_{\text{plan}}$, the robot must sense all obstacles that are within the distance $D_{\text{plan}} + D_T = \tau_{\text{plan}} \cdot v_{\max} + T \cdot v_{\max} + 2\varepsilon$. Since $D_{\text{sense}} \geq (T + \tau_{\text{plan}}) \cdot v_{\max} + 2\varepsilon$ and the robot senses all obstacles within D_{sense} at $t = j \cdot \tau_{\text{plan}}$, we are done. ■

Theorem 35 guarantees that the proposed RTD method is safe and persistently feasible. Next, we address how to represent obstacles so that the online planning algorithm, i.e., picking a new trajectory parameter $k \in K$ at every iteration, can be done in real time.

6 Obstacle Representation

This section presents a method of representing the robot's environment to enable real-time performance of RTD. Different obstacle representations can result in large variations in computation time for a path planner. It has been shown in the literature that safe path plans around continuous obstacles can be computed by first running an SDP to eliminate controllers that may cause a collision, then optimizing over the remaining controllers [22, 29]. But, the procedure is too slow for real-time path planning, which we show in Section 6.1. To address this shortcoming, the

remainder of this section presents a discrete obstacle representation that reduces computation time while preserving safety. We use the following definition of safety to relate obstacles directly to trajectory parameters:

Definition 36. *Given an obstacle $X_{\text{obs}} \subset X$, let K_{safe} denote the set of safe trajectory parameters. No point on the robot's body, described by the high dimensional model (1), can collide with the obstacle when tracking a trajectory parameterized by any $k \in K_{\text{safe}}$.*

The majority of the section is devoted to finding several scalars that relate the geometry of the robot and obstacles. These scalars, which can be computed offline, are subsequently used to construct a discrete obstacle representation. The main result in this section is Theorem 68, which proves that representing obstacles with the proposed discretization preserves the safety guarantees of RTD.

6.1 Set Intersection

Path planning can be performed by optimizing an arbitrary cost function over $k \in K_{\text{safe}}$, which is described in Section 7. However, this requires determining K_{safe} at run-time. It is shown in [22] that a set intersection procedure can be used to approximate K_{safe} using an SDP, as mentioned in Section 3. Here, we demonstrate that set intersection is too slow for real-time operation.

Suppose $X_{\text{obs}} \subset X$ is an obstacle represented as a semi-algebraic set, with the list of polynomials $H_{\text{obs}} = \{h_{i,\text{obs}}\}_{i=1}^{n_{\text{obs}}} \subset \mathbb{R}[x]$. Then [22, Program (19)] is used to find a polynomial $h \in \mathbb{R}[k]$ that is provably an inner approximation of K_{safe} . Here, we restate [22, Program (21)], which implements set intersection using SOS programming. Suppose that w^l is a solution to (D^l) from Section 3.2. Then, picking $l' \in \mathbb{N}$, we find the SOS polynomial $h \in Q_{2l'}(H_K) \subset \mathbb{R}[k]$ with the program

$$\begin{aligned} \inf_h \quad & y_K^\top \text{vec}(h) & (57) \\ & 1 - w^l - h & \in Q_{2l'}(H_{\text{obs}}, H_K) \\ & h & \in Q_{2l'}(H_K). \end{aligned}$$

This program is translated into an SDP at runtime. Notice that, given its size and simplicity, this program does not have the same memory usage problems as the FRS computation (see Section 3.2.2). However, this program may run slowly depending upon the obstacle representation in the set H_{obs} , as we describe next.

To determine the speed of the set intersection SDP, we ran (57) 100 times with H_{obs} representing a single 2-D, box-shaped obstacle at a random position, similar to what is used in the simulation results of Section 9. As with (D^l) in Section 3.2, we implement this SDP using MATLAB's Spotless toolbox [43], and solve the resulting conic program with MOSEK [31]. Running (57) on the box obstacles takes a mean solve time of 17.8 s. We also ran Program (57) 100 times with H_{obs} representing a single, randomly-generated 1-D line-segment obstacle in each trial. We test this type of obstacle because more complex obstacles can be constructed from line segments, as shown in [22]. The polynomial w^l is taken from the solution to (D^l) for the FRS of the Segway dynamics from Example 7 (see Section 8.1 for further details). The program solves in 1.05 s on average. These numbers are also reported in Table 1. The set intersection timing results show that representing a polygonal obstacle with a collection of line segment obstacles is faster than representing the obstacle as a 2-D semi-algebraic set. However, even a line segment representation would require approximately 4 s to solve (57) for a single box, because the solve time increases linearly with the number of line segments as per [22].

The remainder of Section 6 presents a discretized obstacle representation that eliminates the need for set intersection, and allows for the online trajectory optimization to run in real time. For comparison with set intersection, we tested the proposed method (see Algorithm 1 in Section 6.4) to discretize each box and line obstacle from the test of (57) described above. We evaluated w^l on the resulting discrete set of points to produce a list of nonlinear constraints that overapproximate K_{safe} (as proven in Theorem 68 in Section 6.4). The proposed method is three orders of magnitude faster than set intersection, as reported in Table 1.

6.2 FRS Projections

To relate obstacles to unsafe trajectories, we project the robot's FRS into the state space and trajectory parameter space. Recall that obstacles are sets $X_{\text{obs}} \subset X$, where $X \subset Z$ is the xy -subspace of the trajectory producing model's state

Set Intersection vs. Obstacle Discretization			
Obstacle Shape	Method	Mean Time [ms]	Std. Dev [ms]
Box	Set Intersection [22]	17,800	1010
Line	Set Intersection [22]	1050	73
Box	Discretization (proposed)	4	7
Line	Discretization (proposed)	3	2

Table 1: Timing results of the set intersection procedure from [22] versus the proposed obstacle discretization procedure, both of which provably represent the set K_{safe} of safe trajectory parameters to be used for online optimization. The proposed method is two orders of magnitude faster.

space Z . Also recall the FRS spatial projection map $\pi_X : K \rightarrow \mathcal{P}(X)$ in (47), which maps a set of trajectory parameter $k \in K$ to all points of X that are reachable within the time horizon $[0, T]$ by the robot’s trajectory-tracking model (13). We define a related map π_K that maps a subset X' of X to the set $\pi_K(X') \subset K$ for which any trajectory tracking some $k \in \pi_K(X')$ travels through at least one point in X' .

Suppose that the tuple (v, w, q) is an optimal solution to Program (D) from Section 3.1. Then by Lemma 15, $w : X \times K \rightarrow \{0, 1\}$ is an indicator function on X_{FRS} . Define the set-valued map $\pi_K : \mathcal{P}(X) \rightarrow \mathcal{P}(K)$ as

$$\pi_K(X') = \{k \in K \mid \exists x \in X' \text{ s.t. } w(x, k) = 1\}. \quad (58)$$

We call π_K the FRS parameter projection operator. If $X' \subset X$, we say that $\pi_K(X')$ are the parameters corresponding to X' . We use the word “projection” for these operators to relate them to the projection operators proj_{Z_i} in Definition 8. Recall that proj_{Z_i} returns points in a subspace Z_i of the state space Z_{hi} that are identified by an identity relationship. Similarly, π_X and π_K return points in a subspace of the reachable set X_{FRS} that are identified by the indicator function w . The following lemma demonstrates the utility of π_K .

Lemma 37. *Consider an arbitrary point $p \in X \setminus X_0$. Let $k \in \pi_K(p)^C$. At $t = 0$, let the robot, described by the high-fidelity model (1), be at the state $\zeta_{\text{hi},0} \in Z_{\text{hi}}$. Suppose the robot tracks the trajectory parameterized by k , producing the high-fidelity model trajectory $\zeta_{\text{hi}} : [0, T] \rightarrow Z_{\text{hi}}$. Then, no point on the robot’s body ever reaches p . More precisely, there does not exist any pair $(t, \zeta_{\text{hi},0}) \in [0, T] \times Z_{\text{hi},0}$ such that $p = \text{proj}_X(\zeta_{\text{hi}}(t))$.*

Proof. Suppose for the sake of contradiction that there exists some $t \in [0, T]$ and $\zeta_{\text{hi},0} \in Z_{\text{hi},0}$ for which $p = \text{proj}_X(\zeta_{\text{hi}}(t))$. By Lemma 12, there exists $d \in L_d$ such that the trajectory-tracking model (13) has a trajectory $\zeta : [0, T] \rightarrow Z$ for which $\text{proj}_Z(\zeta_{\text{hi}}(t)) = \zeta(t)$ at t . Then, $w(p, k) = 1$ by Lemma 15. But, by (58), $k \in \pi_K(p)^C$ implies that $w(p, k) = 0$, a contradiction. ■

See Figure 9a for an illustration of Lemma 37. This lemma lets us find parameters in K that avoid points in X . So, if we can represent obstacles with points in X , we can find obstacle-avoiding trajectories, motivating the next topic.

6.3 Robot and Obstacle Geometry

Suppose X_{obs} represents one or more obstacles in X . The overall purpose of Section 6 is to find a finite set of discrete points $X_p \subset X$ to represent X_{obs} such that the trajectory parameters corresponding to X_p are a conservative approximation of those corresponding to X_{obs} , i.e. $\pi_K(X_p) \supseteq \pi_K(X_{\text{obs}}) = K_{\text{safe}}^C$. Then, as in Lemma 37, if the robot cannot collide with any of the points in X_p , it cannot collide with the obstacle X_{obs} . This is illustrated in Figure 9c. We call X_p the discretized obstacle.

The motivation behind discretizing the obstacle in this manner is that $\pi_K(X_p)$ can be implemented as a list of point constraints at runtime for the path planning optimization program in Section 7; in practice, this allows the online trajectory planner to run in real time. In the present section, we find four scalars, \bar{r} , \bar{b} , r , and a that are determined by the geometry of the robot. In the next section, we use these scalars to construct X_p . To ensure X_p can be constructed, we introduce the following assumption, which holds for obstacles represented by occupation grids, or by fitting line segments to lidar returns.

Assumption 38. *Each obstacle $X_{\text{obs},i} \subseteq X_{\text{obs}}$ is a closed polygon with a finite number of vertices and edges.*

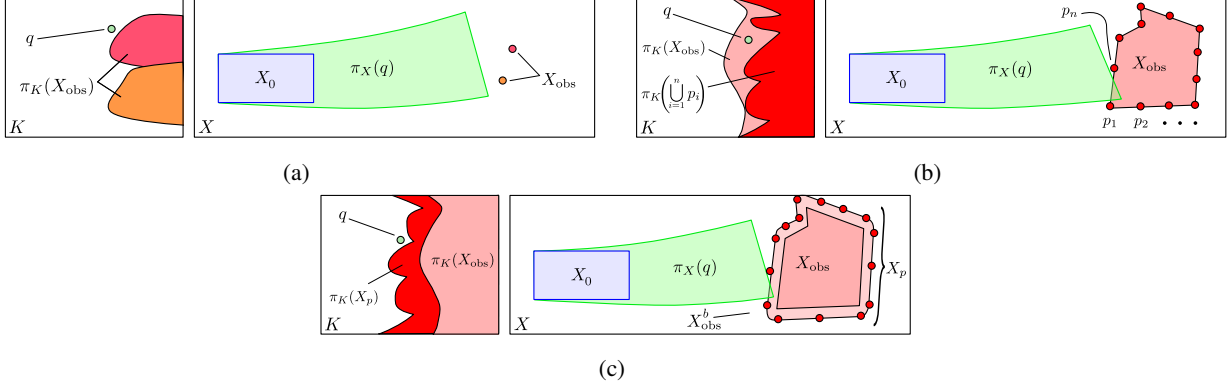


Figure 9: We illustrate the motivation and method for buffering and discretizing obstacles. In all three subfigures, the robot, with footprint X_0 , is shown at an initial condition in the xy -subspace X on the right, and the trajectory parameter space K is on the left. In Figure 9a, the obstacle X_{obs} consists of two points to illustrate the map π_K , which sends each point in X_{obs} to a subset of K (shown with matching colors) containing all trajectory parameters that could cause the robot to reach either point; since $q \in \pi_K(X_{\text{obs}})^C$, by Lemma 37, the robot cannot collide with either obstacle point. Figure 9b shows an arbitrary polygonal obstacle (as in Assumption 38) with a set of discrete points $\{p_1, \dots, p_n\}$ sampled from its boundary. These points are mapped to the parameter space K , as shown by the red area labeled $\pi_K(\bigcup_{i=1}^n p_i)$. A parameter q is chosen outside of the parameters corresponding to these points, but still lies within the projection of the actual obstacle $\pi_K(X_{\text{obs}})$, and therefore may cause a collision as illustrated by the set $\pi_X(q)$. Figure 9c shows the same obstacle, but it is buffered and the boundary of the buffered obstacle is sampled to produce the discrete, finite set X_p . The trajectory parameters corresponding to X_p are a superset of the unsafe parameters $\pi_K(X_{\text{obs}})$, so the robot cannot collide with the obstacle despite the FRS spatial projection $\pi_X(q)$ penetrating between two of the points of X_p .

Note that these polygons are not necessarily convex. If an obstacle is not a closed polygon within the sensor horizon (such as a long wall), it can be closed by intersection with the sensor horizon D_{sense} (as in Assumption 25), which can be over-approximated by a regular polygon (the intersection is a closed set by [32, Theorem 17.1]).

The remainder of Section 6.3 proceeds as follows. In Section 6.3.1, we motivate the scalars \bar{r} , \bar{b} , r , and a required to produce the discretized obstacle representation, and define several geometric objects that are used to find these scalars. In Section 6.3.2, we present a geometric expression for the robot’s dynamics. Then, in Sections 6.3.3 – 6.3.5, we find \bar{r} , \bar{b} , r , and a . To build intuition for these scalars, consider Figure 14 at the end of Section 6.3, which shows each of the scalars for rectangular and circular robot footprints.

6.3.1 Buffer and Point Spacing Motivation

Consider constructing the discretized obstacle X_p from points on the boundary of X_{obs} , as illustrated in Figure 9b. Since the high-fidelity model of the robot (1) produces continuous trajectories in the subspace X (see Assumption 1), the robot cannot collide with an obstacle without passing through the obstacle’s boundary. However, constructing X_p with a finite number of points on ∂X_{obs} may be insufficient to prevent collisions. To see why, consider the candidate $X_p = \{p_1, p_2, \dots, p_n\} \subset \partial X_{\text{obs}}$, with $n \in \mathbb{N}$. Then any $k \in \pi_K(X_p)$ may cause the robot to reach one or more $p_i \in X_p$. Suppose $q \in \pi_K(X_p)^C$. There is no guarantee that $\pi_X(q) \cap X_{\text{obs}} = \emptyset$, i.e. that q would not cause a collision with the obstacle, because the robot may be able to travel between adjacent points in X_p as shown in Figure 9b. To address this issue, we “buffer” the obstacle, then select points from its boundary with a maximum spacing allowed between the points.

Definition 39. Let $b > 0$ be a distance, called a buffer. The buffered obstacle, $X_{\text{obs}}^b \supset X_{\text{obs}}$, is a compact subset of X such that the maximum Euclidean distance between X_{obs} and X_{obs}^b is b :

$$X_{\text{obs}}^b = \left\{ p \in X \mid \exists p' \in X_{\text{obs}} \text{ for which } \|p - p'\|_2 \leq b \right\}. \quad (59)$$

Assumption 40. The space X (which is compact by Assumption 2) is large enough that $X_{\text{obs}}^b \subset X$.

Note that Assumption 27 requires a processing step before trajectory planning, a sensed obstacle $X_{\text{sense}} \subset X$ is expanded by Minkowski sum with a box to compensate for state estimation error; this produces the obstacle X_{obs}

used for trajectory planning. By Assumption 38, we require that X_{obs} is a polygon. If X_{sense} is a polygon, then the Minkowski of X_{sense} with a box (which is a polygon) returns a polygon [9], so this assumption is not violated by the construction of X_{obs} . The buffered obstacle X_{obs}^b is then defined by X_{obs} , not X_{sense} , so state estimation error is accounted for in X_{obs}^b . We then construct the discretized obstacle X_p using X_{obs}^b .

Before defining how to construct the discretized obstacle representation, we define several geometric objects, which are illustrated in Figure 10:

Definition 41. Let $I \subset \mathbb{R}^2$ be a line segment, also called an interval when it lies on either the x - or y -axis. Let $E_I = \{e_1, e_2\} \subset I$ denote the endpoints of I , such that I can be written as $I = \{e_1 + s \cdot (e_2 - e_1) \mid s \in [0, 1]\}$. The length of I is $\|e_1 - e_2\|_2$. Suppose I has a pair of distinct endpoints $\{e_1, e_2\}$, and we create the set $\ell_I = \{e_1 + s \cdot (e_2 - e_1) \mid s \in \mathbb{R}\} \subset \mathbb{R}^2$, i.e. a line that passes through e_1 and e_2 . We call ℓ_I the line defined by I .

Note that a line segment can have a length of 0 if $e_1 = e_2$. We also define a specific type of line segment called a chord:

Definition 42. Let $A \subset \mathbb{R}^2$ be a set with a boundary and $a_1, a_2 \in \partial A$. The line segment $\kappa = \{a_1 + s \cdot (a_2 - a_1) \mid s \in [0, 1]\}$ is a chord of A .

Note that κ need not be a proper subset of A , e.g., if A is not convex. Finally, we define an arc and its circle:

Definition 43. A circle $C \subset \mathbb{R}^2$ of radius $R \geq 0$ with center $p \in \mathbb{R}^2$ is the set $\{p' \in \mathbb{R}^2 \mid \|p' - p\|_2 = R\}$. An arc $A \subset \mathbb{R}^2$ is any connected, strict subset of a circle; this means that any arc has two endpoints $a, b \in \mathbb{R}^2$.

Note, that given two such endpoints and a radius, we can produce an arc A as follows: find $\theta_1 = 2 \tan^{-1} \left(\frac{a_y - p_y}{a_x - p_x + R} \right)$ and $\theta_2 = 2 \tan^{-1} \left(\frac{b_y - p_y}{b_x - p_x + R} \right)$. If $\theta_1 < \theta_2$, set $\Theta = [\theta_1, \theta_2] \subset \mathbb{R}$ or $\Theta = [\theta_2, \theta_1 + 2\pi]$ (to choose the direction of the arc), and similarly if $\theta_2 < \theta_1$. Then $A = \{q + R \cdot [\cos \theta, \sin \theta]^\top \mid \theta \in \Theta\} \subset \mathbb{R}^2$.

Next, we use line segments and arcs to understand the geometry of the buffered obstacle X_{obs}^b . Note that X_{obs}^b may contain one or more obstacles; Definition 39 and the proofs in the remainder of Section 6 still hold if X_{obs}^b is a union of polygons, which is itself a (potentially disjoint) polygon [9]. Therefore, we refer to X_{obs}^b as the singular buffered obstacle for ease of exposition. The following lemma describes the geometry of the buffered obstacle.

Lemma 44. The boundary of the buffered obstacle, consists of a finite set of line segments L and a finite set of arcs A of radius b .

More precisely, let $n_L \in \mathbb{N}$ (resp. $n_A \in \mathbb{N}$) denote the number of line segments (resp. arcs). Let $L_i \in L$ (resp. $A_i \in A$) denote the i^{th} line segment (resp. arc). Note that each L_i and A_i is a subset of X . Then the boundary of the buffered obstacle can be written as the union of all of the lines and arcs:

$$\partial X_{\text{obs}}^b = \left(\bigcup_{i=1}^{n_L} L_i \right) \cup \left(\bigcup_{i=1}^{n_A} A_i \right). \quad (60)$$

Proof. The following statements paraphrase [9, Section 9.2], which shows that the set X_{obs}^b is equivalent to the Minkowski sum of X_{obs} with a closed disk of radius b . The procedure of constructing X_{obs}^b , which we call buffering, is also called “offsetting” a polygon. Offsetting a closed and bounded polygon by a distance b produces a closed and bounded shape with a boundary consisting of line segments and circular arcs of radius b . The sets L and A are finite because X_{obs} is closed and bounded by Assumption 38. ■

Now, consider an X_p that is generated by selecting a set of points from X_{obs}^b such that the points are spaced by the distance $r > 0$ along the line segments of $\partial X_{\text{obs}}^b$ and by the distance $a > 0$ along the arcs, as illustrated in Figure 9c.

Definition 45. We call r the point spacing and a the arc point spacing.

We prove in Section 6.3.5 that, by selecting r and a as function of the buffer b , the robot cannot pass completely between any pair of points in X_p and collide with an obstacle.

Note that our use of buffering in RTD is different from typical trajectory planning methods. Trajectory planners that only consider the dynamics of the center of mass of the robot require obstacles to be buffered to compensate for the robot’s footprint and state estimation error [6, 23]. By Assumption 27, we similarly compensate for state estimation error when processing sensed obstacles to make X_{obs} . However, in RTD, the footprint is already accounted for in the set X_0 ; by buffering X_{obs} by the distance b , we make it possible to construct the discretized obstacle representation. In Appendix 14, we explore how choosing a larger buffer allows for a coarser discretization (i.e. the spacing between points of X_p can be larger) up to a provable upper bound \bar{r} (found in Section 6.3.3), while still ensuring safety.

6.3.2 Geometric Representation of the Dynamics

To understand how to relate the motion of the robot’s body to the discretized obstacle representation, we provide a geometric expression for the robot’s trajectories. Given an obstacle set X_{obs} we want to construct a discretized obstacle X_p such that the safe set of trajectory parameters corresponding to X_p contains the safe set corresponding to X_{obs} . The form of this discretized obstacle must be independent of the robot’s high-fidelity model (1), because obstacles can occur at any orientation and position relative to the robot. Therefore, we treat the robot as though it can translate and rotate arbitrarily, i.e. regardless of physics. Notice that, at any time $t \in [0, T]$, from any initial condition $\zeta_{\text{hi},0}$, and when tracking any parameter k , we can treat the robot’s body as the footprint X_0 subject to a planar translation and rotation (about the robot’s center of mass).

Definition 46. We call $\{R_t\}_{t \in [0, T]}$ a transformation family of planar translations and rotations that is continuous as a function of t .

To simplify exposition, we leave out “ $t \in [0, T]$ ” when we write $\{R_t\}$ when it is clear from context. Recall that, by Assumption 1, the robot’s high-fidelity dynamics (1) are Lipschitz continuous, hence the continuity of $\{R_t\}$ in t . Notice that, for any $\zeta_{\text{hi},0}$ and k , the corresponding $\{R_t\}$ does not have $\zeta_{\text{hi},0}$ or k as parameters in the notation. This is to lighten notation, and to emphasize that, throughout this section, we treat the robot as though it can rotate and translate arbitrarily as long as the transformation family is continuous in t .

In order to represent the robot’s dynamics, every $\{R_t\}$ must be associated with the robot’s footprint X_0 , with center of mass $c \in X_0$. To ensure that any $\{R_t\}$ is well-posed in the robot’s spatial coordinates X , and to simplify exposition, we make the following assumption.

Assumption 47. Recall that, in Definition 3, X is called the xy -subspace of the robot’s state space Z_{hi} , so $X \subset \mathbb{R}^2$. We assume that the X contains the origin.

Using Assumption 47, we define each transformation $R_t \in \{R_t\}_{t \in [0, T]}$ by a rotation angle $\theta_t \in [0, 2\pi)$ and a translation vector $s_t \in \mathbb{R}^2$, so R_t acts on a point $p \in X_0$ as

$$R_t p = \begin{bmatrix} \cos \theta_t & \sin \theta_t \\ -\sin \theta_t & \cos \theta_t \end{bmatrix} (p - c) + s_t + c. \quad (61)$$

Notice that p is rotated about the origin by θ_t after the robot’s center of mass is shifted to the origin. Each R_t can act on X_0 as:

$$R_t X_0 = \{R_t p \mid p \in X_0\}. \quad (62)$$

As an example, if $s_t = 0$, R_t rotates the robot about its center of mass c by the angle θ_t .

6.3.3 Bounding the Point Spacing

We now seek to understand how close together points must be in the discrete obstacle representation. This discussion builds on [42, Theorem 1]. To build intuition, imagine a wall in X with a gap in the wall that is large enough for the robot to pass through without touching the wall. If we keep shrinking this gap, eventually the robot is unable to pass through. In this subsection, informally, we find the largest gap that the robot cannot pass all the way through. We use the size of the gap as an upper bound \bar{r} on the spacings r and a when constructing X_p . Imagine that the buffered obstacle’s boundary is treated as the wall. If the wall is sampled so that points are closer than \bar{r} apart, this is akin to a gap of width at most \bar{r} between each pair of points.

To proceed, we first place assumptions on the shape of the robot’s footprint. We then formally define the notion of passing the robot’s footprint through a line segment. Finally, we find the size of the “largest gap” discussed above.

Assumption 48. The robot’s footprint $X_0 \subset X$ is compact and convex with nonzero volume.

Footprints such as circles and rectangles are common for ground robots (consider the Segway and Rover in Figure 2). If the robot’s footprint is not convex, it can be contained within a convex hull or rectangular bounding box [11].

To define “passing through” a line segment I , we first establish a half-plane P_I that is “defined” by I ; we use P_I as a region that the robot begins in, so that, to pass through I , the robot must leave the half-plane P_I . To create this half-plane, consider the function $\delta_{\pm} : \mathbb{R}^2 \times \mathbb{R}^2 \times \mathbb{R}^2 \rightarrow \mathbb{R}$ for which

$$\delta_{\pm}(e_1, e_2, p) = \frac{(e_{2y} - e_{1y})p_x - (e_{2x} - e_{1x})p_y - e_{2y}e_{1y} - e_{2y}e_{1x}}{\|e_2 - e_1\|_2}, \quad (63)$$

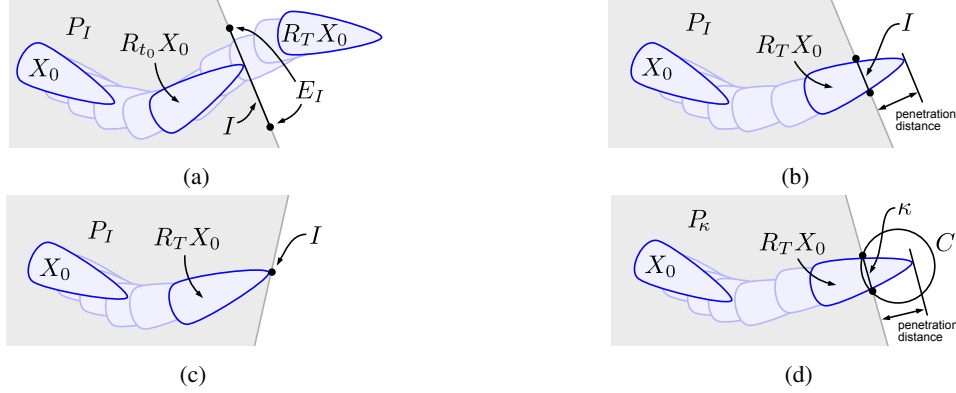


Figure 10: An illustration of passing through (as in Definition 50), penetrating (as in Definition 56), and penetrating into a circle (as in Definition 63). In each subfigure, a family $\{R_t\}_{t \in [0, T]}$ of continuous rotations and translations attempts to pass the convex, compact set X_0 through the line segment I with endpoints E_I . At $t = 0$, X_0 lies in the half-plane P_I , defined by I as in Definition 49. Each figure contains X_0 at its initial position $R_0 X_0$ and final position $R_T X_0$ indicated by a dark blue outline. The lighter outlines between these positions show examples of X_0 being translated and rotated as $\{R_t\}$ is applied. In Figure 10a, X_0 is able to pass fully through I ; the index $t_0 \in [0, T]$ where X_0 first touches I is also shown with a dark blue outline. In Figure 10b, X_0 is unable to pass fully through I , but penetrates through I by some distance into P_I^C . In Figure 10c, the line segment I has length 0, so X_0 cannot pass through it, but instead stops as soon as it touches I , and achieves 0 penetration distance through I . Note that, in this case, P_I is defined by a line perpendicular to the line segment from I to the center of mass of X_0 , as per Definition 49. In Figure 10d, the circle C has a chord κ , and X_0 penetrates into C through κ by the penetration distance shown. The half-plane defined by κ is denoted P_κ .

where the subscript x or y denotes the corresponding coordinate of a point in \mathbb{R}^2 . If I has distinct endpoints $\{e_1, e_2\}$, then $\delta_\pm(e_1, e_2, p)$ is the perpendicular distance from the point p to the line defined by I . The sign of $\delta_\pm(e_1, e_2, p)$ is positive if p lies to the “left” of the line defined by I , relative to the “forward” direction from e_1 to e_2 . The function δ_\pm is illustrated in Figure 11a. We use δ_\pm to define a half-plane in \mathbb{R}^2 as follows:

Definition 49. Let $c \in X_0$ denote the center of mass $[x_{c,0}, y_{c,0}]^\top$ of the robot’s footprint at time 0, as in Assumption 4. Let I be a line segment as in Definition 41 with two distinct endpoints $E_I = \{e_1, e_2\}$. Then $P_I \subset \mathbb{R}^2$ denotes the closed half-plane defined by I ; this half-plane is determined by the line defined by I and by c as:

$$P_I = \{p \in X \mid \text{sign}(\delta_\pm(e_1, e_2, p)) = \text{sign}(\delta_\pm(e_1, e_2, c))\}, \quad (64)$$

where $\text{sign}(a) = 1$ for $a \geq 0$ and -1 otherwise. Now suppose that I is a line segment of length 0, i.e. $e_1 = e_2$, so we cannot directly define P_I as in (64). Suppose that $e_1 \neq c$. So, we can pick a point e' for which $(e' - e_1) \cdot (c - e_1) = 0$ where \cdot denotes the standard inner product on \mathbb{R}^2 , so the line segment from e_1 to c is perpendicular to the line segment from e_1 to e' . Then, P_I is given by (64), but using e' in place of e_2 .

In the case where $e_1 = e_2 = c$, P_I is undefined. See Figures 10 and 11a for illustrations of the different cases of P_I . Notice that, except when $e_1 = e_2 = c$, P_I is always a closed half-plane, even if c lies on the line defined by I . The utility of P_I is that, if the line defined by I does not intersect X_0 , then $X_0 \subset P_I$, i.e. P_I contains X_0 . So, we can use P_I as a region that the robot starts in at time 0.

Definition 50. Let $I \subset X \setminus X_0$ be a line segment with endpoints E_I as in Definition 41, and P_I be the half-plane defined by I as in Definition 49. Suppose that the robot lies fully within P_I at time 0, i.e. $X_0 \subset \text{int}(P_I)$. Let $\{R_t\}$ be a transformation family as in Definition 46. Let t_0, t_1 be indices in $(0, T]$ such that $R_t X_0$ intersects the “middle” of I , i.e. $R_t X_0 \cap (I \setminus E_I) \neq \emptyset$, for all $t \in [t_0, t_1]$. Furthermore, suppose that $R_t X_0 \subset P_I$ for all $t \in [0, t_0)$, and that no $R_t X_0$ can intersect the endpoints E_I (i.e. $R_t X_0 \cap E_I = \emptyset$) except at $t = T$. We say that such a transformation family attempts to pass X_0 through I . If X_0 is able to leave P_I while passing through I , i.e. $R_T X_0 \subset P_I^C$, then X_0 is said to pass fully through I .

See Figure 10 for an illustration of passing through and passing fully through. Note, in Definition 50 and throughout the remainder of the section, we abuse vocabulary by saying the transformation family attempts to pass X_0 through I . This choice of words seems to conflate the robot’s footprint at time 0 with the motion of the footprint through space.

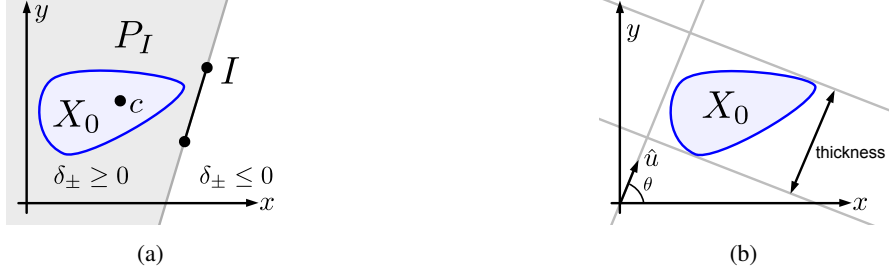


Figure 11: An arbitrary, compact, convex set X_0 lies in the plane. In Figure 11a, the line segment I defines the closed half-plane P_I (the grey area) using the function δ_{\pm} from (63). If the endpoints of I are labeled e_1 and e_2 , then the set P_I contains all points $p \in \mathbb{R}^2$ for which the sign of $\delta_{\pm}(e_1, e_2, p)$ is the same as the sign of $\delta_{\pm}(e_1, e_2, c)$, where c is the center of mass of X_0 . In Figure 11b, a unit vector \hat{u} is fixed to the origin with angle θ . The thickness of X_0 is given by the distance between the two unique lines that are tangent to X_0 and perpendicular to \hat{u} .

In particular, the position of the set X_0 is fixed at time 0; instead, the motion of the robot at each t is represented by each set $R_t X_0$.

Notice that, since X_0 must pass through the interior of I , it is not allowed to go “around” I when passing through. Furthermore, over the time horizon $[t_0, t_1]$ in Definition 50, the set made by the intersection $R_t X_0 \cap I$ is a chord (as in Definition 42) of $R_t X_0$ [42, Theorem 1]. We now state a property of X_0 used to bound the size of the aforementioned “gap in a wall” in Lemma 52 below.

Definition 51. Given a unit vector in \mathbb{R}^2 at an angle θ , the thickness of X_0 along this unit vector is the distance between the two unique lines that are tangent to X_0 and perpendicular to the vector. The width of X_0 is defined as the minimum thickness of X_0 when searching over all $\theta \in [0, 2\pi)$, and the diameter of X_0 is, similarly, the maximum thickness [42, Section 1].

See Figure 11b for an illustration of thickness. Note that the width is nonzero and finite because X_0 is compact and has nonzero volume by Assumption 48.

Lemma 52. [42, Theorem 1] Let $I \subset (X \setminus X_0)$ be a line segment with endpoints E_I and length $L > 0$ (as in Definition 41). Let X_0 be the robot’s footprint at time 0 (as in Definition 3), with width $W > 0$ (as in Definition 51). Then X_0 can pass through I (as in Definition 50) if and only if $W < L$.

Proof. See [42] for a more detailed proof. We only sketch out the intuition here. Recall that X_0 is convex and compact with nonzero volume by Assumption 48.

Suppose a transformation family $\{R_t\}$ passes X_0 through I as in Definition 50. Then there exists an interval of time $[t_0, t_1] \subset (0, T)$ for which $R_t X_0 \cap (I \setminus E_I)$ is nonempty for all $t \in [t_0, t_1]$; note that $t_1 > t_0$ because X_0 has nonzero volume. The set $R_t X_0 \cap (I \setminus E_I)$ is a chord (as in Definition 42) of $R_t X_0$ with length greater than or equal to the width W as in Definition 51. Since X_0 can pass fully through I , the endpoints E_I never intersect any $R_t X_0$. Therefore the length of the chord $R_t X_0 \cap I$ is always less than L , so $L > W$.

Now suppose $W < L$. If X_0 has diameter D , then X_0 can fit completely inside a rectangle with short side length W and long side length D [11, Theorem 3]. This rectangle can be rotated so that its short side is parallel to I , then pass fully through I by pure translation, i.e. with no further rotations. Since X_0 fits inside the rectangle, X_0 can pass fully through I . ■

Finally, we consider these geometric definitions as applied to the robot:

Definition 53. The scalar \bar{r} denotes the maximum point spacing, which is equal to the width of the robot footprint X_0 as in Definition 51.

The maximum point spacing relates to the points in the discretized obstacle X_p as follows. As illustrated in Figure 9c, the discretized obstacle X_p is constructed by first buffering an obstacle X_{obs} by a distance b (see Definition 39), then sampling the boundary of X_{obs}^b such that the distance between consecutive sampled points is strictly less than \bar{r} .

Definition 54. We refer to consecutive sampled points as adjacent points of the discretized obstacle X_p .

We address the notion of adjacent points in more detail in Section 6.4.1. Suppose that we attempt to pass X_0 through the gap between two adjacent points of X_p , and do not allow X_0 to overlap with either of the points while passing through. Since each pair of adjacent points of X_p are strictly closer than \bar{r} to each other, we know by Lemma 52 that the robot can never pass fully through the gap. Consequently, finding \bar{r} correctly is critical, leading to the following remark:

Remark 55. *The width \bar{r} of X_0 must either be found exactly or underapproximated to ensure safety. If the width is overapproximated, then the robot described by X_0 may be able to pass between a pair of points spaced slightly less than \bar{r} apart, as per Lemma 52. Methods exist to exactly compute the width of arbitrary compact convex sets. For example, the algorithm in [11] finds the smallest bounding rectangle of the set; then the length of the rectangle’s shorter leg is the set’s width. A geometric procedure to find the width using the rotation angle θ and the thickness (as in Definition 51) is presented in [42, Section 1].*

6.3.4 Bounding the Buffer Size

As in Section 6.3.3, imagine a wall with gap of width \bar{r} . Lemma 52 proves that the robot cannot pass fully through this gap. However, the robot can still penetrate through the gap by some distance before it gets stopped by the wall. In this section, we find the farthest distance that the robot can penetrate through the gap. We use this supremizing penetration distance as an upper bound \bar{b} on the obstacle buffer, so $b \in (0, \bar{b})$. Recall that our intention is to discretely sample the boundary of the buffered obstacle in (59) to produce a set X_p , so the spacing between adjacent points of X_p (as in Definition 54) must be smaller than \bar{r} . If the robot is not allowed to touch any points in X_p , it cannot penetrate farther than the distance \bar{b} between any pair of adjacent points. So, obstacles do not need to be buffered by a distance larger than \bar{b} . The existence of \bar{b} is proven in Lemma 57. To proceed further, we define the word “penetrate” precisely.

Definition 56. *Let $I \subset (X \setminus X_0)$ be a line segment as in Definition 41. Let P_I be the half-plane defined by I as in Definition 49, and suppose $X_0 \subset P_I$ strictly. Let $\{R_t\}$ be a transformation family that attempts to pass X_0 through I by Definition 50. Suppose X_0 cannot pass fully through I , and that $R_T X_0 \cap P_I^C$ is nonempty, so there is some portion of X_0 that does pass through I . Consider all line segments perpendicular to I with one endpoint on I and the other at a point in $R_T X_0$ in P_I^C . We call the maximum length of any of these line segments the penetration distance of X_0 through I . The set $R_T X_0$ penetrates I by this distance, as in Figure 10b. If I is of length 0, then the penetration distance of X_0 through I is always 0, as in Figure 10c.*

Lemma 57. *Let X_0 be the robot’s footprint at time 0 (as in Definition 3), with width \bar{r} (as in Definition 53). Let $I_{\bar{r}} \subset (X \setminus X_0)$ be a line segment of length \bar{r} (as in Definition 41). Then there exists a supremizing penetration distance \bar{b} (as in Definition 56) that can be achieved by passing X_0 through $I_{\bar{r}}$ (as in Definition 50).*

Proof. This proof is illustrated in Figure 12. We sketch the intuition first. To find \bar{b} , we use transformation families $\{R_t\}$ to pass X_0 through $I_{\bar{r}}$. Recall that X_0 cannot pass fully through $I_{\bar{r}}$ by Lemma 52. Then, we measure the penetration distance corresponding to each transformation family, until we find a maximum.

Now we proceed rigorously. Note that X_0 is compact and convex with nonzero volume as in Assumption 48. Recall by Assumption 47 that the xy -subspace $X \subset \mathbb{R}^2$ contains the origin of \mathbb{R}^2 . To ease the exposition, suppose without loss of generality that X_0 lies entirely in the intersection of X with the left half-plane of \mathbb{R}^2 , and that $I_{\bar{r}}$ is fixed to the origin and oriented vertically in the upper half-plane, so $I_{\bar{r}} = \{0\} \times [0, \bar{r}]$. In this case, the half-plane $P_{I_{\bar{r}}}$ defined by $I_{\bar{r}}$ (as in Definition 49) is the closed left half-plane. This can be done without loss of generality because, when passing X_0 through $I_{\bar{r}}$ with a transformation family $\{R_t\}$ (as in Definition 46), we only care about the relative position of X_0 to $I_{\bar{r}}$ at each $t \in [0, T]$. If X_0 and $I_{\bar{r}}$ are oriented arbitrarily in X , we can first rotate and translate both X_0 and $I_{\bar{r}}$ with the same transformation to move the “lower” endpoint of $I_{\bar{r}}$ to the origin, then pass X_0 through $I_{\bar{r}}$, and finally undo the first rotation and translation to return X_0 and $I_{\bar{r}}$ to their original positions.

Let $\mathcal{R}_{\bar{r}}$ denote the set of all transformation families $\{R_t\}$ that attempt to pass X_0 through $I_{\bar{r}}$ as per Definition 50. By Lemma 52, X_0 cannot pass fully through $I_{\bar{r}}$ because $I_{\bar{r}}$ is of length \bar{r} . By Definition 56, X_0 may penetrate $I_{\bar{r}}$ by some distance, which depends upon the transformation family $\{R_t\}$. We must show that, across all $\{R_t\} \in \mathcal{R}_{\bar{r}}$, there is a supremizing penetration distance.

Consider an arbitrary $\{R_t\} \in \mathcal{R}_{\bar{r}}$. Since $I_{\bar{r}}$ is collinear with the y -axis, we can find the penetration distance of X_0 through $I_{\bar{r}}$ corresponding to $\{R_t\}$ using the function $\delta_x : \mathcal{P}(\mathbb{R}^2) \rightarrow \mathbb{R}$, which returns the right-most point of a set $A \subset \mathbb{R}^2$:

$$\delta_x(A) = \sup_a \{a_x \mid a \in A\}, \quad (65)$$



Figure 12: An arbitrary compact, convex set X_0 of width \bar{r} penetrates a line segment $I_{\bar{r}}$ when a transformation family $\{R_t\}_{t \in [0, T]}$ is applied to pass X_0 through $I_{\bar{r}}$ as in Definition 50. Since $I_{\bar{r}}$ is of length \bar{r} , X_0 cannot pass fully through by Lemma 52. At the initial index $t=0$ and the final index $t=T$, the sets $R_0 X_0$ and $R_T X_0$ are shown with dark blue outlines. A sampling of intermediate indices $t \in (0, T)$ are shown with light blue outlines. In Figure 12a, X_0 penetrates through $I_{\bar{r}}$ by the distance $\delta_x(R_T X_0)$; this produces a suboptimal, feasible value to (66). Figure 12b shows the optimal value of the program, which returns the supremizing penetration distance of C through $I_{\bar{r}}$.

where a_x is the x -component of the point a . So, given a particular $\{R_t\} \in \mathcal{R}_{\bar{r}}$, $\delta_x(R_T X_0)$ is the penetration distance of X_0 through $I_{\bar{r}}$ by Definition 56. Recall that X_0 is compact (i.e. closed and bounded in X) and that X_0 cannot pass fully through $I_{\bar{r}}$ by Lemma 52 (i.e. the horizontal displacement achieved by $R_T X_0$ is bounded). Therefore, $\delta_x(R_T X_0)$ is upper bounded.

We have shown that the penetration distance is bounded for each family $\{R_t\} \in \mathcal{R}_{\bar{r}}$. To prove the claim that there is a supremizing penetration distance, we must show that the value of δ_x is upper bounded across all $\{R_t\} \in \mathcal{R}_{\bar{r}}$. In other words, we want to know that the following supremum is finite:

$$\bar{b} = \sup_{\{R_t\}} \delta_x(R_T X_0) \quad (66)$$

$$\text{s.t. } \{R_t\} \in \mathcal{R}_{\bar{r}}. \quad (67)$$

Recall from Definition 51 that X_0 has a finite diameter D , which is the largest possible distance between two parallel lines that are tangent to X_0 . So, for any $\{R_t\} \in \mathcal{R}_{\bar{r}}$, if $\delta_x(R_T X_0) > D$, then X_0 has passed fully through I . But this is impossible by Lemma 52. Since $\bar{b} \leq D$, (66) is upper bounded. ■

We now relate Lemma 57 to the robot.

Definition 58. Let X_0 be a robot footprint as in Assumption 48, with width \bar{r} as in Definition 51. Suppose \bar{b} is the optimum value of (66), which exists by Lemma 57. We call \bar{b} the supremizing penetration distance.

Remark 59. In addition to using \bar{b} to define the maximum buffering required to ensure safety during planning, we use \bar{b} to find the point spacing r (see Lemma 62) and arc point space a (see Lemma 64) which define exactly how to discretize the obstacle. In particular, given $b \in (0, \bar{b})$ we show how to select r and a using optimization problems (69) and (72). Then, we buffer the obstacle by b and sample its boundary using r and a in Algorithm 1 to construct the discretized obstacle X_p . In Theorem 68, we prove that the robot can never penetrate through X_p farther than b , i.e. the robot cannot collide with X_{obs} , because of the use of r and a . Importantly, for the optimization problems that define r and a to be well-posed, we must ensure that b is in fact less than the supremizing penetration distance. As a result, underapproximating \bar{b} is critical. A geometric method for finding \bar{b} for an arbitrary convex robot footprint is presented in Lemma 74 in Appendix 13.

6.3.5 Finding the Point Spacing and Arc Point Spacing

Let \bar{r} be as in Definition 53 and \bar{b} as in Definition 58. We now choose $b \in (0, \bar{b})$, then use b to find the point spacing r and the arc point spacing a , from Definition 45. First, we prove two lemmas about chords (see Definition 42) in order to find r and a . Then, for $b \in (0, \bar{b})$, we find $r \in (0, \bar{r})$ with Lemma 62 and $a \in (0, \bar{r})$ with Lemma 64.

Lemma 60. Given any three distinct, parallel chords of a convex, compact set in \mathbb{R}^2 , we claim that the middle chord is not the shortest of the three. We now restate this mathematically. Let $C \subset \mathbb{R}^2$ be a convex, compact set with nonzero volume. Let κ_1 , κ_2 , and κ_3 be three chords of C (as in Definition 42) such that $\kappa_1 \parallel \kappa_2 \parallel \kappa_3$ and $\kappa_i \cap \kappa_j = \emptyset$ for any $i \neq j$. Suppose the chords have lengths L_1 , L_2 , and L_3 , respectively. Furthermore, assume that there exists at least one line segment (as in Definition 41) within C that intersects κ_2 , and that has one endpoint on κ_1 and the other endpoint on κ_3 ; in other words, κ_2 lies between κ_1 and κ_3 . Then $L_1 \geq L_3$ implies that $L_2 \geq L_3$ and $L_1 > L_3$ implies that $L_2 > L_3$.

Proof. Let $e_{i,1}$ and $e_{i,2}$ denote the endpoints (as in Definition 42) of each chord κ_i where $i = 1, 2, 3$. By definition, these endpoints lie in ∂C . Without loss of generality, assume that all three chords are oriented vertically (rotating the chords and the shape C does not change the relative position of the chords to each other or to C). Also suppose without loss of generality that each $e_{i,1}$ is the “upper” endpoint (we can do this without loss of generality because each chord is a line segment by Definition 42, and because we can swap the labels of the endpoints of a line segment without changing the set of points in the line segment). Define the line segments I_1 from $e_{1,1}$ to $e_{3,1}$ and I_2 from $e_{1,2}$ to $e_{3,2}$. Since C is convex, $I_1, I_2 \subset C$.

Suppose κ_1 and κ_3 have the same length, so $L_1 = L_3$. Then the quadrilateral with edges given by the line segments $\kappa_1, I_1, \kappa_3,$ and I_3 is a parallelogram Q_P (two of its sides are parallel and of equal length). So, every line segment inside Q_P that is parallel to κ_1 has length $L_1 = L_3$. Furthermore, Q_P lies completely inside C because C is convex; this means that $\kappa_2 \cap Q_P$ is a chord of Q_P that is parallel to κ_1 , and $\kappa_2 \cap Q_P \subseteq \kappa_2$. Then, since the length of $\kappa_2 \cap Q_P = L_1$, the length of κ_2 is $L_2 \geq L_1 \geq L_3$.

Now suppose $L_1 > L_3$. Then the quadrilateral with edges $\kappa_1, I_1, \kappa_3,$ and I_3 is a trapezoid Q_T (two of its sides are parallel and of different lengths) that lies within C . Since $L_1 > L_3$, every line segment inside Q_T that is parallel to κ_1 is strictly shorter than κ_1 . So, similar to the logic for Q_P above, the length of $\kappa_2 \cap Q_T$ is greater than L_3 , meaning that $L_2 > L_3$. ■

Next, we use Lemma 60 to understand the shape of the footprint as it passes through a line segment in Lemma 61. In particular, Lemma 61 shows that, as the robot penetrates farther through a line segment, the size of the intersection between the robot and the line segment increases. We use this result in Lemma 62 to bound r above and below.

Lemma 61. *Let X_0 be the robot’s footprint at time 0 (as in Definition 3), with width \bar{r} (as in Definition 53). Let $I_{\bar{r}} \subset (X \setminus X_0)$ be a line segment (as in Definition 41) of length \bar{r} . Let $P_{I_{\bar{r}}}$ be the closed half-plane defined by $I_{\bar{r}}$ (as in Definition 49) and containing X_0 , and suppose that $X_0 \subset P_{I_{\bar{r}}}$. Suppose the transformation family $\{R_t\}$ attempts to pass X_0 through $I_{\bar{r}}$ (as in Definition 50). Suppose $t_0 > 0$ such that, for each $t \in [t_0, T]$, the set $\kappa_t := R_t X_0 \cap I_{\bar{r}}$ is nonempty and is a chord of $R_t X_0$. Then, for any $t > t_0$, every chord of $R_t X_0$ that is parallel to $I_{\bar{r}}$ and lies in $P_{I_{\bar{r}}}^C$ is shorter than κ_t .*

Proof. This proof follows directly from Definition 50 of passing through and from Lemma 60. Recall that X_0 is convex and compact with nonzero volume as in Assumption 48.

As in Lemma 57, without loss of generality assume $I_{\bar{r}}$ lies along the y -axis with its lower endpoint fixed to the origin, i.e. $I_{\bar{r}} = \{0\} \times [0, \bar{r}]$, and that X_0 lies in the closed left half-plane, which is $P_{I_{\bar{r}}}$. We can do this without loss of generality because X contains the origin by Assumption 47, so moving X_0 and $I_{\bar{r}}$ in this way is a translation and rotation that can be undone.

Let $t \in (t_0, T]$ be arbitrary and let κ_t denote the chord $R_t X_0 \cap I_{\bar{r}}$. Note that t_0 exists by Definition 50. In addition, for any $t \in (t_0, T]$, the set $R_t X_0 \cap I_{\bar{r}}$ is a chord of $R_t X_0$ [42, Theorem 1]. Notice that the length of κ_t is less than or equal to \bar{r} by Definition 50 of passing through. By Lemma 52, X_0 cannot pass fully through $I_{\bar{r}}$. Therefore, there exists a chord κ^- of $R_t X_0$ that lies in $P_{I_{\bar{r}}}$, is parallel to $I_{\bar{r}}$, and has length greater than or equal to \bar{r} . Otherwise, $R_t X_0$ could pass fully through $I_{\bar{r}}$ by translation. Since $t > t_0$, $R_t X_0 \cap P_{I_{\bar{r}}}^C$ is nonempty by Definition 50 of passing through. Therefore, there exist chords of $R_t X_0$ that lie in $P_{I_{\bar{r}}}^C$ and are parallel to $I_{\bar{r}}$. Let κ^+ be any such chord. The chords $\kappa^-, \kappa_t,$ and κ^+ are three parallel, distinct chords of the convex, compact set $R_t X_0$, and the length of κ^- is greater than the length of κ_t . Therefore, by Lemma 60, κ^+ is shorter than κ_t . Since κ^+ was arbitrary, we are done. ■

Now we find the point spacing r with a procedure illustrated in Figure 13.

Lemma 62. *Let $X_0 \subset \mathbb{R}^2$ be the robot’s footprint at time 0 (as in Definition 3), with width \bar{r} (as in Definition 53). Let \bar{b} be the maximum penetration depth corresponding to X_0 (as in Definition 58). Pick $b \in (0, \bar{b})$. Then there exists $r \in (0, \bar{r}]$ such that, if I_r is a line segment of length r (as in Definition 41), and if $\{R_t\}$ is any transformation family that attempts to pass X_0 through I_r (as in Definition 50), then the penetration distance of X_0 through I_r (as in Definition 56) is less than or equal to b .*

Proof. We first sketch the intuition for the proof. As in Lemma 57, we attempt to pass X_0 through a line segment $I_{\bar{r}}$ of length \bar{r} , but X_0 cannot pass fully through $I_{\bar{r}}$ by Lemma 52. Each time we pass X_0 through $I_{\bar{r}}$, we halt passing it through when the penetration distance of X_0 through $I_{\bar{r}}$ is equal to b . Then, we measure the length of the line segment $X_0 \cap I_{\bar{r}}$. The length of the smallest such line segment is the desired point spacing r .

We now proceed rigorously. Let $I_{\bar{r}} \subset (X \setminus X_0)$ be a line segment of length \bar{r} (as in Definition 41). Without loss of generality, suppose that $I_{\bar{r}}$ is vertical with its lower endpoint at the origin, so $I_{\bar{r}} = \{0\} \times [0, \bar{r}]$; and suppose that

$X_0 \subset X \subset \mathbb{R}^2$ lies entirely in the closed left half-plane. See the proof of Lemma 57 for why $I_{\bar{r}}$ and X_0 can be placed this way without loss of generality; in brief, the rotations and translations required can be undone.

Next, we discuss how we measure horizontal distance (to constrain the penetration distance to b) and vertical span (to find the distance r). Unlike in Lemma 57, instead of letting X_0 penetrate through $I_{\bar{r}}$ by the distance \bar{b} , we limit the penetration distance to $b < \bar{b}$. Since $I_{\bar{r}}$ is oriented vertically at the origin, we can measure the penetration distance through $I_{\bar{r}}$ using the horizontal distance given by δ_x from (65), which returns the maximum x -coordinate over all points in a set in \mathbb{R}^2 . To measure vertical span, we define the map $\delta_y : \mathcal{P}(\mathbb{R}^2) \rightarrow \mathbb{R}_{\geq 0}$ as follows:

$$\delta_y(A) = \sup\{a_y \mid a \in A\} - \inf\{a_y \mid a \in A\}, \quad (68)$$

where a_y denotes the y -component of a .

Now, we find r by constructing the line segment I_r . Let $\mathcal{R}_{\bar{r}}$ be the set of all transformation families $\{R_t\}$ (as in Definition 46) that attempt to pass X_0 through $I_{\bar{r}}$ (as in Definition 50). Suppose that $\{R_t\} \in \mathcal{R}_{\bar{r}}$ is a transformation family for which, at $t = T$, the penetration distance of X_0 through $I_{\bar{r}}$ is b (as in Definition 56). In other words, $\delta_x(R_T X_0) = b$. Consider the line segment $I_r = R_T X_0 \cap I_{\bar{r}}$ (this is a line segment by [42, Theorem 1]). Then, under the transformation family $\{R_t\}$, X_0 penetrates through I_r by the distance b , and the length of I_r is given by $\delta_y(R_T X_0 \cap I_{\bar{r}})$. So, our goal is to find the shortest I_r over all such $\{R_t\}$; the length of the shortest I_r is the distance r claimed by the premises. Consider the following program to achieve this goal:

$$r = \inf_{\{R_t\}} \delta_y(R_T X_0 \cap I_{\bar{r}}) \quad (69)$$

$$\text{s.t. } \{R_t\} \in \mathcal{R}_{\bar{r}}, \quad (70)$$

$$\delta_x(R_T X_0) = b. \quad (71)$$

We first check that feasible solutions exist for (69). By Lemma 57 and Remark 59, there exist $\{R_t\} \in \mathcal{R}_{\bar{r}}$ for which $\delta_x(R_T X_0) = \bar{b} > b$. For any such $\{R_t\}$, since $R_0 X_0 = X_0$ (which lies in the left half-plane), we have that $\delta_x(R_0 X_0) \leq 0$. Then, since $\{R_t\}$ is continuous by Definition 46, there must exist some $\tau \in (0, T)$ for which $\delta_x(R_\tau X_0) = b$. So, again using that $\{R_t\}$ is continuous, we can “cut off” the time index t at τ and then rescale time so that τ becomes T as follows. For $t \in [0, \tau]$, let $t' = \frac{T}{\tau}t$. Then the family $\{R_{t'}\}_{t' \in [0, T]}$ for which $R_{t'} = R_t$ is a family in $\mathcal{R}_{\bar{r}}$ for which X_0 penetrates through $I_{\bar{r}}$ by the distance b .

Now we check that $r \in (0, \bar{r})$. Suppose that $\{R_t\}$ is a feasible solution to (69). Notice that $\{R_t\}$ cannot pass X_0 fully through $I_{\bar{r}}$ by Lemma 52, so $\delta_y(R_T X_0 \cap I_{\bar{r}}) \leq \bar{r}$ is immediate. By Definition 50 of passing through, $R_T X_0 \cap I_{\bar{r}}$ must be nonempty, so $r = \delta_y(R_T X_0 \cap I_{\bar{r}}) \geq 0$.

Finally, we show that (69) achieves a minimum $r > 0$. Let $\{R_t\}$ be a feasible solution. Suppose for the sake of contradiction that there is no $\varepsilon > 0$ for which $r \geq \varepsilon$. Let $\kappa_r = R_T X_0 \cap I_{\bar{r}}$, which is a chord (as in Definition 42) of $R_T X_0$ [42, Theorem 1]. By Lemma 61, no chord parallel and to the right of κ_r can be longer than κ_r , because $I_{\bar{r}}$ is of length $\bar{r} \geq r$ and parallel to κ_r . But then, if $\varepsilon = 0$, since X_0 has nonzero volume by Assumption 48, there can be no nonempty chords to the right of κ_r , which contradicts the fact that $\{R_t\}$ attempts to pass X_0 through I and as a result violates (71). ■

A suboptimal, feasible solution to (69) is shown in Figure 13a; an optimal solution for the same X_0 is shown in Figure 13b. With Lemma 62, and specifically (69), we find the point spacing r as in Definition 45. We use r as follows. Suppose our robot has a footprint X_0 as in Definition 3, with width \bar{r} as in Definition 53, and associated supremizing penetration distance \bar{b} as in Definition 58. Pick $b \in (0, \bar{b})$. Suppose $X_{\text{obs}} \subset X$ is an obstacle as in Definition 24, and let it consist of polygons as in Assumption 38. Construct X_{obs}^b , the buffered obstacle, with (59). Recall by Lemma 44 that the boundary of the buffered obstacle consists of line segments and arcs. Then, r lets us construct the portion of the discretized obstacle X_p that corresponds to the line segments in $\partial X_{\text{obs}}^b$. In particular, suppose we sample each line segment of $\partial X_{\text{obs}}^b$ such that adjacent points (as in Definition 54) are no farther than r apart. Then, by Lemma 62, if I_r is a line segment between two of these adjacent points, the robot can penetrate no further than b through I_r (as in Definition 56). In other words, the robot cannot reach X_{obs} by going “between” the adjacent points of the line segments.

Now, note that we cannot necessarily use r as the point spacing distance when sampling the arcs of $\partial X_{\text{obs}}^b$. To understand why, informally, imagine X_0 penetrating into a circle C of radius $b \in (0, \bar{b})$ instead of a line segment of length \bar{r} as in Lemma 62. Suppose that X_0 stops when it touches the center of the circle. For the sake of argument, suppose that the boundary ∂X_0 (which exists because X_0 is compact by Assumption 48) intersects C in exactly two

points; then, in the intersection of X_0 with C , there is an arc of radius b between these two points. If the length of this arc were equal to r , for an arbitrary convex X_0 , then we could sample “along” each arc by the distance r . But this is not true in general; one can check that it is false if X_0 is circular, as in Example 67. Therefore, we need a different point spacing for the arcs, which is the arc point spacing a as in Definition 45.

Before finding a , we generalize the concepts of passing through and penetrating from line segments to circles and arcs:

Definition 63. Let $C \subset \mathbb{R}^2$ be a circle of radius R with center p as in Definition 43. Let X_0 be the robot’s footprint at time 0 as in Definition 3. Let κ be a chord of C as in Definition 42. Then passing X_0 into C through κ is defined as passing X_0 through the chord κ as in Definition 50. If the length of κ is less than the width of X_0 , then, by Lemma 52, X_0 cannot pass fully through κ , but does penetrate the chord up to some distance as in Definition 56. Let P_κ be the closed half-plane defined by κ as in Definition 49. The penetration of X_0 into C through κ is the maximum Euclidean distance from any point in $X_0 \cap C$ to a point in $X_0 \cap P_\kappa^C$.

This definition is illustrated in Figure 10d.

Lemma 64. Let X_0 be the robot’s footprint at time 0 (as in Definition 3), with width \bar{r} (as in Definition 53). Let \bar{b} be the supremizing penetration distance corresponding to X_0 (as in Definition 58). Pick $b \in (0, \bar{b})$, and let $C \subset (X \setminus X_0)$ be a circle of radius b centered at a point $p \in X$ (as in Definition 43). Then there exists a number $a \in (0, \bar{r})$ such that, if κ_a is any chord of C of length a (as in Definition 42), then the penetration of X_0 into C through κ (as in Definition 63) is no larger than b .

Proof. We begin with a sketch of the proof to build intuition. This proof proceeds much as for Lemma 62 to find the point spacing r . To prove that a exists, we pass X_0 through a line segment $I_{\bar{r}}$ of length \bar{r} , up to a penetration distance of b . Then, we translate the circle C of radius b such that X_0 is penetrating into this circle. From the intersection of the circle with X_0 , we find a chord κ_a . The length of κ_a depends on the transformation family $\{R_t\}$ used to pass X_0 through $I_{\bar{r}}$. We search across all such transformation families to find the smallest κ_a , the length of which is the desired arc point spacing a .

Now we proceed rigorously. Recall by Assumption 48 that X_0 is compact, convex, and has nonzero volume, and by Assumption 47 that $X \subset \mathbb{R}^2$ contains the origin of \mathbb{R}^2 . Let $I_{\bar{r}} \subset (X \setminus X_0)$ be a line segment of length \bar{r} (as in Definition 41). As in Lemma 57 (used to find \bar{b}), suppose without loss of generality that $I_{\bar{r}}$ is oriented vertically, with its lower endpoint fixed at the origin, so $I_{\bar{r}} = \{0\} \times [0, \bar{r}]$. Suppose without loss of generality that X_0 lies fully in the left half-plane, which is $P_{I_{\bar{r}}}$, the half-plane defined by $I_{\bar{r}}$ (as in Definition 49). This can be done without loss of generality because it only requires rotation and translation of X_0 and $I_{\bar{r}}$, which can be undone.

Let $\mathcal{R}_{\bar{r}}$ be the set of all transformation families that attempt to pass X_0 through $I_{\bar{r}}$ (as in Definition 50). By Lemma 62, there exist $\{R_t\} \in \mathcal{R}_{\bar{r}}$ for which the penetration distance of X_0 through $I_{\bar{r}}$ is equal to b . Such $\{R_t\}$ are feasible solutions to (69). Let $\ell_b = \{b\} \times \mathbb{R}$ be the vertical line at $x = b$. Let $\{R_t\}$ be a feasible solution to (69). Then, there exists at least one point in $R_T X_0$ that lies on ℓ_b . Let κ_b denote the set $R_T X_0 \cap \ell_b$, which is a chord of $R_T X_0$ [42, Theorem 1]. Note that κ_b may have length 0, i.e. it is a point, and that κ_b is compact, because it is the intersection of two compact sets [32, Theorem 17.1 and Theorem 26.2]. Place the circle C (with radius b) tangent to the y -axis, and centered at any point $p_b \in \kappa_b$. Let C_b denote this translation of C . Recall the function δ_x from (65), which returns the right-most point of a set in \mathbb{R}^2 . With these objects, we pose following program to find the shortest chord κ_a for which X_0 penetrates into C_b through κ_a by the distance b :

$$a = \inf_{\{R_t\}, p_b, p_1, p_2} \|p_1 - p_2\|_2 \quad (72)$$

$$\text{s.t. } \{R_t\} \in \mathcal{R}_{\bar{r}} \quad (73)$$

$$\delta_x(R_T X_0) = b, \quad (74)$$

$$p_b \in \ell_b \cap R_T X_0, \quad (75)$$

$$p_1, p_2 \in C_b \cap \partial R_T X_0, \quad (76)$$

where p_1 and p_2 are the endpoints of κ_a (as in Definition 43).

We now construct a feasible solution to (72). Let $\{R_t\}$ be a feasible solution to (69), so $\delta_x(R_T X_0) = b$, which satisfies (73) and (74). Since $\ell_b \cap R_T X_0$ is nonempty as discussed above, we can pick p_b to satisfy (75), and create C_b centered at p_b . Then $A_b = C_b \cap R_T X_0$ is an arc of radius b (as in Definition 43); we justify that A_b is indeed an arc in the next paragraph. Let p_1 and p_2 be the endpoints (as in Definition 43) of A_b , satisfying (76). Let κ_a be the chord that lies

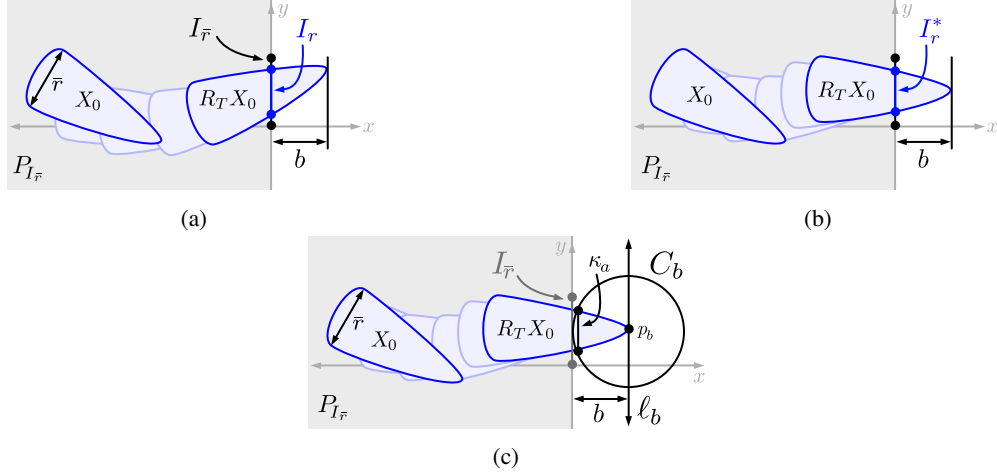


Figure 13: We illustrate Program (69) in Figures 13a and 13b, and Program (72) in Figure 13c. The set X_0 is an arbitrary convex, compact shape, and starts at $t = 0$ in the left half-plane $P_{I_{\bar{r}}}$. The transformation family $\{R_t\}_{t \in [0, T]}$ attempts to pass X_0 through $I_{\bar{r}}$. At time T , $R_T X_0$ is stopped such that its penetration distance through $I_{\bar{r}}$ is the distance b . Program (69) attempts to find the smallest line segment I_r that can be created when passing X_0 through $I_{\bar{r}}$ up to the penetration distance b ; a suboptimal, feasible solution is shown in Figure 13a, and an optimal solution is shown in Figure 13b. Program (72) attempts to find the smallest chord κ_a of a circle C_b for which X_0 cannot penetrate farther than b into C_b through κ_a . This is shown in Figure 13c, which starts from a feasible solution to (69), then centers the circle C_b on a point of $R_T X_0$ that has penetrated to the distance b past $I_{\bar{r}}$. The chord κ_a is defined by points in the intersection of $\partial R_T X_0$ with C_b , and is therefore also a chord of $R_T X_0$. In this case, the optimal κ_a is shown.

between the endpoints of A_b . Then, $R_T X_0$ penetrates into C_b through κ_a by the distance b (as in Definition 63). This is illustrated in Figure 13c.

Now we justify that A_b is indeed an arc of radius b with two endpoints. First, notice that the intersection $C_b \cap R_T X_0$ is nonempty for two reasons. One, because C_b is centered on a point in $\partial R_T X_0$; and two, because $\delta_x(R_T X_0) = b$, which implies that there exists at least one line segment inside $R_T X_0$ that is in the open right half-plane and of length b . Furthermore, because $R_T X_0$ has nonzero volume (Assumption 48), A_b has exactly two endpoints, which lie on the boundary of $R_T X_0$. Otherwise, there would exist a pair of points in $R_T X_0$ that are connected by a line segment that does not lie fully in $R_T X_0$, which would violate the convexity of $R_T X_0$.

Now, we check that $a \in (0, \bar{r})$. Let $\{R_t\}, p_b, p_1, p_2$ be a feasible solution to (72). By construction, X_0 penetrates into C_b through κ_a by $b < \bar{b}$. Then the length a of κ_a is less than \bar{r} , otherwise, by Lemma 57, X_0 could penetrate into C_b through κ_a by no more than b . Now suppose that $a = 0$. Then, by Lemma 61, there can be no nonempty chords of $R_T X_0$ between κ_a and the center of the circle p_b , but then X_0 does not penetrate into C_b through κ_a . ■

Now, we have completed finding the scalars \bar{r} (Lemma 52), \bar{b} (Lemma 57), r (Lemma 62), and a (Lemma 64) that were desired at the outset of Section 6.3. To wrap up, we note what to do if r and a cannot be found exactly, then present two examples of \bar{r} , \bar{b} , r , and a for rectangular and circular robot footprints.

Remark 65. *Since r and a are point spacings for discretizing obstacles, they must be underapproximated if they cannot be found exactly, by logic similar to that described in Remark 55. Otherwise, the robot may be able to penetrate farther than the distance b between them.*

For some convex shapes, such as the rectangle and circle in Examples 66 and 67, r and a can be found analytically. For arbitrary convex shapes, one can use the procedure proposed in Appendix 13 (Lemma 74) for finding \bar{b} , but limit the penetration distance to b ; then one can find r as in Lemma 62 with (68) and find a as in Lemma 64 by placing a circle C_b and finding the chord κ_a .

Example 66. (Rectangular footprint). *Suppose X_0 is a rectangle of length L and width W , with $L > W$. Then $\bar{r} = W$ and $\bar{b} = W/2$. Given $b \in (0, \bar{b})$, $r = 2b$ and $a = 2b \sin(\pi/4)$. A visual proof is in Figure 14a.*

Example 67. (Circular footprint). Suppose X_0 is a circle of radius R . Then $\bar{r} = 2R$ and $\bar{b} = R$. Pick $b \in (0, \bar{b})$. Define the positive angles $\theta_1 = \cos^{-1}\left(\frac{R-b}{R}\right)$ and $\theta_2 = \cos^{-1}\left(\frac{b}{2R}\right)$. Then we find $r = 2R \sin \theta_1$ and $a = 2b \sin \theta_2$. A visual proof is in Figure 14b.



Figure 14: An illustration of the numbers \bar{r}, b, r , and a for rectangular and circular robot footprints (see Examples 66 and 67). The left subfigure shows a rectangular footprint in blue, with length L and width W . The right subfigure shows a circular robot footprint with diameter $2R$. For both footprints, the maximum point spacing \bar{r} (as in Definition 53) is in purple. The supremizing penetration distance \bar{b} (as in Definition 58) is omitted for clarity. The buffer b is in magenta. The point spacing r is in mint green. The arc point spacing a is in orange. The black circle corresponds to the circle C_b used in (72) to find a (see Lemma 64).

6.4 Preserving Safety with Discretized Obstacles

Now we present an algorithm to take a buffered obstacle and discretize its boundary, producing the discretized obstacle X_p . We prove in Theorem 68 that, if the robot is cannot collide with any point in X_p , then it also cannot collide with the obstacles. Finally, we discuss sources of conservatism in the discretization approach.

6.4.1 Constructing the Discretized Obstacle

First, we establish several functions used to discretize the buffered obstacle boundary. Let X_{obs} consist of polygons (as in Assumption 38). Suppose X_0 is the robot's footprint at time 0 (as in Definition 3), which is compact and convex with nonzero volume (as in Assumption 48). Suppose that \bar{r} and \bar{b} are found for X_0 as in Definitions 53 and 58. Select $b \in (0, \bar{b})$, then find r with (69) and a with (72). Buffer the obstacle to produce X_{obs}^b as in (59). Then, by Lemma 44, we can rewrite $\partial X_{\text{obs}}^b = L \cup A$ where L is a finite set of closed line segments (as in Definition 41) and A is a finite set of closed arcs (as in Definition 43). Let n_L be the number of line segments and n_A be the number of arcs. For $i = 1, \dots, n_L$, let $L_i \subset L$ denote the i^{th} segment, and similarly $A_i \subset A$ for the i^{th} arc. Then the function `extractLines` takes in the buffered obstacle X_{obs}^b and returns the set L of all line segments on $\partial X_{\text{obs}}^b$. Similarly, the function `extractArcs` takes in X_{obs}^b and returns the set A of all circular arcs on $\partial X_{\text{obs}}^b$.

Given line segments and arcs, we now define the function `sample`: $\mathcal{P}(\mathbb{R}^2) \times \mathbb{R} \rightarrow \mathcal{P}(\mathbb{R}^2)$ to discretize them. Suppose $S \subset \mathbb{R}^2$ is a connected curve with exactly two endpoints and no self-intersections; note we are conflating a curve with its image. Let $s > 0$ be a distance. Then $P = \text{sample}(S, s)$ is a set containing the endpoints of S . Furthermore, if the total arclength along S is greater than s , then P also contains a finite number of points spaced along S such that, for any point in P , there exists at least one other point that is no farther away than the arclength s along S . Note that the line segments in L and the arcs in A can be parameterized; then the `sample` function can be implemented using interpolation of a parameterized curve.

Suppose that X_p is constructed from a buffered obstacle X_{obs}^b using Algorithm 1. Then X_p contains the endpoints of each line segment or arc of $\partial X_{\text{obs}}^b$, since it is constructed using `sample`. In addition, for each line segment of $\partial X_{\text{obs}}^b$, X_p contains additional points spaced along the line segment such that each point is within the distance r (in the 2-norm) from at least one other point. Similarly, for each arc of $\partial X_{\text{obs}}^b$, X_p contains points spaced along the arc such that each point is within the arclength a of at least one other point; this implies that distance between any pair of adjacent points along each arc is no more than a . Finally, note that X_p is finite because there are a finite number of polygons in X_{obs} (see Assumption 38), each polygon has a finite number of edges, and $r, a > 0$.

Now, we formalize the notion that X_p represents the obstacles X_{obs} without affecting the guarantee of safety. Recall that the purpose of constructing X_p is to map the obstacles X_{obs} into the parameter space K via the map $\pi_K : X \rightarrow K$ as

Algorithm 1 Construct Discretized Obstacle (`discretizeObs`)

```
1: Require:  $X_{\text{obs}}^b \subset X, r \in \mathbb{R}_{\geq 0}, a \in \mathbb{R}_{\geq 0}$ 
2:  $L \leftarrow \text{extractLines}(X_{\text{obs}}^b), A \leftarrow \text{extractArcs}(X_{\text{obs}}^b)$ 
3:  $X_p \leftarrow \emptyset$ 
4: For each:  $i \in \{1, \dots, n_L\}$ 
5:    $X_p \leftarrow X_p \cup \text{sample}(L_i, r)$ 
6: end
7: For each:  $j \in \{1, \dots, n_A\}$ 
8:    $X_p \leftarrow X_p \cup \text{sample}(A_j, a)$ 
9: end
10: Return  $X_p$ 
```

in (58). To ensure safety, the set $\pi_K(X_p)$ must contain all possible unsafe trajectory parameters $\pi_K(X_{\text{obs}})$, which is the complement of the set K_{safe} , leading to the following theorem:

Theorem 68. *Let X_0 be the robot's footprint at time 0 as in Definition 3, with width \bar{r} as in Definition 53. Let $X_{\text{obs}} \subset (X \setminus X_0)$ be a set of obstacles as in Definition 24. Suppose that the maximum penetration depth \bar{b} is found for X_0 as in Definition 58. Pick $b \in (0, \bar{b})$, and find the point spacing r with (69) and the arc point spacing a with (72). Construct the discretized obstacle X_p in Algorithm 1. Then, the set of all unsafe trajectory parameters corresponding to X_{obs} is a subset of the trajectory parameters corresponding to X_p , i.e. $\pi_K(X_p) \supseteq \pi_K(X_{\text{obs}})$.*

Proof. We show that any trajectory parameter outside of those corresponding to X_p cannot cause any point on the robot to enter the set X_{obs} at any time $t \in [0, T]$. If no $q \in \pi_K(X_p)^C$ can cause a collision, then $\pi_K(X_p)^C \subseteq K_{\text{safe}}$, which implies that $\pi_K(X_p) \supseteq \pi_K(X_{\text{obs}})$. First, recall that the robot's high-fidelity model in (1) produces continuous trajectories (by Assumption 1) of the robot's footprint in \mathbb{R}^2 , so we can represent the motion of the robot over the time horizon $[0, T]$ using a transformation family $\{R_t\}$ as in Definition 46.

Suppose $k \in \pi_K(X_p)^C$ is arbitrary, and the robot begins at an arbitrary $\zeta_{\text{hi},0} \in Z_{\text{hi},0}$. Let $\{R_t\}$ be the transformation family that describes the robot's motion when tracking the trajectory parameterized by k . Consider a pair (p_1, p_2) of adjacent points (as in Definition 54) of X_p . Recall that the function `sample` returns the endpoints of any line segment (as in Definition 41) or arc (as in Definition 43), in addition to points spaced along the line segment or arc if necessary. Therefore, by Algorithm 1, (p_1, p_2) is either from a line segment or from an arc of $\partial X_{\text{obs}}^b$. Recall that, by Lemma 44, $\partial X_{\text{obs}}^b$ consists exclusively of line segments and arcs. By construction, if p_1 is on a line segment (resp. arc), then p_2 is within the distance r (resp. a) along the line segment; this also holds if either point is an endpoint of a line segment or arc.

Consider the case when (p_1, p_2) is from an arbitrary line segment L_i of $\partial X_{\text{obs}}^b$. By (59), the distance from X_{obs} to any point on L_i is b . By Lemma 37, when tracking the trajectory parameterized by k , the robot can approach infinitesimally close to p_1 and/or p_2 , but cannot contain them, for any $t \in [0, T]$. So, by Lemma 62 and continuity of the robot's trajectory, no point in the robot can penetrate farther than b through L_i .

Now consider when (p_1, p_2) is from an arbitrary arc A_i of $\partial X_{\text{obs}}^b$. By Equation (59), the distance from X_{obs} to any point on A_i is b . Each such arc is a section of a circle of radius b . By Lemma 37, the robot cannot contain p_1 or p_2 for any $t \in [0, T]$. So, by Lemma 64 and continuity of the robot's trajectory, the robot cannot pass farther than the distance b into A_i through the chord of A_i with endpoints p_1 and p_2 .

Since L_i and A_i were arbitrary, there does not exist any $t \in [0, T]$ for which $R_t X_0 \cap X_{\text{obs}}$ is nonempty. In other words, the robot does not collide with X_{obs} by passing through any line segment or arc of $\partial X_{\text{obs}}^b$. Since k was arbitrary, we conclude that there does not exist any $k \in \pi_K(X_p)^C$ for which the robot collides with any obstacle. Therefore, $\pi_K(X_p)^C \subseteq K_{\text{safe}}$. ■

6.4.2 Conservatism of the Discretized Obstacle in Practice

Our approach has two sources of conservatism. The first is that we can only compute overapproximations to the robot's FRS. The second is that we must buffer obstacles to discretize them.

First, we discuss the FRS overapproximation that we compute in Section 3. Note that, in Theorem 68, the FRS parameter projection map π_K is defined by an exact solution to (D) . However, as per Section 3.2, we can only compute solutions to the relaxed problem (D^b) . This does not affect the safety guarantee of the discretized obstacle, as we note in the following remark.

Remark 69. Suppose (v^l, w^l, q^l) is a solution to (D^l) for some $l \in \mathbb{N}$. Define the map $\pi_K^l : \mathcal{P}(X) \rightarrow \mathcal{P}(K)$ by

$$\pi_K^l(X') = \{k \in K \mid \exists x \in X' \text{ s.t. } w^l(x, k) \geq 1\}. \quad (77)$$

By Lemma 18, X_{FRS} is contained in the 1-superlevel set of w^l . This means that, for any $X' \subset X$, π_K^l overapproximates π_K , i.e. $\pi_K^l(X') \supseteq \pi_K(X')$. Therefore, if $k \in K_{\text{safe}}$ corresponds to some X_{obs} , then $\pi_K^l(X_{\text{obs}})^C \subseteq \pi_K(X_{\text{obs}})^C = K_{\text{safe}}$. In other words, Theorem 68 still holds for π^l .

Now, we discuss the effect of choosing different buffer sizes $b \in (0, \bar{b})$. If the buffer is small, then r and a must be small, according to Lemma (62) and (64). If r and a are small, by Algorithm 1, the points of X_p are spaced closer together, increasing $|X_p|$. Each point in X_p is mapped to a nonlinear constraint at runtime, so increasing $|X_p|$ may increase the execution time of the trajectory optimization. If the buffer is large, then r and a can be larger, but the trajectory optimization may become more conservative, because buffering obstacles reduces the total free space available for the robot to move through. A large buffer may also not reduce the trajectory optimization execution time, because increasing b allows for increasing r and a only up to \bar{r} . So, b should be chosen as small as possible to reduce conservatism, but large enough to enable fast execution times. We describe a strategy for choosing b to balance between these two effects in Appendix 14.

7 Online Trajectory Optimization

This section describes the real-time trajectory planning part of RTD, which is presented in Algorithm 2.

Recall the robot's non-braking trajectory (49), denoted $\zeta_{\text{hi}} : [0, T] \rightarrow Z_{\text{hi}}$, produced by the feedback controller u_k (10) that controls the robot to track the trajectory parameter $k \in K$. Given a user specified cost function $J : K \rightarrow \mathbb{R}$, and an initial robot state $\zeta_{\text{hi},0} \in X_{\text{hi}}$, Algorithm 2 performs trajectory optimization in a real-time, provably safe manner. The algorithm begins with a user-specified initial trajectory parameter k_0 , and predicts the state of the high-fidelity model under the control input u_{k_0} , beginning from $\zeta_{\text{hi},0}$ at $t = \tau_{\text{plan}}$ using (11) from Assumption 9; we assume that $\text{proj}_X(\zeta_{\text{hi},0}) = [x_c, y_c]^\top$, i.e. the robot's state estimate only tracks the center of mass. At each iteration, the algorithm begins by applying the control input $u_{k_j^*}$ to the high fidelity model (Line 4), bringing the robot's state to $\zeta_{\text{hi},j+1}$. While this control input is being applied, the algorithm senses surrounding obstacles (Line 5), builds a representation for them (Line 6), applies the `buffer` to produce the buffered obstacle as in (59) (Line 7), then represents the obstacles as a set of discrete points X_p by applying Algorithm 1 (Line 8). In addition, the control input to be applied in the next iteration is computed (Line 9). We describe the behavior of the function `OptK` in greater detail below; in brief, it uses the obstacle constraints and user-specified cost function to generate an optimal control input $u_{k_{j+1}^*}$ that is applied during the next iteration. Next, we compute the future position of the high-fidelity model under the optimal control input $u_{k_{j+1}^*}$ beginning from $\zeta_{\text{hi},j+1}$ using (11) as in Assumption 9 (Line 10).

Note, at the same time that Lines 5-10 are executing, the control input $u_{k_j^*}$ is applied to the high fidelity model (Line 4), bringing the robot's state to $\zeta_{\text{hi},j+1}$. As a result, the function `OptK` takes in the state of the robot after the application of control input $u_{k_j^*}$ at t_{j+1} , user-specified cost function J , w^l , obstacle points, and planning time. `OptK` either finds a new k_{j+1}^* and returns the associated feedback controller $u_{k_{j+1}^*}$ as in (10); or it returns the braking controller u_{brake} associated with the previous iteration's controller $u_{k_j^*}$ (as in Assumption 30). If the braking controller is applied, the robot stops within the FRS spatial projection corresponding to k_j^* given by $\pi_X^l(k_j^*) \subset X$ from (47), which is possible by Assumption 32. Note that uncertainty in localization and state estimation is not a focus of this paper, but can be accounted for in either the FRS computation (by increasing g and expanding X_0) or obstacle buffering (by increasing b).

Algorithm 2 is real-time feasible due to Algorithm 1, written here as the `discretizeObs` function (Line 8); and due to the enforcement of τ_{trajopt} in the `OptK` function (Line 9). Recall from Assumption 26 that the time to execute one planning iteration, τ_{plan} , is equal to the time to sense and buffer obstacles and predict the next position of the robot, which is denoted by τ_{process} , plus the time to run `OptK`, which is denoted by τ_{trajopt} .

Next, we comment on the formulation of `OptK`. From Theorem 68 and Remark 69, we know that X_p safely represents the obstacle (i.e. $\pi_K^l(X_p) \subseteq K_{\text{safe}}$). In other words, if (v^l, w^l, q^l) is a feasible solution to (D^l) (see Section 3.1), we can evaluate w^l on the discretized obstacle X_p to conservatively approximate the corresponding set of unsafe trajectory parameters. As a result, given an arbitrary cost function $J : K \rightarrow \mathbb{R}$, the optimization program `OptK` takes

Algorithm 2 Reachability-based Trajectory Design (RTD) Online

1: **Require:** $b, r, a, \tau_{\text{plan}}, \tau_{\text{trajopt}}, T \in \mathbb{R}_{\geq 0}; w^l \in \mathbb{R}_{2J}[x, k]; k_0 \in K; \zeta_{\text{hi},0} \in Z_{\text{hi}}; \text{ and } J : K \rightarrow \mathbb{R}.$
2: **Initialize:** $j = 0, t_j = 0, k_j^* = k_0, \text{ and } \zeta_{\text{hi},j+1} = \zeta_{\text{hi}}(t_j + \tau_{\text{plan}}; \zeta_{\text{hi},0}, k_j^*).$
3: **Loop:**
4: **Apply** $u_{k_j^*}$ to the robot for $[t_j, t_j + \tau_{\text{plan}}).$
5: **Sense** obstacles $\{X_{\text{obs},i}\}_{i=1}^{n_{\text{obs},j}}.$ // Lines 5 – 10 execute simultaneously with Line 4
6: $X_{\text{obs}} \leftarrow \bigcup_{i=1}^{n_{\text{obs},j}} X_{\text{obs},i}.$
7: $X_{\text{obs}}^b \leftarrow \text{buffer}(X_{\text{obs}}, b).$
8: $X_p \leftarrow \text{discretizeObs}(X_{\text{obs}}^b, r, a).$
9: **Compute** $u_{k_{j+1}^*} \leftarrow \text{OptK}(\zeta_{\text{hi},j+1}, J, w^l, X_p, \tau_{\text{trajopt}}).$
10: $\zeta_{\text{hi},j+2} \leftarrow \zeta_{\text{hi}}(2\tau_{\text{plan}} + t_j; \zeta_{\text{hi},j+1}, k_{j+1}^*).$
11: $t_{j+1} \leftarrow t_j + \tau_{\text{plan}}$ and $j \leftarrow j + 1.$
12: **End**

the following form:

$$\begin{aligned} & \min_k J(k) \\ & \text{s.t. } w^l(p, k) \leq 0 \quad \forall p \in X_p. \end{aligned} \tag{78}$$

This formulation has a finite list of constraints and a low-dimensional decision variable k , which allows OptK to typically terminate within the time limit τ_{trajopt} . See Appendix 14 for more details about the runtime of OptK .

Finally, we check that Algorithm 2 is provably safe.

Remark 70. *From Theorem 35, we know that the robot can either find a safe plan of duration T (as in Definition 29) or brake for all $t \geq 0$ as long as it has a safe plan at $t = 0$. So, in Algorithm 2, Theorem 35 proves that Lines 4 and 5 are safe by lower-bounding D_{sense} , and assumes that Lines 6 – 9 are safe. Then, Theorem 68 proves that Lines 6 – 9 are safe, by constructing X_p such that $\pi_K^l(X_p) \subseteq K_{\text{safe}}$ (as in Definition 36) at each iteration. By Assumption 9, Line 10 predicts the robot’s position to within a box of size $\varepsilon_x \times \varepsilon_y$, and by Assumption 27, the obstacle X_{obs} is expanded to compensate for this state prediction error. So, since all of the lines inside the loop are safe, Algorithm 2 is safe.*

8 Application

This section details the application of RTD to two robots: the Segway (Figure 2a), and the Rover (Figure 2b). Both robots use Algorithm 2 (as in Section 7) for online safe trajectory planning, demonstrated in simulation (Section 9) and on hardware (Section 10).

8.1 Segway

The Segway is a differential-drive robot. We apply RTD to the Segway to show that our method can provide collision-free trajectory planning in unstructured, random environments.

8.1.1 Dynamic Models

The robot has a circular footprint with a 0.38 m radius. It is limited to a maximum yaw rate $\omega = \pm 1$ rad/s and a maximum speed $v = 1.25$ m/s (as in Assumption 6). Example 7 presents the Segway’s high-fidelity model (4) and feedback controller (5) and (6). Example 13 presents the trajectory-tracking model (16) used to compute the FRS. Motion capture data is used to find the parameters $\beta_\omega = 2.95$, $\beta_v = 3.00$, and $\beta_v = \beta_\theta = 0$ from (4) for the hardware depicted in Figure 2a. In simulation, β_γ and β_α are as in the hardware, and $\beta_v = \beta_\theta = 10$. Given a current yaw rate, ω , the commanded yaw rate, ω_{des} , is restricted to be within ± 0.5 rad/s of ω at each planning iteration.

The Segway fulfills the assumptions on state estimation, tracking error, and braking as follows. State estimation, as in Assumption 9, has no error in simulation, so $\varepsilon_x = \varepsilon_y = 0$. On the Segway hardware, we find that SLAM using Google Cartographer with a planar lidar results in $\varepsilon_x = \varepsilon_y = 0.1$ m [18]. The tracking error function g is constructed

to satisfy Assumption 10 by fitting to simulated tracking error data, as shown in Appendix 14. The braking controller is as in Example 31, and uses the same gains β_γ , β_α , β_θ , and β_v as the non-braking controller for the high-fidelity model in Example 7. Assumption 32 requires that all braking trajectories lie within the FRS for persistent feasibility. Designing and validating such a braking controller can be done with SOS programming, but is not the focus of this work. Figure 8 illustrates that the braking controller satisfies Assumption 32.

8.1.2 FRS Computation

The Segway's FRS is computed over a time horizon $T = 1$ s, chosen as per Example 34. The tracking error function g is reported in Example 76 in Appendix 14. The FRS computation uses the trajectory-producing model in Example 13 (from Section 2.2), in the program (D^l) with $l = 6$ (from Section 3.2). Two FRS's are computed: one for low-speed maneuvers (from 0.0–0.5 m/s), and one for high-speed maneuvers (from 0.0–1.25 m/s), detailed in Appendix 14 and discussed briefly below.

8.1.3 Obstacle Representation and Online Planning

The width of the segway is $\bar{r} = 0.76$ m (Definition 53) and the maximum penetration distance is $\bar{b} = 0.38$ m (Definition 58). In the simulations, we use a buffer size of $b = 0.07$ m, which results in a point spacing $r = 0.38$ m and arc point spacing $a = 0.10$ m as per Definition 45 and Example 67. On the hardware, we use a buffer size of $b = 0.05$ m, so $r = 0.37$ m and $a = 0.10$ m.

In Appendix 14.2, we discuss in detail how the Segway's low- and high-speed FRS's are used, a procedure we call **FRS swapping**. Here, we present a brief overview. The low-speed FRS spans a smaller range of initial conditions and desired velocities than the high-speed FRS, which reduces the magnitude of the tracking error function g , meaning that the low-speed FRS is less conservative than the high-speed FRS at the same speed (notice that the high-speed FRS contains all of the speeds that can be selected when planning with the low-speed FRS). When the Segway is planning with the high-speed FRS but has an average speed below 0.5 m/s, it swaps to planning with the low-speed FRS. If planning with the low-speed FRS but traveling at an average speed higher than 0.45 m/s, the Segway swaps to the high-speed FRS, which allows it to pick speeds up to 1.25 m/s in the subsequent planning iteration. FRS swapping reduces the conservatism of RTD on the Segway. Since the low- and high-speed FRS's have overlapping sets of initial conditions, FRS swapping does not impact the safety guarantee.

8.2 Rover

The Rover is a front wheel steering, rear wheel drive platform, and demonstrates the utility of RTD in passenger robot applications.

8.2.1 Dynamic Models

The Rover has a rectangular footprint of length 0.6 m and width 0.3 m centered 0.009 m in front of the center of mass. The top speed and yaw rate are limited to 2 m/s and ± 1.5 rad/s respectively (as in Assumption 6). It has mass $m = 7.78$ kg, moment of inertia about the vertical axis $I_z = 0.2120$ kg m², wheelbase $l = 0.3302$ m, distance from center of mass to rear wheel $l_r = 0.12$ m, and steering gain $\beta_\delta = 4.3$.

The Rover's high-fidelity model is adapted from [35]:

$$\underbrace{\frac{d}{dt} \begin{bmatrix} x(t) \\ y(t) \\ \theta(t) \\ v_x(t) \\ \delta(t) \end{bmatrix}}_{\zeta_{hi}(t)} = \underbrace{\begin{bmatrix} v_x(t) \cos(\theta(t)) - \frac{l_r v_x(t)}{l} \tan(\delta(t)) \sin(\theta(t)) \\ v_x(t) \sin(\theta(t)) + \frac{l_r v_x(t)}{l} \tan(\delta(t)) \cos(\theta(t)) \\ \frac{v_x(t)}{l} \tan(\delta(t)) \\ \frac{f_{u_0}(u_0, v_x(t), \dot{\theta}(t)) - m_o \tan(\delta(t)) \sec^2(\delta(t)) \dot{\delta}(t) v_x(t)}{m + m_o \tan^2(\delta(t))} \\ \beta_\delta (f_{u_1}(u_1) - \delta(t)) \end{bmatrix}}_{f_{hi}(t, \zeta_{hi}(t), u(t))}. \quad (79)$$

This model utilizes kinematic steering assumptions, which are commonly used to model cars operating at low speeds [40]. The inputs are two PWM voltage commands, (u_0, u_1) , to the traction motor and steering servo. Motion capture data was used to fit functions, f_{u_0} and f_{u_1} , that map the PWM commands to driving force, F_x , and desired wheel angle,

δ_{des} . The steering wheel angle is bounded by $|\delta(t)| \leq 0.66$ rad for all t , and the functions f_{u_0} and f_{u_1} are Lipschitz continuous, so (79) is Lipschitz continuous in t, ζ_{hi} , and u as required by Assumption 1.

Example 19 presents the Rover’s trajectory-producing model (30). Recall that the trajectory-tracking model (13), is the trajectory-producing model plus the tracking error functions (as in Assumption 10). For the Rover, the trajectory-tracking model is:

$$\dot{\zeta}_1(t) = \underbrace{\begin{bmatrix} k_3 \cos(\theta(t)) - l_r \omega(t, k) \sin(\theta(t)) \\ \omega(t, k) \end{bmatrix}}_{f_1} + \underbrace{\begin{bmatrix} 0.06 \\ 0 \end{bmatrix}}_{g_x} d(t) \quad (80)$$

$$\dot{\zeta}_2(t) = \underbrace{\begin{bmatrix} k_3 \sin(\theta(t)) + l_r \omega(t, k) \cos(\theta(t)) + 0.09(1-t)^2 k_2 \\ \omega(t, k) \end{bmatrix}}_{f_2} + \underbrace{\begin{bmatrix} 0.15(1-t)^2 \\ 0 \end{bmatrix}}_{g_y} d(t) \quad (81)$$

where the yaw rate $\omega(t, k) = \frac{k_2}{2}t + k_1(1-t)$ is given by (31) with $T_h = 2$ s.

The Rover’s braking controller, as in Assumption 30, converts a previously-planned trajectory to a braking trajectory by first converting the trajectory from a function of time to a function of distance traveled, i.e. arclength. The Rover then uses a proportional controller for longitudinal acceleration to brake to 0 m/s, while a proportional controller for the steering attempts to match the robot’s center of mass and heading coordinates to the previously-planned trajectory as a function of the distance traveled during braking.

The Rover satisfies the assumptions on state estimation, tracking error, and braking. For state estimation, as with the Segway, there is no error in simulation; on the hardware, $\varepsilon_x = \varepsilon_y = 0.1$ m. The tracking error functions in (80) and (81) are fit to trajectory data as with the Segway. The braking controller is verified empirically. Recall that SOS programming can be used to verify the braking controller, but that is not a focus of this work; the FRS for the Rover’s expanded footprint is large enough that designing a braking controller to satisfy Assumption 32 is not difficult.

8.2.2 FRS Computation

The Rover’s FRS is computed over a time horizon $T = 1$ s, chosen to satisfy Assumption 32, based on a maximum braking distance of 1.25 m at 2 m/s and a planning time $\tau_{\text{plan}} = 0.375$ s. To compute the FRS, first, (D_i^4) is solved for the subsystems $i = 1, 2$ in (39) and (40). Then, (41) with relaxation $\alpha = 5$ reconstructs the full system FRS.

8.2.3 Obstacle Representation

As mentioned in Example 19, to capture rotations of the Rover with a maximum heading of ± 0.5 rad, its footprint X_0 is enlarged to a rectangle of length 0.64 m and width 0.56 m. For this enlarged footprint, $\bar{r} = 0.56$ m (Definition 53) and the maximum penetration distance is $\bar{b} = 0.28$ m (Definition 58). We use a buffer $b = 0.01$ m, resulting in the point spacing $r = 0.02$ m and arc point spacing $a = 0.014$ m as per Example 66.

9 Simulation Results

This section compares RTD against a Rapidly-exploring Random Tree (RRT) planner based on [23, 36, 39] and a Nonlinear Model-Predictive Control (NMPC) planner, GPOPS-II [38]. The RRT and NMPC implementations are detailed in Section 9.2. The contribution of this section is the comparison of RTD to RRT and NMPC, and the demonstration of safety of RTD over thousands of simulations. The simulation results are presented in Table 4 for the Segway and Table 5 for the Rover.

Recall that trajectory planning is performed in a receding-horizon fashion, where the robot computes a plan of duration T s while executing a previously-determined plan. The robot is also limited by a physical sensor horizon, D_{sense} . The robot is given a finite amount of time, τ_{plan} , within which it must find a plan, and it executes a duration $\tau_{\text{move}} \leq T$ of a given plan. Note that in real-world applications and previous sections of this paper, τ_{move} is the same as τ_{plan} . We define τ_{move} separately in this section because we simulate the RTD, RRT, and NMPC planners with and without real-world timing limits to compare performance. For the Segway, we use $\tau_{\text{move}} = 0.5$ s, and for the Rover, $\tau_{\text{move}} = 0.375$ s. Also recall that, as per Assumption 26, $\tau_{\text{plan}} = \tau_{\text{process}} + \tau_{\text{trajopt}}$, where τ_{trajopt} is the time limit enforced on the trajectory planner at each planning iteration. For all planners and all simulations, we assume that $\tau_{\text{process}} = 0$.

Finally, recall by Assumption 9 that the robot can predict its future state to within ε_x and ε_y in the x - and y -directions respectively. For all planners and all simulations, since the robot is represented as the high-fidelity model (1), there is no state estimation error, so $\varepsilon_x = \varepsilon_y = 0$.

9.1 Scenarios

The simulated scenario for the Segway is a 9×5 m² room, with the longer dimension oriented east-west. The room is filled with 6 to 15 randomly-distributed box-shaped obstacles with a side length of 0.3 m. A random start location is chosen on the west side of the room and a random goal is chosen on the east side. The simulated environment is similar to the hardware demo depicted in Figure 2a. For high-level path planning, A* is applied to a grid in the x and y coordinates; this provides a coarse global path and intermediate waypoints (position and heading). At each planning iteration, the cost function given to `OptK` (as in Section 7 Algorithm 2) attempts to minimize the distance to the current waypoint. A trial is considered successful if the Segway reaches the goal without touching any obstacles.

The simulated scenario for the Rover is a larger version of the mock road depicted in Figure 2b, which mimics a highway environment. The simulated road lies along the x -direction (oriented east-west) and is centered at $y = 0$. It is 2.5 m wide (including the shoulder), with two 0.6 m wide lanes centered at $y = 0.3$ m and $y = -0.3$ m. The Rover plans trajectories with speeds of 1–2 m/s. In each trial, three 0.6×0.3 m² box-shaped obstacles are placed in the right, left, and right lanes respectively. This obstacle arrangement is used to force the Rover to attempt two lane changes per trial; note that the RTD, RRT, and NMPC trajectory planners are all general implementations (as described in Section 9.2), not specialized to this particular obstacle arrangement. The obstacles all have a heading of 0 rad relative to the road, and their centers are allowed to vary by 0.15 m from lane center in the y -dimension. The spacing between the obstacles in the x -direction is given by a normal distribution with a mean of 4 m and standard deviation of 0.6 m. The Rover begins each trial centered in the right lane, with a velocity of 2 m/s. A trial is considered successful if the Rover crosses a line positioned 8 m after the third obstacle without intersecting any obstacle or road boundary (i.e. crashing). For high-level path planning, a desired waypoint is placed a set distance ahead of the robot and centered in the current lane. If the waypoint is inside or behind an obstacle relative to the Rover, the waypoint is switched to the other lane. At each planning iteration, the cost function given to `OptK` minimizes the Rover’s x and y position of the center of mass relative to the current waypoint, with the cost for y weighted twice as heavily as that of x . It was found empirically that placing the waypoint 4 m ahead of the Rover at each planning iteration causes it to switch to the other such the Rover is far enough from the obstacle to be capable of performing a lane change; this 4 m “lookahead distance” was used for all three planners. An additional constraint ensures the planned trajectory keeps the Rover’s center of mass within the lane lines. This is done by creating an artificial “wall” obstacle that is half of the Rover’s width from the edges of the road, which gives the road a shoulder. This wall obstacle is passed to every planner at every planning iteration.

9.2 Trajectory Planner Implementation

The simulations are run in MATLAB on a 2.10 GHz computer with 1.5 TB of RAM. Timeouts are enforced with Matlab’s `tic` and `toc` functions. If any of the planners fail to find a solution within τ_{plan} during a planning iteration, the robot attempts to brake along the previously-identified path if one exists, or else brakes in a straight line. For all of the planners, if the Segway has braked and did not crash, one planning iteration is spent rotating in place towards the current waypoint before replanning.

9.2.1 RTD

The Segway simulations use SNOPT [14] to solve the online trajectory optimization `OptK` (see Program (78) and Algorithm 2 Line 9). The solver’s initial guess is chosen to turn towards the current waypoint. The cost function is the robot’s Euclidean distance at time T to the waypoint generated by the high-level A* planner.

The Rover simulations use MATLAB’s `fmincon` to solve `OptK`. The cost function is the Euclidean distance at time T from the planned trajectory’s endpoint to the waypoint, weighting error in x vs. error in y at a ratio of 1:2. The initial guess is determined by identifying which lane the current waypoint is in and selecting trajectory parameters to reach the lane center at the robot’s maximum speed.

For both robots, RTD uses an optimality tolerance of 10^{-3} . When `OptK` is called, points in X_p that lie outside of the FRS for any trajectory parameter $k \in K$ are discarded. Additionally, points that are unreachable due to physical limitations of the robots, such as the turning radius of the Rover, are discarded.

9.2.2 RRT

The Segway and Rover use similar RRT implementations, based on several papers [23, 36, 39], which describe a variety of heuristics for growing a tree of a robot’s trajectories with nodes in the high-fidelity state space. Both RRT implementations use the entire duration τ_{plan} to plan a trajectory at each planning iteration.

To account for the robot’s footprint, obstacles are buffered by Minkowski sum with a polygonal outer approximation of a closed disk, with radius given by the desired buffer distance (see Experiment 1 in Section 9.3.1 for how we empirically select the buffer). This produces a representation of each buffered obstacle as a collection of half-planes.

The RRT planner begins by checking if the previously-planned trajectory is still feasible [23], meaning that none of its nodes lie inside any buffered obstacles. If the past trajectory is feasible, the tree is initialized with the previous plan’s nodes; if the past trajectory is infeasible, the tree is initialized from the robot’s initial state. New nodes of the tree are created by first choosing a random existing node, with the choice biased towards more recently-generated nodes. From the randomly-chosen node, the high-fidelity robot model is forward-integrated under a random desired yaw rate and desired speed [23, 39]. Forward-integration of the dynamics returns points in the robot’s xy -subspace X distributed in time by a time discretization. A new node is discarded if any of these points lie inside any buffered obstacle, outside of the robot’s environment (the room for the Segway and the road for the Rover), or outside the robot’s sensor horizon. In addition, for the Segway, recall (from Section 9.1) that A^* is used for the high-level plan; nodes farther than 1.5 m from the A^* path are discarded [36]. For both the Segway and the Rover, if no feasible nodes can be found, the robot attempts to brake while staying spatially along its planned trajectory from the previous planning iteration.

Forward integration of the robot’s dynamics is required for dynamic feasibility of the RRT trajectory plans, given the complexity of the high-fidelity models of the Segway and Rover [6]. The edge time, or total duration of each forward-integration, along with the time discretization, are heuristic choices that affect the computation time and complexity of paths that the RRT can generate; these numbers were selected empirically for each system. Our implementation makes use of MATLAB’s symbolic and function generation toolboxes. For the Segway and Rover, we generate integration functions that take in an initial condition and return a trajectory of the robot’s dynamics, forward-integrated with an RK4 method, for a predetermined edge time and step size. We confirmed that calls to this function are as fast or faster than a C++ implementation by forward integrating each robot’s dynamics from random initial conditions using the ODEINT C++ library [1].

For both the Segway and Rover, the high-level planners generate intermediate waypoints as described in Section 9.1. When growing the RRT, samples are biased to turn towards waypoints as described in [23]. It was found that the cost function used for RTD and NMPC can cause the RRT planner to pick long paths with large changes in yaw rate because path smoothness is not included in the cost. To combat this, we instead set the RRT’s cost at each node as the cumulative distance from the root node, plus a penalty for lying close to obstacles as in [23], which was found empirically to reduce the number of crashes. Once the RRT has planned for the duration τ_{plan} , we select the top 10% or top 50 (whichever is less) of nodes closest to the waypoint, then choose the node with the lowest cost among these to produce the trajectory plan. Additional costs or heuristics to encourage smoothness were not implemented, because, in this study, the planners are solely evaluated on number of crashes and their ability to safely reach the goal.

For the Rover, we found that forward-integrating the high-fidelity model (79) was too slow to generate many nodes within τ_{plan} s. As a result, we use the following simplified vehicle model for the Rover’s RRT:

$$\frac{d}{dt} \begin{bmatrix} x(t) \\ y(t) \\ \theta(t) \\ v_x(t) \\ \delta(t) \end{bmatrix} = \begin{bmatrix} v_x(t) \cos(\theta(t)) - \frac{l_r v_x(t)}{l} \tan(\delta(t)) \sin(\theta(t)) \\ v_x(t) \sin(\theta(t)) + \frac{l_r v_x(t)}{l} \tan(\delta(t)) \cos(\theta(t)) \\ \frac{v_x(t)}{l} \tan(\delta(t)) \\ \beta_v (v_{\text{des}}(t) - v_x(t)) \\ \beta_\delta (\delta_{\text{des}}(t) - \delta(t)) \end{bmatrix}. \quad (82)$$

The control inputs (which are sampled to create nodes) are desired velocity v_{des} and desired wheel angle δ_{des} . We found that trajectories generated with the gain $\beta_v = 2.0$ can be closely tracked by the Rover’s low-level controller, since all commanded and initial velocities result in accelerations within the Rover’s limits. The Rover’s RRT has an additional heuristic to encourage lane keeping: when there are no obstacles between the Rover and waypoint, the standard deviation of sampled yaw rates and the cost of nodes lying close to the lane center are reduced.

9.2.3 NMPC

The Segway and Rover both use GPOPS-II for the nonlinear model predictive control planner [38]. GPOPS-II is an algorithm that approximates the trajectory planning problem as a polynomial optimization program. This software uses internal heuristics to choose a finite number of collocation points, then evaluates the polynomial approximation of the robot’s dynamics and obstacle avoidance constraints at each of these points. The accuracy of the solution and the run time of the algorithm is dependent on the tolerance of the polynomial approximation.

Obstacles are represented as constraints on the x and y coordinates of the robot’s center of mass at each collocation point. Each obstacle is buffered using a Minkowski sum with a polygonal outer-approximation of a closed disk with radius given by a user-selected buffer distance (see Section 9.3.1). This representation means that, to check for collision of a trajectory with an obstacle, a finite number of half-plane checks are performed per obstacle per collocation point. If no feasible trajectory can be found within τ_{plan} , the robot attempts to brake while staying spatially along its planned trajectory from the previous planning iteration.

For the Segway, the NMPC planner chooses a desired yaw rate and velocity as the control input at each collocation point, and plans with the robot’s dynamic model (4) from Example 7. The planner is given a coarse trajectory guess at the first planning iteration, and each subsequent iteration is seeded with the previous iteration’s result. The GPOPS-II parameters used are: 4–10 collocation points per phase and a mesh tolerance of 10^{-6} .

For the Rover, it was found that GPOPS-II was unable to plan trajectories of 0–2 s in length in under 5 minutes when using the full robot model (79). This is because the function relating the PWM control inputs to driving force, f_{u_0} , differs for acceleration, coasting, and braking inputs. To reduce computation time, GPOPS-II plans with the simplified model (82). The GPOPS-II parameters used for the Rover are: 4–10 collocation points per phase and a mesh tolerance of 10^{-3} . Reducing the mesh tolerance decreases the computation time and accuracy of solutions. Since accuracy is reduced, GPOPS-II sometimes returns solutions that are infeasible for the Rover’s dynamics; we discard such solutions if they enter an “inner” buffer around each obstacle, which is set to 0.1 m less than the specified obstacle buffer.

9.3 Experiments

For each robot, we generate 1,000 random trials that fit the scenarios described in Section 9.1. Since these are randomly generated, it is not guaranteed that feasible (i.e. collision-free) paths exist from the start to the goal in every trial. This is useful, because it requires planners to be safe even when the high-level trajectory planner can only find infeasible trajectories. We run a series of experiments to explore the performance of these three trajectory planners when we relax or enforce requirements of real-time planning and real sensor horizons. We also explore the effect of enforcing a minimum planning time horizon for RRT and NMPC, since RTD specifies a minimum time horizon for persistent feasibility (see Remark 73 in Section 2). The results of the comparison between RTD, RRT, and NMPC are presented in Table 4 for the Segway and Table 5 for the Rover.

Experiment 1 (Section 9.3.1) determines the distance used to buffer obstacles for RRT and NMPC, as discussed in Section 9.2; this is because, to the best of our knowledge, it is unclear how large obstacle buffers need to be to ensure safety for these methods. This experiment does not enforce real-time planning or limited sensor horizon requirements, to ensure that the planners have enough time and information to plan. To relax the real-time requirement, τ_{move} is the same amount of time per planning iteration as is used on the hardware (0.5 s for the Segway and 0.375 s for the Rover), but τ_{plan} is large to give each planner time to find a plan. To relax the sensor-horizon, D_{sense} is large enough that each planner has obstacle information about the entire scene from $t = 0$ s onwards.

Experiment 2 (Section 9.3.2) explores the effect of enforcing real-time planning and a limited sensor horizon on the planners. In this case, $\tau_{\text{plan}} = \tau_{\text{move}}$, meaning that each robot can only plan over the duration that it moves at each planning iteration. The sensor horizon D_{sense} is chosen to reflect each robot’s hardware. The buffer used for RRT and NMPC is the buffer that performed best in Experiment 1. The buffer for RTD is chosen in $(0, \bar{b})$ as described in Section 8 to ensure safety.

Experiment 3 (Section 9.3.3) shows that RTD performs provably safe trajectory planning in real time when subject to the minimal sensor horizon given by Theorem 35. The minimum sensor horizon is significantly smaller than the sensor horizon that each robot’s hardware is capable of (e.g., the Segway’s minimal sensor horizon is 1.9 m, whereas its hardware has a sensor horizon of 4 m), but RTD is still safe. RRT and NMPC are not tested in this experiment.

9.3.1 Experiment 1: Buffer Size for RRT and NMPC

The goal for Experiment 1 is to determine how to buffer obstacles for RRT and NMPC. To the best of our knowledge, these planners do not prescribe a provably-safe buffer size, and only track the robot’s center of mass. Recall that, by contrast, RTD considers the motion of the footprint of the robot, and provides a range of provably safe buffer sizes. To ensure that the buffer size is the only parameter that influences RRT and NMPC, this experiment relaxes the real-time and limited sensor horizon requirements, giving the planners enough time and information to find a plan at most planning iterations.

The parameters used for Experiment 1 are as follows. For the Segway, $\tau_{\text{move}} = 0.5$ s, $\tau_{\text{plan}} = 10$ s, and $D_{\text{sense}} = 100$ m. For the Rover, $\tau_{\text{move}} = 0.375$ s, $\tau_{\text{plan}} = 10$ s, and $D_{\text{sense}} = 50$ m. Since $\tau_{\text{plan}} > \tau_{\text{move}}$, the real-time requirement is relaxed. Since D_{sense} is large, the limited sensor horizon requirement is relaxed. For both the Segway and the Rover, obstacles are buffered by Minkowski sum with a polygonal outer approximation of a closed disk (see Section 9.2). For the Segway, since the robot’s radius is 0.38 m, we test buffer sizes of 0.40, 0.45, and 0.50 m. Since the Segway’s braking distance is no more than 0.625 m from 1.25 m/s, we also test a buffer size of 0.65 m as per Example 31. For the Rover, RRT and NMPC algorithms are tested with buffer sizes of 0.15, 0.25, and 0.35 m. The Rover’s braking distance of 1.25 m from 2 m/s is too large to use for uniform buffering, and non-uniform buffering introduces a heuristic for RRT and NMPC that we do not test.

We expect the results of Experiment 1 to show that, as the buffer size is increased for both planners and both robots, the number of crashes reduces (because any plan that avoids a buffered obstacle places the robot farther away from the actual obstacle for a larger buffer size), and the number of goals reached reduces (because a larger buffer reduces the amount of free space available to each planner). We expect no crashes for either planner with a buffer size of 0.65 m for the Segway.

The results of Experiment 1 are summarized in Table 4 for the Segway and Table 5 for the Rover. Recall that, since the trials are randomly generated, we do not expect every trial to have a collision-free path from start to goal. On the Segway, RRT and NMPC fulfill the expectation that, as the buffer size increases, the number of goals and crashes both reduce. On the Rover, we see that the buffer size of 0.15 m is so small that RRT crashes too often to reach the goal compared to the buffers of 0.25 and 0.35 m; NMPC is able to reach the goal frequently for all three buffer sizes, and surprisingly has no crashes for 0.25 and 0.35 m buffers.

We now discuss the results of Experiment 1. Crashes occur for the RRT and NMPC planners for two reasons. First, the smaller buffer sizes are potentially too small to compensate for both robots’ inability to perfectly track a planned trajectory (recall that, in our implementation, RRT plans trajectories with an RK4 approximation of the dynamics, and NMPC uses a polynomial approximation of the dynamics). Second, if the trajectory planner is unable to find a feasible trajectory at a planning instance, the robot attempts to brake along the previously-planned trajectory, but there is no guarantee that this is possible while staying safe for these methods. We address the first cause in subsequent experiments by choosing an RRT and NMPC buffer size of 0.45 m for the Segway and 0.25 m for the Rover. This choice is a balance between a high success rate and a low crash rate. We do not address the second cause, because this introduces a heuristic that, to the best of our knowledge, is not provided in the literature for RRT or NMPC.

We also test RRT and NMPC on the Segway with buffer sizes of 0.65 m, to check that, if no feasible solution is found in a planning iteration, both methods should always be able to brake without crashing. Both methods indeed have 0 crashes with this buffer size, but it results in conservative performance, with 58.7% of goals reached for RRT and just 1.5% of goals reached for NMPC. The NMPC performance drop is likely due to the large number of half-planes required to represent each buffered obstacle, meaning that even $\tau_{\text{plan}} = 10$ s is not enough time to find feasible solutions; this could be remedied with a different obstacle representation, but is not the focus of this work.

Segway Experiment 1		RRT [23, 36, 39]		NMPC [38]	
		Goals	Crashes	Goals	Crashes
Buffer [m]	0.40	80.4	16.9	83.5	1.1
	0.45	74.2	10.0	82.1	0.4
	0.50	70.0	6.5	75.9	0.2
	0.65	58.7	0.0	1.5	0.0

Table 2: Comparison of success and crash rates for varying buffer sizes for the Segway. A buffer size of 0.45 m provides the best balance of performance and safety for both RRT and NMPC. The Segway’s braking distance of 0.625 m from 1.25 m/s means that the 0.65 m buffer prevents RRT and NMPC from crashing, but both methods become much more conservative with this buffer.

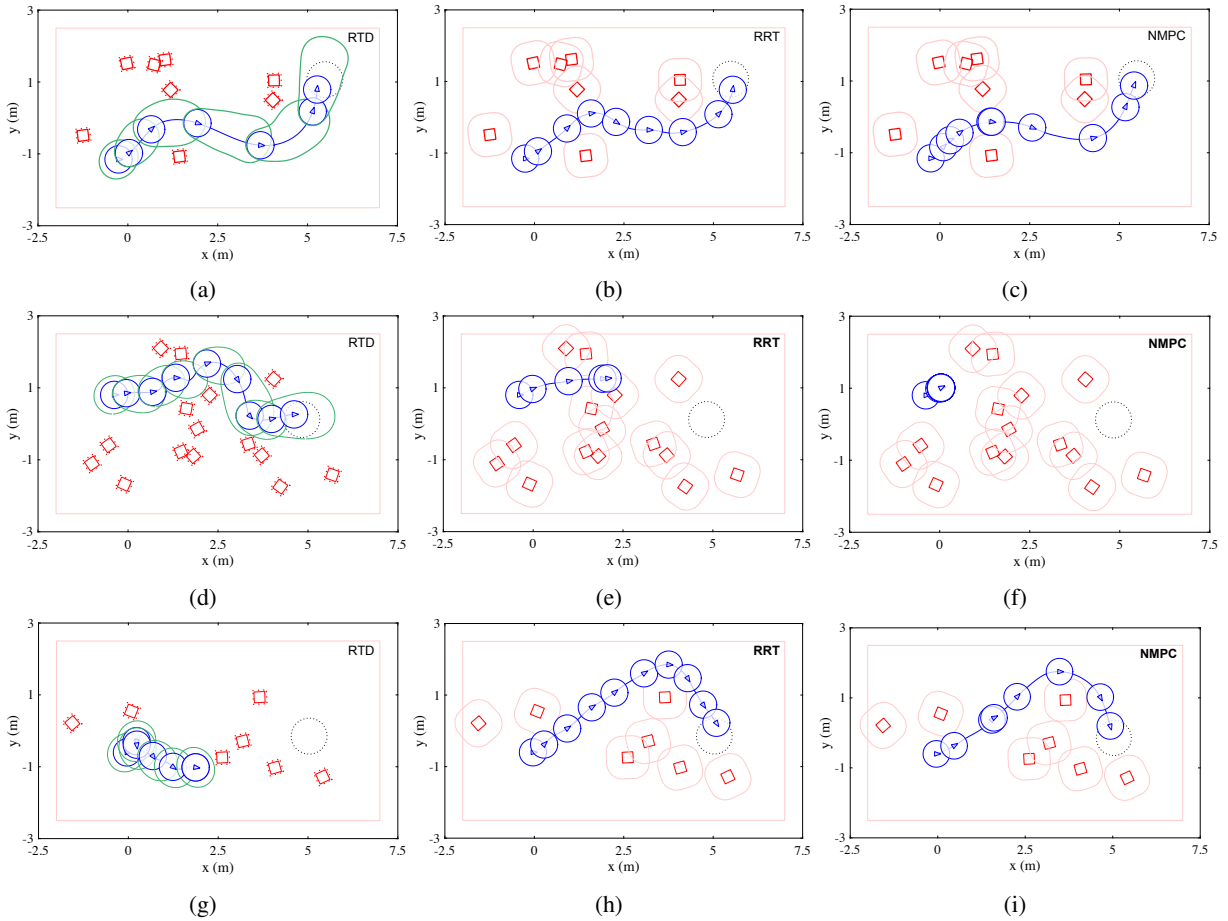


Figure 15: Sample scenarios from Experiments 1 (RRT and NMPC) and 2 (RTD) (Sections 9.3.1 and 9.3.2) for the Segway, which starts on the east (left) side of the scenario, with the goal plotted as a dashed black circle on the west (right) side of the scenario. Recall that RTD is not tested in Experiment 1, but the same scenarios are used in all three experiments, making this comparison possible. The Segway’s pose is plotted in blue every 1.5 s, or less frequently when the Segway is stopped or spinning in place. For RTD, contours of the FRS (i.e. the set $\pi_x^l(k_{opt})$ from (77)) are plotted in green. The actual (non-buffered) obstacles for all three planners are plotted as solid red boxes. For RTD, the discretized obstacle is plotted as the red points around each box; this is a buffer size of 0.07 m. For RRT and NMPC, the buffered obstacles are plotted as tan lines around each box; this is a buffer size of 0.45 m. Row 1 (Subfigures (a), (b), and (c)) shows a scenario where all three planners are successful. Row 2 shows a scenario where RTD is successful, but RRT and NMPC are not. Subfigure (d) shows RTD reaching the goal. Subfigure (e) shows RRT attempting to navigate a gap between several obstacles, where it is unable to find a new plan; it crashes when it tries to brake along its previously-planned trajectory. Subfigure (f) shows NMPC braking because it cannot compute a safe plan to navigate the same gap where RRT crashed; here, NMPC happens to brake safely and gets stuck because it cannot find a new plan fast enough. Row 3 shows a scenario where RTD stops safely, but fails to reach the goal, whereas RRT and NMPC do reach the goal. Subfigure (g) shows that RTD initially turns north more sharply than RRT or NMPC, which forces it to brake safely; it then finds a safe path south, which causes the high-level A* planner to reroute it even farther south to where there is no feasible solution, causing RTD to get stuck because the southern route is considered feasible by the A* planner. Subfigures (h) and (i) show RRT and NMPC reaching the goal because they do not turn north as sharply initially, so the A* planner is able to route them north and around the obstacles.

Rover Experiment 1		RRT [23, 36, 39]		NMPC [38]	
		Goals	Crashes	Goals	Crashes
Buffer [m]	0.15	74.8	25.2	96.6	0.5
	0.25	97.4	2.2	96.7	0.0
	0.35	95.7	2.4	95.2	0.0

Table 3: Comparison of success and crash rates for varying buffer sizes for the Rover. A buffer size of 0.25 m provides the best balance of performance and safety for both planners.

9.3.2 Experiment 2: Real-time Planning and Limited Sensor Horizon

The goal for Experiment 2 is to understand the performance of RTD, RRT, and NMPC when subject to real-time and limited sensor horizon requirements. RTD is designed to satisfy these requirements while provably ensuring safety. RRTs are typically capable of rapid planning, though not necessarily with arbitrary dynamics [6, 23]. For NMPC, these requirements can cause wide variations in performance depending on how constraints are represented [10, 12, 38].

The parameters used for Experiment 2 are as follows. For the Segway, $\tau_{\text{move}} = \tau_{\text{plan}} = 0.5$ s and $D_{\text{sense}} = 4.0$ m. For the Rover, $\tau_{\text{move}} = \tau_{\text{plan}} = 0.375$ s, and $D_{\text{sense}} = 3.5$ m. Since $\tau_{\text{move}} = \tau_{\text{plan}}$, the amount of time allowed for planning is the same as the amount of time that each robot executes from the previously-planned trajectory, meaning the real-time requirement is enforced. Since D_{sense} is smaller than the size of each robot’s scenario (see Section 9.1), the limited sensor horizon requirement is enforced. For the Segway, the RRT and NMPC buffer size is 0.45 m; the RTD obstacle buffer size is 0.07 m. Note that, since the Segway’s radius is 0.38 m, this means that RTD has the same amount of free space available for planning as RRT and NMPC. For the Rover, the RTD obstacle buffer size is 0.01 m; the RRT and NMPC buffer size is 0.25 m. Since the Rover’s RTD planner uses an expanded rectangular footprint as discussed in Example 19, whereas RRT and NMPC track the Rover’s center of mass, there is no way to directly compare the buffer sizes. So, for RTD, we pick $0.01 \in (0, \bar{b})$ to ensure safety, where $\bar{b} = 0.28$ m as discussed in Section 8.2.

We expect the results of Experiment 2 to be as follows. For both robots, we expect RTD to have a similar number of goals reached as RRT and NMPC, and we expect RRT and NMPC to reach the goal less often than in Experiment 1. This is due to the limited sensor horizon, meaning the high-level planner no longer has access to the entire scenario at time 0, and therefore may make poor routing decisions. As for crashes, RTD is designed with real-time performance as a requirement, and prescribes a minimum sensor horizon in Theorem 35 that is less than D_{sense} for both robots. Therefore, we expect RTD to have no crashes. We expect RRT and NMPC to have slightly more crashes than in Experiment 1, because the sensor horizon is shorter, and because the real-time requirement means that these two planners may be unable to find feasible plans as often, resulting in both planners braking more frequently.

The results of Experiment 2 are summarized in Table 4 for the Segway and Table 5 for the Rover. For the Segway, RTD reaches the goal more often than the other two planners do in Experiment 1 or in Experiment 2 (87.4%); recall that the same scenarios are used in all three experiments, making this comparison possible. RRT surprisingly reaches the goal slightly more often in Experiment 2 than in Experiment 1 (77.2% vs. 75.2%); and NMPC is incapable of reaching the goal (0% vs. 83.7%). RTD has no crashes, as expected; RRT crashes less often (6.3% vs. 11.7%); and NMPC does not crash because it struggles to move the robot at all. For the Rover, RTD reaches the goal 93.1% of the time. RRT reaches the goal slightly less often than in Experiment 1 (97.4% vs. 97.8%); and NMPC is incapable of reaching the goal (0% vs. 97.6%). RTD has no crashes; RRT crashes more often (2.1% vs. 1.9%); and NMPC again does not crash because it struggles to move the robot.

We now discuss the results of Experiment 2. For both the Segway and Rover, RTD’s performance is as expected based on the theory in this paper: it is able to reach the goal, can plan in real time, and has no crashes. The Segway’s RRT has a slight increase in goals and reduction in crashes, which is surprising, but this makes sense because the real-time requirement means that RRT is less likely to find a plan at every iteration, and must brake more often. So, the Segway’s RRT travels through each scenario in short bursts, and takes advantage of the fact that the Segway is able to spin in place after braking. For the Segway’s NMPC planner, we notice that GPOPS-II is able to find trajectories rapidly when the vehicle is not near obstacles; but, since the obstacles are randomly-placed and produce non-convex constraints, the solver struggles to solve quickly when near them, resulting in 0 goals and 0 crashes. The Rover’s RRT planner reaches the goal slightly less often, and crashes slightly more often, as expected by the shortened sensor horizon; unlike the Segway, the Rover cannot spin in place to potentially find a new plan after braking. The Rover’s NMPC planner suffers the same issues near the obstacle constraints as the Segway’s NMPC planner.

Figure 15 demonstrates Experiments 1 and 2 for the Segway; the RRT and NMPC plots are from Experiment 1, and the RTD plots are from Experiment 2, since RTD is not run in Experiment 1. The same randomly-generated scenarios are used in all experiments, so this direct comparison is possible. The figure shows one scenario where RTD, RRT, and NMPC all reach the goal without crashing; one scenario where RTD reaches the goal, RRT crashes, and NMPC gets stuck; and one scenario where RTD brakes safely whereas RRT and NMPC reach the goal. In the second scenario, RRT crashes because, while trying to navigate a gap between two obstacles, it is unable to find a feasible plan; it then attempts to brake along its previous trajectory, but touches an obstacle while doing so, because the Segway cannot necessarily brake exactly along its previous plan produced by RRT. NMPC gets stuck trying to navigate this same gap where RRT crashes, because the gap is a non-convex region with enough obstacle constraints that the NMPC planner computes slowly. Unlike RRT, NMPC brakes much earlier, which happens to be safe, but then is unable to find a plan to navigate the gap. In the third scenario, RTD gets stuck because, early on, it finds a different path from RRT and NMPC; this new path causes the high-level A* planner to reroute RTD towards a region where A* believes that the route is feasible, but RTD does not, resulting in RTD braking safely. This demonstrates that, even if the high-level planner makes infeasible decisions, RTD is safe.

Figure 16 demonstrates Experiment 2 for the Rover with one scenario where RTD succeeds, RRT crashes, and NMPC gets stuck; and one scenario where RTD brakes safely, RRT crashes, and NMPC gets stuck. In both scenarios, RRT crashes when it travels too close to an obstacle to find a plan at the next planning iteration, causing it to try to brake; it is unable to brake exactly along the previously-found trajectories, resulting in a crash. In both scenarios, NMPC is able to find plans until the obstacles appear in its sensor horizon; since real-time planning is enforced in Experiment 2, NMPC is unable to find a plan quickly as soon as it sees an obstacle, causing it to brake. It brakes without crashing because it is farther than its braking distance from the obstacles when it senses them.

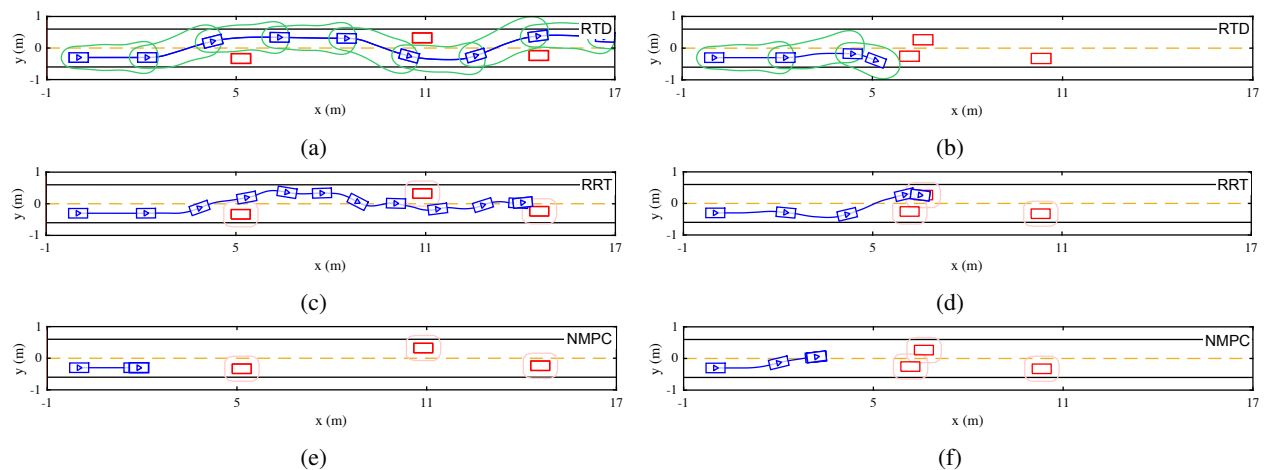


Figure 16: Two sample scenarios from Experiment 2 for the Rover. The Rover’s trajectory and pose (every 1.125 s) are plotted in blue. Obstacles are plotted in red. Buffered obstacles for RRT and NMPC are plotted in beige. Subfigures (a) and (b) show RTD avoiding the obstacles. The subset of the FRS associated with the optimal parameter every 1.25 s is plotted in green. Subfigures (c) and (d) show the RRT method. In Subfigure (c), RRT is unable to find a path around the third obstacle. In Subfigure (d), RRT is unable to come to a stop before it collides with the second obstacle. Subfigures (e) and (f) show NMPC, which stops due to enforcement of real-time planning limits.

9.3.3 Experiment 3: Real Planning Time and Minimal Sensor Horizon

The goal for Experiment 3 is to confirm that RTD performs safe, real-time trajectory planning even when the sensor horizon is the minimum possible as per Theorem 35. This is useful because, to be practical, RTD must be able to tolerate environments where a robot’s sensors are only effective in a small area.

The parameters used for Experiment 3 are as follows. For the Segway, $\tau_{\text{move}} = \tau_{\text{plan}} = 0.5$ s and $D_{\text{sense}} = 1.875$ m. For the Rover, $\tau_{\text{move}} = \tau_{\text{plan}} = 0.375$ s and $D_{\text{sense}} = 2$ m. Since $\tau_{\text{move}} = \tau_{\text{plan}}$, the real-time planning requirement is enforced, as in Experiment 2. The sensor horizon D_{sense} is given by Theorem 35. For the Segway, the buffer size used is 0.07 m, as in Section 8.1. For the Rover, the buffer size is 0.01 m.

We expect the results of Experiment 3 to show that RTD has zero crashes for either robot. We expect the number of goals reached to drop compared to Experiment 2, because a smaller sensor horizon means that the high-level planner for both robots has less information when making routing decisions. So, it is more likely that the high-level planners cause both robots to brake safely without reaching the goal.

The results of Experiment 3 confirm the expectation. Both robots have 0 crashes. The Segway reaches the goal 76.4% of the time, versus 88.4% in Experiment 2. The Rover reaches the goal 52.9% of the time, versus 93.1% in Experiment 2.

We now discuss the results of Experiment 3. Neither robot has any crashes with the minimal sensor horizon. Both robots reach the goal much less frequently, because the high-level planner often does not have enough information to make feasible global plans. But, RTD guarantees locally safe behavior regardless of global planner optimality.

9.4 Discussion

The experiments show that RTD is successful in reaching the desired goal comparably often to RRT and NMPC for both the Segway and Rover. Importantly, RTD has 0 crashes in all of the simulations.

RRT crashes because its paths may take it near obstacles, where it is difficult to build a dense tree since most nodes are infeasible. When this happens, RRT attempts to brake along its previously-planned trajectory, but there is no guarantee that this can be done safely. Interestingly, for the Segway, reducing the allowed planning time τ_{plan} reduces the crash rate. This is because RRT cannot find a feasible plan as frequently with the lower planning time, so it brakes more often, and begins braking further away from obstacles. Since the Segway rotates in place after braking, the RRT has more opportunities to find feasible paths.

NMPC crashes because, when the robot is near an obstacle, there are a large number of non-convex constraints in the resulting optimization program, so finding a feasible solution within the planning time cutoff of τ_{plan} is difficult. If no plan is found, the robot attempts to brake along its previous trajectory, but the algorithm has no guarantee that doing so is safe. Recall that, for RTD, we require the robot to be able to brake within the FRS corresponding to its parameterized trajectories (Assumption 32). By contrast, NMPC produces arbitrary trajectories, so it cannot make the same braking assumption.

We found that increasing the buffer size (Experiment 1) reduces the number of crashes for both RRT and NMPC for both robots, as expected. The tradeoff for buffer size is that a larger buffer reduces the free space available for the robot to move through, reducing how often each robot reaches the goal. Importantly, crashes occur for both planners even when they are not required to plan in real-time or with a limited sensor horizon. In other words, RRT and NMPC are shown to not be persistently feasible, confirming that persistent feasibility must be considered for robots operating with receding horizon trajectory planners.

RTD is sometimes unable to reach the goal, but still always brakes safely. Note that RRT and NMPC on both the Segway and Rover platforms are sometimes also unable to reach the goal. For the Segway, stopping safely before reaching the goal occurs when RTD plans a path too close to an obstacle, in which case the online optimization OptK struggles to find a non-stopped solution even after spinning the Segway in place. This may be remedied by changing the global A* planner to penalize obstacles more, or by changing the cost function in the online optimization. The Rover stops without reaching the goal when the expanded footprint (which captures the robot's rotations) is too large to make a lane change through a tight gap between two obstacles. This may be remedied by representing X_0 as the true footprint of the vehicle and then capturing the spatial effects of rotation in g_x and g_y .

Overall, the simulation experiments confirm that RTD is safe and persistently feasible. See Figures 15 and 16 for examples of RTD performing trajectory planning for the Segway and Rover platforms.

10 Hardware Demonstration

This section details the application of RTD to the Segway (Figure 2a) and Rover (Figure 2b) hardware platforms. Section 9 confirms that RTD is safe and persistently feasible, so it is able to plan safe trajectories in real time. The hardware demonstrations confirm this as well. Videos of the robots are available at <https://youtu.be/FJns7YpdMXQ> for the Segway and https://youtu.be/bgDEAi_Ewfw for the Rover.

Segway Simulation Results					
Experiment	τ_{plan} [s]	D_{sense} [m]	Planner	Goals [%]	Crashes [%]
1 (0.45 m buffer)	10.0	100	RRT	75.2	11.7
			NMPC	83.7	0.5
2	0.5	4.0	RTD	87.4	0.0
			RRT	77.2	6.3
			NMPC	0.0	0.0
3	0.5	1.5	RTD	76.4	0.0

Table 4: Simulation results of Experiments 1–3 for the Segway. RTD is the only method that never experiences crashes, as expected; it also reaches the goal more frequently than RRT or NMPC. RRT improves in goals and crashes when forced to plan in real time because it brakes more often, so it leverages the Segway’s capability to rotate in place more frequently. NMPC reaches the goal comparably often to RTD and RRT, with fewer crashes than RRT, but is unable to plan in real time (Experiment 2). In Experiment 3, RTD is capable of planning safely, but is more conservative in terms of goals reached than in Experiment 2, when given the smallest possible sensor horizon allowed for persistent feasibility by Theorem 35.

Rover Simulation Results					
Experiment	τ_{plan} [s]	D_{sense} [m]	Planner	Goals [%]	Crashes [%]
1 (0.25 m buffer)	10.0	50	RRT	97.8	1.9
			NMPC	97.6	0.0
2	0.375	3.5	RTD	93.1	0.0
			RRT	97.4	2.1
			NMPC	0.0	0.0
3	0.375	2.75	RTD	52.9	0.0

Table 5: Simulation results of Experiments 1–3 for the Rover. RTD is the only method that can both reach the goal and never crash when real time planning is enforced. However, it reaches the goal less frequently than RRT or NMPC in Experiment 2, because the RTD robot footprint introduces conservatism that RRT and NMPC do not experience. RRT has approximately the same number of goals reached in all experiments where it is tested; its number of crashes reduces slightly when a minimum planning time horizon is enforced, as expected. NMPC has comparably many goals reached to RRT, and fewer crashes because it frequently is unable to find a feasible plan within τ_{plan} s, causing it to brake when near obstacles. In addition, NMPC is unable to plan in real time. In Experiment 3, RTD is capable of planning safely, but more conservative in terms of goals reached compared to Experiment 2, when given the smallest possible sensor horizon allowed for persistent feasibility by Theorem 35.

10.1 Segway

The first hardware demo uses the Segway Robotics Mobility Platform shown in Figure 2a. Sensing is performed with a Hokuyo UTM-30LX planar lidar; in practice, we found this sensor to be accurate up to $D_{\text{sense}} = 4.0$ m away (recall that the Segway runs indoors, so the effective sensor horizon is small). The robot is controlled by a 4.0 GHz laptop with 64 GB of memory, running MATLAB and the Robot Operating System (ROS). Google Cartographer is used for localization and mapping [18]. All computation is run onboard. Since SLAM and state estimation requires $\tau_{\text{process}} = 0.2$ s per iteration (as in Assumption 26), we enforce $\tau_{\text{trajopt}} = 0.3$ s when calling `OptK` (as in Algorithm 2 from Section 7). We find in practice that the state estimation error is never more than 0.1 m in the global xy -coordinate frame while the Segway tracks any parameterized trajectory, so we set $\varepsilon_x = \varepsilon_y = 0.1$ m as in Assumption 9. The FRS is computed for the Segway as described in Section 8.1.

The Segway is run on a 4×8 m² tile floor with 30 cm cubical obstacles randomly distributed just before run time. The Segway has no prior knowledge of the obstacles. Two points are picked on opposite ends of the room and used as the start and goal points in an alternating fashion.

A supplementary video illustrates the performance of RTD. randomly-placed obstacles, the Segway RMP platform is able to operate safely while consistently reaching its goal. As in the simulation, the Segway uses a low speed and a high speed FRS (see Section 8.1.2). In the handful of instances where the Segway brakes, the A* algorithm generates waypoints that require passing through a gap that is too small for the high speed FRS; the Segway swaps to the low speed FRS after stopping, and is then able to navigate the gap.

10.2 Rover

The second hardware demo uses a Rover car-like robot based on a Traxxas RC platform. The Rover is tested on a 7 m long mock road, which is a tiled surface, as shown in Figure 2b. This setup resembles the simulation environment, but with a shorter road and smaller obstacles. The Rover is equipped with a front-mounted Hokuyo UST-10LX planar lidar for sensing and localization; as the Rover runs indoors, we found this sensor to be accurate up to at least $D_{\text{sense}} = 3.5$ m away given occlusions and obstacle density. An NVIDIA TX-1 computer on-board is used to run the sensor drivers, state estimator, feedback controller, and low-level motor controller. The Rover uses ROS to communicate with an Intel Core i7 7820HK (2.90 GHz) CPU/64 GB RAM laptop over wifi. The laptop is used for localization and mapping, to capture experiment data, and to run the function OptK from Algorithm 2. We use $\varepsilon_x = \varepsilon_y = 0.1$ m for the state estimation error as in Assumption 27. The FRS is computed for the Rover as described in Section 8.2.

For each trial, the Rover is placed at one end of the mock road and instructed to drive to a goal at the other end at speeds of 1–1.5 m/s. One to three obstacles are placed between the Rover and the goal. The obstacles are $0.3 \times 0.3 \times 0.3$ m³ cardboard cubes. The Rover is not given prior knowledge of the obstacles for each trial, and uses its planar LIDAR to detect them in real-time. The Rover has an enforced planning time limit of $\tau_{\text{trajopt}} + \tau_{\text{process}} = 0.375$ s. Contrary to the Segway, the timeouts were enforced together. This is because localization and map updates were provided smoothly at 20 Hz, so the algorithm did not need to pause and wait for an update as often as the Segway did. Eight trials were run back-to-back and filmed in one take, as presented in the supplementary video. Several types of scenarios are constructed to encourage the Rover to change lanes or force it to brake to a stop. Eighteen trials were run in addition to the filmed trials, and resulted in zero crashes. The FRS described in Section 8.2 is used, with the Rover’s speed at 1.0–1.5 m/s. Due to the minimum speed, the Rover is occasionally unable to navigate tight gaps; this could be remedied by using a low speed FRS as the Segway does.

11 Conclusion

This paper presents the Reachability-based Trajectory Design (RTD) method, which plans provably safe trajectories in real time. Other state-of-the-art methods for planning rely on spatial or temporal discretization and rely on heuristics to manage tradeoffs between accuracy and run time to simultaneously enable safety and real-time performance. With RTD, the robot plans using a continuous set of parameterized trajectories. The Forward Reachable Set (FRS), computed offline, contains reachable positions of the robot, including tracking error, when tracking these trajectories over a fixed time horizon. Criteria for the robot’s sensor horizon and stopping distance ensure that the robot is always able to find a safe trajectory or stopping path.

RTD operates in a planning loop; in each iteration, a nonlinear optimization program is solved to select optimal trajectory parameters. The FRS is used to create a map that sends obstacles from the state space to the parameter space as nonlinear constraints for the online solver in a provably safe way, ensuring that any trajectory selected to satisfy the constraints cannot cause a collision. This paper presents a provably safe method for representing arbitrary obstacles with a discrete set of points. This representation allows the online optimization program to solve in real-time. This paper also adapts a system decomposition technique for computing the FRS, extending the application of RTD to higher dimensional systems.

RTD is applied to two systems in both simulation and hardware: a Segway RMP robot navigating a room full of random obstacles, and a car-like Rover robot performing lane change maneuvers on a mock two lane road. The Segway’s parameterized trajectories are Dubins paths with varying velocities and yaw rates. Using a high-level A* planner to produce a coarse route, the Segway is able to safely traverse the room despite random, unforeseen obstacle configurations. The Rover’s FRS computation uses the presented system decomposition method. The Rover’s parameterized trajectories are lane change maneuvers generated with a bicycle model. A high-level planner tells the Rover to change lanes if an obstacle is sensed nearby in the same lane. RTD then synthesizes either a safe lane change or safe braking maneuver. Simulation results for both the Segway and Rover compare the performance and safety of RTD to Rapidly-exploring Random Tree (RRT) and Nonlinear Model-Predictive Control (NMPC) methods. When real-time planning limits are enforced, RTD is able to outperform RRT and NMPC in terms of number of goals reached without causing any crashes. Videos of the hardware demonstrations are available at <https://www.youtube.com/watch?v=FJns7YpdMXQ> for the Segway and https://www.youtube.com/watch?v=bgDEAi_Ewfw for the Rover. Although this paper only applies to 2-D ground vehicles, the theory can also be generalized to 3-D systems.

Future work will extend RTD to dynamic environments and more complex uncertainty models. We are also exploring nonlinear solvers that can find globally-optimal solutions in finite time for the online portion of RTD, because the current method is limited by off-the-shelf nonlinear solvers without global optimality guarantees.

References

- [1] Ahnert, K. and Mulansky, M. (2011). Odeint - solving ordinary differential equations in C++. *CoRR*, abs/1110.3397.
- [2] Buehler, M., Iagnemma, K., and Singh, S. (2009). *The DARPA urban challenge: autonomous vehicles in city traffic*, volume 56. springer.
- [3] Chen, M., Herbert, S., and Tomlin, C. J. (2016). Exact and efficient hamilton-jacobi-based guaranteed safety analysis via system decomposition. *arXiv preprint arXiv:1609.05248*.
- [4] Chen, M., Herbert, S. L., Vashishtha, M. S., Bansal, S., and Tomlin, C. J. (2016). Decomposition of Reachable Sets and Tubes for a Class of Nonlinear Systems. *ArXiv e-prints*.
- [5] Ding, J., Li, E., Huang, H., and Tomlin, C. J. (2011). Reachability-based synthesis of feedback policies for motion planning under bounded disturbances. In *Robotics and Automation (ICRA), 2011 IEEE International Conference on*, pages 2160–2165. IEEE.
- [6] Elbanhawi, M. and Simic, M. (2014). Sampling-based robot motion planning: A review. *IEEE Access*, 2:56–77.
- [7] Falcone, P., Borrelli, F., Asgari, J., Tseng, H., and Hrovat, D. (2008). Low complexity mpc schemes for integrated vehicle dynamics control problems. In *9th international symposium on advanced vehicle control*.
- [8] Falcone, P., Borrelli, F., Asgari, J., Tseng, H. E., and Hrovat, D. (2007). Predictive active steering control for autonomous vehicle systems. *IEEE Transactions on control systems technology*, 15(3):566–580.
- [9] Fogel, E., Halperin, D., and Wein, R. (2012). *Minkowski Sums and Offset Polygons*, pages 209–240. Springer Berlin Heidelberg, Berlin, Heidelberg.
- [10] Frasch, J. V., Gray, A., Zanon, M., Ferreau, H. J., Sager, S., Borrelli, F., and Diehl, M. (2013). An auto-generated nonlinear mpc algorithm for real-time obstacle avoidance of ground vehicles. In *2013 European Control Conference (ECC)*, pages 4136–4141.
- [11] Freeman, H. and Shapira, R. (1975). Determining the minimum-area encasing rectangle for an arbitrary closed curve. *Commun. ACM*, 18(7):409–413.
- [12] Gao, Y., Gray, A., Carvalho, A., Tseng, H. E., and Borrelli, F. (2014a). Robust nonlinear predictive control for semiautonomous ground vehicles. In *2014 American Control Conference*, pages 4913–4918.
- [13] Gao, Y., Gray, A., Tseng, H. E., and Borrelli, F. (2014b). A tube-based robust nonlinear predictive control approach to semiautonomous ground vehicles. *Vehicle System Dynamics*, 52(6):802–823.
- [14] Gill, P. E., Murray, W., and Saunders, M. A. (2002). Snopt: An sqp algorithm for large-scale constrained optimization.
- [15] González, D., Pérez, J., Milanés, V., and Nashashibi, F. (2016). A review of motion planning techniques for automated vehicles. *IEEE Transactions on Intelligent Transportation Systems*, 17(4):1135–1145.
- [16] Gray, A., Gao, Y., Lin, T., Hedrick, J. K., Tseng, H. E., and Borrelli, F. (2012). Predictive control for agile semi-autonomous ground vehicles using motion primitives. In *American Control Conference (ACC), 2012*, pages 4239–4244. IEEE.
- [17] Herbert*, S. L., Chen*, M., Han, S., Bansal, S., Fisac, J. F., and Tomlin, C. J. (2017). Fastrack: a modular framework for fast and guaranteed safe motion planning. *IEEE Conference on Decision and Control (submitted)*.

- [18] Hess, W., Kohler, D., Rapp, H., and Andor, D. (2016). Real-time loop closure in 2d lidar slam. In *2016 IEEE International Conference on Robotics and Automation (ICRA)*, pages 1271–1278.
- [19] Janson, L., Schmerling, E., Clark, A., and Pavone, M. (2015). Fast marching tree: A fast marching sampling-based method for optimal motion planning in many dimensions. *The International journal of robotics research*, 34(7):883–921.
- [20] Johnson-Roberson, M., Barto, C., Mehta, R., Sridhar, S. N., and Vasudevan, R. (2016). Driving in the matrix: Can virtual worlds replace human-generated annotations for real world tasks? *arXiv preprint arXiv:1610.01983*.
- [21] Karaman, S. and Frazzoli, E. (2011). Sampling-based algorithms for optimal motion planning. *The international journal of robotics research*, 30(7):846–894.
- [22] Kousik, S., Vaskov, S., Johnson-Roberson, M., and Vasudevan, R. (2017). Safe trajectory synthesis for autonomous driving in unforeseen environments. In *ASME 2017 Dynamic Systems and Control Conference*, pages V001T44A005–V001T44A005. American Society of Mechanical Engineers.
- [23] Kuwata, Y., Teo, J., Fiore, G., Karaman, S., Frazzoli, E., and How, J. P. (2009). Real-time motion planning with applications to autonomous urban driving. *IEEE Transactions on Control Systems Technology*, 17(5):1105–1118.
- [24] Lasserre, J. B. (2009). *Moments, positive polynomials and their applications*, volume 1. World Scientific.
- [25] LaValle, S. M. and Kuffner Jr, J. J. (2001). Randomized kinodynamic planning. *The International Journal of Robotics Research*, 20(5):378–400.
- [26] Liniger, A. and Lygeros, J. (2017). Real-time control for autonomous racing based on viability theory. *arXiv preprint arXiv:1701.08735*.
- [27] Liu, W., Anguelov, D., Erhan, D., Szegedy, C., Reed, S., Fu, C.-Y., and Berg, A. C. (2016). Ssd: Single shot multibox detector. In *European Conference on Computer Vision*, pages 21–37. Springer.
- [28] Luders, B., Kothari, M., and How, J. (2010). Chance constrained rrt for probabilistic robustness to environmental uncertainty. 0.
- [29] Majumdar, A. and Tedrake, R. (2016). Funnel libraries for real-time robust feedback motion planning. *arXiv preprint arXiv:1601.04037*.
- [30] Majumdar, A., Vasudevan, R., Tobenkin, M. M., and Tedrake, R. (2014). Convex optimization of nonlinear feedback controllers via occupation measures. *The International Journal of Robotics Research*, 33(9):1209–1230.
- [31] Mosek ApS (2010). The mosek optimization software. *Online at <http://www.mosek.com>*, 54(2-1):5.
- [32] Munkres, J. (2000). *Topology (2nd Edition)*. Pearson, 2 edition.
- [33] Nagurnas, S., Mituneviius, V., Unarski, J., and Wach, W. (2007). Evaluation of veracity of car braking parameters used for the analysis of road accidents. *Transport*, 22(4):307–311.
- [34] Nocedal, J. and Wright, S. (2006). *Numerical Optimization*. Springer Series in Operations Research and Financial Engineering. Springer New York.
- [35] Orosz, G., Zhang, Y., Qin, W. B., He, C. R., and Avedisov, S. S. (2017). Nonholonomic lane change maneuvers for connected and autonomous vehicles.
- [36] Palmieri, L., Koenig, S., and Arras, K. O. (2016). Rrt-based nonholonomic motion planning using any-angle path biasing. In *2016 IEEE International Conference on Robotics and Automation (ICRA)*, pages 2775–2781.
- [37] Parrilo, P. A. (2000). *Structured semidefinite programs and semialgebraic geometry methods in robustness and optimization*. PhD thesis, California Institute of Technology.
- [38] Patterson, M. A. and Rao, A. V. (2014). Gpops-ii: A matlab software for solving multiple-phase optimal control problems using hp-adaptive gaussian quadrature collocation methods and sparse nonlinear programming. *ACM Trans. Math. Softw.*, 41(1):1–1:37.

- [39] Pepy, R., Lambert, A., and Mounier, H. (2006). Path planning using a dynamic vehicle model. In *2006 2nd International Conference on Information Communication Technologies*, volume 1, pages 781–786.
- [40] Rajamani, R. (2011). *Vehicle dynamics and control*. Springer Science & Business Media.
- [41] Rudin, W. (1976). *Principles of Mathematical Analysis*. International series in pure and applied mathematics. McGraw-Hill.
- [42] Strang, G. (1982). The width of a chair. *The American Mathematical Monthly*, 89(8):529–534.
- [43] Tobenkin, M. M., Permenter, F., and Megretski, A. (2013). Spotless polynomial and conic optimization.
- [44] Vandiver, J. and Gossard, D. (2011). 2.003sc engineering dynamics. <https://ocw.mit.edu/courses/mechanical-engineering/2-003sc-engineering-dynamics-fall-2011/>. Accessed: 2018-08-20.

12 Appendix: Conditions for Persistent Feasibility

In this appendix, we provide conditions to ensure that, at any speed, the robot’s non-braking trajectory (49) is spatially longer than the corresponding braking trajectory, i.e. the robot achieves a larger displacement in X when not braking as opposed to braking. This is because, if we know that a non-braking trajectory is safe over its entire distance, then the robot can stop safely in its direction of travel, i.e. longitudinally. We find a minimum planning time horizon that guarantees this with Remark 73. Then, to ensure safety, we assume the robot is able to stop within its FRS as discussed in Section 5. Here, we are only concerned with the robot’s longitudinal braking behavior.

We begin by defining the braking trajectory with controller u_{brake} from (50):

$$\zeta_{\text{brake}}(t; \zeta_{\text{hi},0}, k) = \zeta_{\text{hi},0} + \int_0^{\tau_{\text{plan}} + \tau_{\text{brake}}(\zeta_{\text{hi},0}, k)} f_{\text{hi}}(\tau, \zeta_{\text{brake}}(\tau), u_{\text{brake}}(\tau)) d\tau. \quad (83)$$

Recall that, by Assumption 30, for every $\zeta_{\text{hi},0}$ and k , there exists a finite braking distance $D_{\text{brake}} : Z_{\text{hi},0} \times K \rightarrow \mathbb{R}_{\geq 0}$ given by

$$D_{\text{brake}}(\zeta_{\text{hi},0}, k) = \int_{\tau_{\text{plan}}}^{\tau_{\text{plan}} + \tau_{\text{brake}}(\zeta_{\text{hi},0}, k)} \left\| \text{proj}_X(f_{\text{hi}}(\tau, \zeta_{\text{brake}}(\tau), u_{\text{brake}}(\tau))) \right\|_2 d\tau, \quad (84)$$

which follows from the formula for length along a differentiable parametric curve [41, Theorem 6.27]. So, the quantity $D_{\text{brake}}(\zeta_{\text{hi},0}, k)$ is the robot’s total distance traveled over the braking portion of the braking trajectory (83). Recall that the robot begins braking at $t = \tau_{\text{plan}}$ while tracking k from initial condition $\zeta_{\text{hi},0}$. Since $Z_{\text{hi},0}$ and K are compact, there exists a maximum braking distance:

$$D_{\text{stop}} = \max_{\zeta_{\text{hi},0} \in Z_{\text{hi},0}, k \in K} D_{\text{brake}}(\zeta_{\text{hi},0}, k). \quad (85)$$

Recall from Assumption 6 that the robot’s high-fidelity model (1) has a state that tracks its speed in the subspace X , and a max speed v_{max} . Let $D_{\text{brake,max}} : [0, v_{\text{max}}] \rightarrow \mathbb{R}_{\geq 0}$ be the maximum braking distance at a particular speed:

$$D_{\text{brake,max}}(v) = \sup_{\zeta_{\text{hi},0} \in Z_{\text{hi},0}, k \in K} \{D_{\text{brake}}(\zeta_{\text{hi},0}, k) \mid \text{proj}_V(\zeta_{\text{hi},0}) = v\}, \quad (86)$$

where proj_V returns the value of speed state in $\zeta_{\text{hi},0}$. The maximum is achieved for each v because proj_V is continuous (see Definition 8), so the preimage $\text{proj}_V^{-1}(\{v\})$ is a closed subset of $Z_{\text{hi},0}$, and therefore compact [32, Theorem 26.2]. We now relate $D_{\text{brake,max}}$ to the vehicle speed to formalize the idea that, as the robot travels faster, its maximum braking distance increases.

Assumption 71. *The maximum braking distance at any speed is upper bounded by a linear function of speed:*

$$D_{\text{brake,max}}(v) \leq \left(\frac{D_{\text{stop}}}{v_{\text{max}}} \right) v. \quad (87)$$

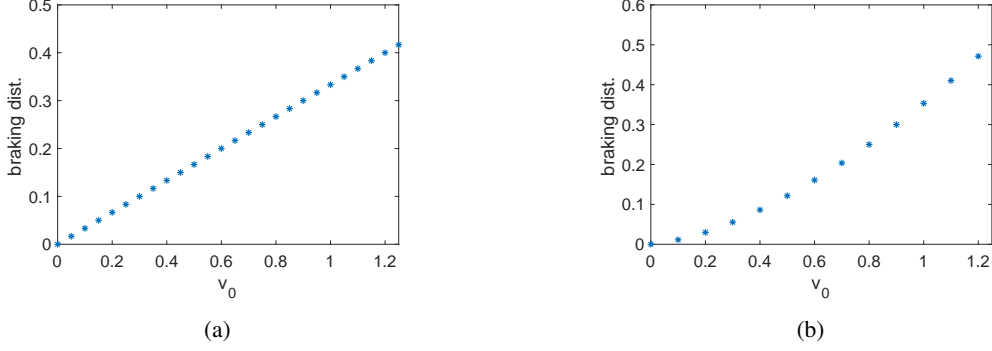


Figure 17: Braking distance of the Segway is shown in Figure 17a, and of the Rover in Figure 17b versus initial speed v_0 . Notice that both robots have a braking distance which is upper bounded by a linear function of speed as in Assumption 71.

Assumption 71 implies that the maximum stopping distance at speed $v = 0$ (resp. v_{\max}) is 0 (resp. D_{stop}). To see why $D_{\text{brake,max}}$ can be upper-bounded by a linear function of speed, consider the following example. For automobiles, the maximum braking distance is proportional to the kinetic energy of the vehicle, which is proportional to the square of the vehicle's speed [33]. Let $D_{\text{quad}} : [0, v_{\max}] \rightarrow \mathbb{R}_{\geq 0}$ be the braking distance of this quadratic relationship. We assume the relationship between braking distance and kinetic energy also holds for any ground robot. Since v_{\max} is fixed by Assumption 6, the relationship satisfies (87):

$$D_{\text{quad}}(v) = \left(\frac{D_{\text{stop}}}{v_{\max}^2} \right) v^2 \leq \left(\frac{D_{\text{stop}}}{v_{\max}} \right) v \quad \forall v \in [0, v_{\max}], \quad (88)$$

where the coefficient of the quadratic term ensures that D_{stop} is the braking distance at v_{\max} . Figure 17 shows that this relationship holds for the Segway and Rover robots described in Section 8.

We use Assumption 71 to find the amount of time, τ_v , for the robot to travel the distance $D_{\text{brake,max}}(v)$ at speed v :

$$\tau_v = \max_{v \in (0, v_{\max}] \left(\frac{D_{\text{brake,max}}(v)}{v} \right) = \frac{D_{\text{stop}}}{v_{\max}}, \quad (89)$$

where the maximum occurs at $v = v_{\max}$ by Assumption 71.

Assumption 72. Suppose the robot, described by high-fidelity dynamics 1, is at an arbitrary initial condition $\zeta_{\text{hi},0}$, with initial speed $\text{proj}_V(\zeta_{\text{hi},0}) = v \in (0, v_{\max}]$, and is tracking an arbitrary $k \in K$. Let the non-braking trajectory be as in (49) and the braking trajectory be as in (83). Then the distance that the robot travels along the non-braking trajectory over the duration $\tau_{\text{plan}} + \tau_v$ is greater than or equal to the total distance it travels along the braking trajectory:

$$\left(\int_{\tau_{\text{plan}}}^{\tau_{\text{plan}} + \tau_{\text{brake}}(\zeta_{\text{hi},0,k})} \left\| \text{proj}_X(f_{\text{hi}}(\tau, \zeta_{\text{brake}}, u_{\text{brake}})) \right\|_2 d\tau \right) \leq \left(\int_{\tau_{\text{plan}}}^{\tau_{\text{plan}} + \tau_v} \left\| \text{proj}_X(f_{\text{hi}}(\tau, \zeta_{\text{hi}}, u_k)) \right\|_2 d\tau \right), \quad (90)$$

where we are again using the arclength formula as in (84), and the arguments to $\zeta_{\text{brake}}, u_{\text{brake}}, \zeta_{\text{hi}}$, and u_k have been dropped for ease of notation.

Note that, over the time horizon $[0, \tau_{\text{plan}}]$, the braking and non-braking trajectories are identical, which is why we only consider $t \geq \tau_{\text{plan}}$. To understand Assumption 72, consider the case where the non-braking controller u_k maintains a fixed speed v . Then, from (87) and (89), we have that the braking distance is less than the non-braking distance traveled:

$$D_{\text{brake,max}}(v) \leq \frac{D_{\text{stop}}}{v_{\max}} = \tau_v \cdot v. \quad (91)$$

The only case where Assumption 72 would not hold is if the controller u_k causes the vehicle to brake from a speed $v \in (0, v_{\max}]$ in a distance less than $D_{\text{brake,max}}(v)$; and so, this assumption prevents this from happening. Assumption 72 ensures that, even if u_k does not maintain a fixed speed, the robot travels farther along any non-braking trajectory than along any braking trajectory starting at the same speed. We conclude with the following remark, that establishes the minimum required planning time horizon T .

Remark 73. For an arbitrary $\zeta_{hi,0} \in Z_{hi,0}$ and $k \in K$, let the robot’s non-braking trajectory be given by (49), and let τ_v be given by (89). Then the planning time horizon T must satisfy

$$T \geq \tau_{\text{plan}} + \tau_v \quad (92)$$

for Assumption 72 to be fulfilled. To see why this is the case, compare the limits of the integral of the non-braking trajectories in (49) and (90).

13 Appendix: Obstacle Representation

We now present a geometric method for finding the maximum penetration distance \bar{b} (Definition 58) for an arbitrary robot footprint X_0 with width \bar{r} (Definition 53).

Lemma 74. Let X_0 be the robot’s footprint at time 0 (as in Definition 3) with width \bar{r} (as in Definition 53). Let $I_{\bar{r}} \subset (X \setminus X_0)$ be a line segment (Definition 41) of length \bar{r} . Let \bar{b} denote the maximum penetration distance of X_0 through $I_{\bar{r}}$ (as in Definition 58). Then, there exists at least one angle of rotation $\theta \in [0, 2\pi)$ for which, if X_0 is rotated by θ , then passed through $I_{\bar{r}}$ by translation only (where passing through is as in Definition 50), X_0 penetrates $I_{\bar{r}}$ by \bar{b} .

Proof. Let $P_{I_{\bar{r}}}$ be the closed half-plane defined by $I_{\bar{r}}$ as in Definition 49. Let $\{R_t\}$ be a transformation family as in Definition 46 such that the penetration of X_0 into $I_{\bar{r}}$ (as in Definition 56) is the number \bar{b} ; such an $\{R_t\}$ exists by Lemma 57. As per Definition 46, every $R_t \in \{R_t\}$ has an associated translation s_t and rotation θ_t , both of which are continuous in t . By [42, Theorem 1], the line segment $R_T X_0 \cap I_{\bar{r}}$ is a chord of $R_T X_0$ (as in Definition 42). By Lemma 61, every chord of $R_T X_0$ that is parallel to $I_{\bar{r}}$ and lies in $P_{I_{\bar{r}}}^C$ is strictly shorter than $I_{\bar{r}}$. Therefore, one can translate $R_T X_0$ “out” of $P_{I_{\bar{r}}}^C$ (i.e., “undo” passing X_0 through $I_{\bar{r}}$), while leaving $R_T X_0$ rotated at the angle θ_T associated with R_T . More precisely, there exists a family $\{s_t\}_{t \geq T}$ of translations such that the set $\{p + s_t \mid p \in R_T X_0\}$ does not intersect the endpoints of $I_{\bar{r}}$ for all $t > T$; otherwise, there exists a chord of $R_T X_0$ that is parallel to $I_{\bar{r}}$ and longer than $I_{\bar{r}}$ that lies in $P_{I_{\bar{r}}}^C$, which contradicts Lemma 61 and the fact that the family $\{R_t\}$ passes X_0 through $I_{\bar{r}}$. So, we can cause X_0 to penetrate through $I_{\bar{r}}$ by the distance \bar{b} by first rotating it to an angle θ_T , then passing it through by translation only. ■

Note that this lemma starts with the penetration distance of \bar{b} and works “backwards.” However, we can find θ_T in a “forward” direction, which we now discuss informally. Assume the premises of Lemma 74, and recall that X_0 cannot pass fully through $I_{\bar{r}}$. Rotate X_0 by an angle $\theta \in [0, 2\pi)$. Next, pass X_0 through $I_{\bar{r}}$ “as far as possible” into $P_{I_{\bar{r}}}^C$ by translation only; this means that both endpoints of $I_{\bar{r}}$ lie in the boundary of the translated X_0 . Consider the following to see why the translated X_0 must contain both endpoints to be translated “as far as possible.” If ∂X_0 does not contain both endpoints of $I_{\bar{r}}$ after translation, then there are two possibilities. In the first case, the translated X_0 contains neither endpoint, so it can be translated farther into $P_{I_{\bar{r}}}^C$. In the second case, the translated X_0 contains one endpoint, in which case it can be translated a small distance towards the other endpoint so that it no longer contains both endpoints, which means that we are back in the first case. This procedure of rotation-then-translation need only be checked for $\theta \in [0, 2\pi)$, and every θ is associated with a finite penetration distance, so at least one θ produces the maximum penetration distance \bar{b} .

14 Appendix: Application

We now present a pair of design choices that can help RTD perform in real time and reduce its conservatism. First, by Theorem 68, safety is guaranteed if obstacles are buffered by a distance $b \in (0, \bar{b})$ (see Definition 39); here, we discuss how to choose b practically. Second, we describe how to apply FRS swapping, introduced in Section 8.1, to pick different trajectory-tracking models (as in (13)) for different initial condition regimes of the high-fidelity model (1).

14.1 Choosing the Buffer Size

As per Theorem 68, the buffer size b must be chosen in $(0, \bar{b})$ for safety. As noted in Section 6 and shown in the simulation results for Experiment 1 in Tables 2 and 3, choosing a larger b increases conservatism because it reduces

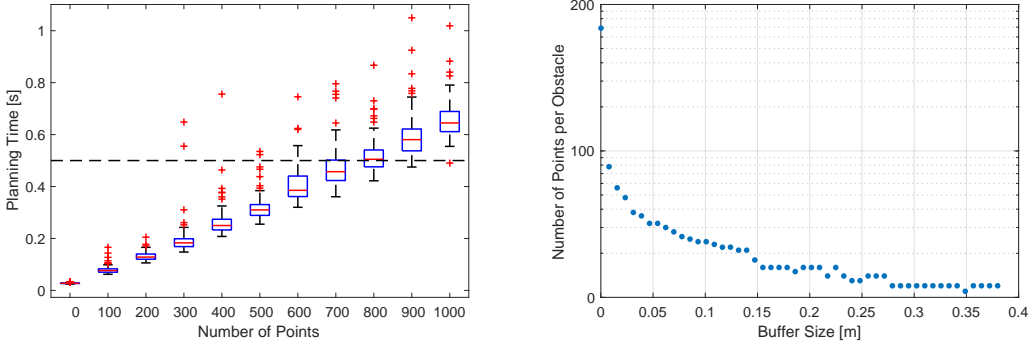


Figure 18: The two-step procedure for choosing the buffer size b for the Segway from Example 7. As shown in the left subplot, increasing the number of points in X_p (i.e. the number of nonlinear constraints) causes the mean planning time to linearly increase ($r^2 = 0.99$); these data come from running MATLAB’s `fmincon` function with randomly uniformly-distributed points to produce nonlinear constraints, with a cost function that is minimized when the Segway reaches a randomly-selected waypoint. For each number of points (i.e., constraints), the box plot shows the mean planning time as a red line, the 25th and 75th percentiles as a blue box, and the maximum and minimum inlier data as the black whiskers; outliers are plotted as red pluses. The Segway’s planning time cutoff $\tau_{\text{plan}} = 0.5$ s is plotted as a dashed black line, showing that the algorithm can tolerate up to 700 constraints while still converging within τ_{plan} on average. The right subplot shows the number of points that are produced as a function of the buffer size $b \in (0, \bar{b})$ for a 0.3×0.3 m² box-shaped obstacle as used in simulation (see Section 9). The points are produced by the `buffer` function (Algorithm 1 Line 7). A buffer size of 0.05 m produces approximately 32 points per obstacle, which would allow the Segway to plan for up to 21 such box obstacles while converging within τ_{plan} .

the amount of free space available for the robot to move through. Here, we show that there is a tradeoff between a smaller b for reduced conservatism versus a larger b for reduced execution time.

Consider Program (78), i.e. `OptK`, which finds optimal trajectory parameters at runtime (see Algorithm 2), and can be implemented with a nonlinear optimization solver. Recall that the planning time is $\tau_{\text{plan}} = \tau_{\text{process}} + \tau_{\text{trajopt}}$ as in Assumption 26, where τ_{trajopt} is used as a cutoff time for the execution of `OptK`. Since τ_{process} is fixed (see Assumption 26), we want to know how τ_{trajopt} changes as a function of b . In other words, we want to understand how long it takes to run `OptK` as b changes.

To do this, first suppose that we have w^l as part of a feasible solution to (D^l) computed for some trajectory-tracking dynamics as in (13), and suppose $J : K \rightarrow \mathbb{R}$ is an arbitrary cost function to be used by `OptK`. From Section 6, recall that obstacles are represented as a finite set of discrete points $X_p \subset X$. We evaluate w^l on each of these points to construct nonlinear constraints for `OptK` as shown in (78). So, the more points there are in X_p , the more nonlinear constraints there are for `OptK`, and, as a consequence, `OptK` takes longer to run.

Now, notice that the number of points in X_p increases as b decreases (see Algorithm 1). What we do here is create a “pretend” X_p by sampling a fixed number of points in X , and then we measure how long it takes `OptK` to run when each of those points is turned into a nonlinear constraint using w^l ; in other words, we find τ_{trajopt} as a function of $|X_p|$ (see the left subfigure in Figure 18). Then, we create an arbitrary polygonal obstacle $X_{\text{obs}} \subset X$ (which obeys Assumption 38), and find how many points are produced in its discretized representation produced by Algorithm 1 as b increases; in other words, we find $|X_p|$ as a function of b (see the right subfigure in Figure 18). Finally, we pick a maximum desired amount of time for τ_{trajopt} , which we associate with a maximum number of points N allowed in X_p ; the number N lets us find the buffer size b that produces X_p such that $|X_p| \leq N$ for our arbitrary polygonal obstacle. Note that the arbitrary polygonal obstacle should be representative of obstacles that the robot is expected to encounter for this procedure to work best; if this kind of information is not available, then one can test a variety of polygons with varying total perimeters, since the larger the perimeter of the obstacle, the more points are created in the discretized representation (to see why, consider the `sample` function used by Algorithm 1).

We now give an example of this generic procedure applied to the Segway.

Example 75. First, compute the FRS using (D^l) with $l = 6$ as described in Section 8.1; this gives us the polynomial w^6 . Recall that the Segway has a circular footprint X_0 . Let $x_{\text{des}} \in (X \setminus X_0)$ be a randomly-selected “waypoint” and let $x_T(k) \in X$ be the end of the Dubins path at time T created by the trajectory-producing model (13); set $J(k) = \|x_{\text{des}} - x_T(k)\|_2^2$ as the cost function for `OptK`. To find the relationship between $|X_p|$ and τ_{trajopt} , we repeat the following

steps 100 times for each $N \in \{100, 200, \dots, 1000\}$.

1. Create a “pretend” X_p by sampling a random set of N points uniformly in $X \setminus X_0$.
2. Solve $\text{Opt}K$ using J as above, with the pretend X_p passed to w^6 to create nonlinear constraints, and do not enforce any time limit on $\text{Opt}K$.
3. Time how long it takes to solve $\text{Opt}K$.

Now, to find the relationship between b and $|X_p|$, create a square obstacle $X_{\text{obs}} \subset X$ with a side length of 0.3 m. Find the numbers \bar{r} (Definition 53) and \bar{b} (Definition 58) for X_0 . Pick a variety of $b \in (0, \bar{b})$; for each b , using Example 67, compute the point spacing r and arc point spacing a . Pass X_{obs} , b , r , and a to Algorithm 1 to produce X_p , and count $|X_p|$. As b varies, $|X_p|$ changes as shown in Figure 18.

Finally, we pick a desired $\tau_{\text{trajopt}} = 0.5$ s. From the left subfigure of Figure 18, if $|X_p| \leq 700$, then $\text{Opt}K$ typically solves in less than or equal to 0.5 s. From the right subfigure of Figure 18, if $b = 0.05$ m, then the single box obstacle produces 32 points; so, choosing $b = 0.05$ m means that $\text{Opt}K$ can solve within 0.5 s when considering up to $|X_p|/N = 700/32 \approx 21$ square obstacles in a single planning iteration.

14.2 FRS Swapping

In applications with large spaces of initial conditions and parameterized trajectories, it is useful to compute separate FRS’s corresponding to different regions of the parameter space, K , or different sets of initial conditions. Then, at runtime, the trajectory optimization can choose whether to swap to a different FRS depending on the current state, or the previous state evolution. The benefit of FRS’s spanning different ranges of initial conditions is that, for each FRS, we can compute a different tracking error function g ; we find in practice that the magnitude of g is smaller over a smaller range of initial conditions, resulting in a less conservative FRS for each range of initial conditions. Note that FRS swapping does not affect the safety guarantee when planning with any one of multiple FRS’s, because each FRS ensures safety by itself. However, for FRS swapping, the swapping criteria and tracking error functions g must ensure that, if swapping to a different FRS, the initial conditions of the robot are accounted for in that FRS.

For the Segway application discussed in this paper, we found that it is useful to compute one FRS with a max speed of 1.25 m/s, and one with a max speed of 0.5 m/s. The magnitude of the error function, g , is reduced for the low-speed FRS, due to the decreased range of initial conditions, as shown in Figure 20. Note the high-speed FRS contains all initial conditions in the low-speed FRS; this means that the low-speed FRS is a subset of the high-speed FRS. So, we can use the high-speed FRS alone for planning, but swapping to the low-speed FRS when the robot is traveling slowly enables us to reduce conservatism. See Figure 19 for contours of the low- and high-speed FRS’s, and note how the low-speed FRS is smaller for the same initial condition and commanded trajectory. We present the low- and high-speed error functions in the following example.

Example 76. Consider the Segway’s trajectory-tracking model in Example 13. When $v_{\text{max}} = 1.25$ m/s, then the tracking error function (shown in Figure 3) is:

$$\begin{aligned} g_x(t) &= -1.5835t^3 + 3.9683t^2 - 3.4832t + 1.2511 \\ g_y(t) &= -1.0455t^4 + 2.4518t^3 - 2.1804t^2 + 0.9514t + 0.0223. \end{aligned} \tag{93}$$

When $v_{\text{max}} = 0.5$ m/s, the tracking error function is:

$$\begin{aligned} g_x(t) &= -0.6169t^3 + 1.5444t^2 - 1.3628t + 0.5000 \\ g_y(t) &= -0.3506t^4 + 0.8339t^3 - 0.7747t^2 + 0.3655t + 0.0097. \end{aligned} \tag{94}$$

We now present the logic for swapping between high- and low-speed FRS’s using thresholds. For example, on the Segway described in Section 8.1, we use velocity thresholds η_{up} and η_{down} , and store a moving average of the robot’s velocity, μ_v over the past τ seconds, to perform FRS swapping as follows. After Line 10 in Algorithm 2, we check the following two conditions:

1. If we are planning with the low-speed FRS and $\mu_v \geq \eta_{\text{up}}$, switch to the high-speed FRS.
2. If we are planning with the high-speed FRS and $\mu_v \leq \eta_{\text{down}}$, switch to the low-speed FRS.

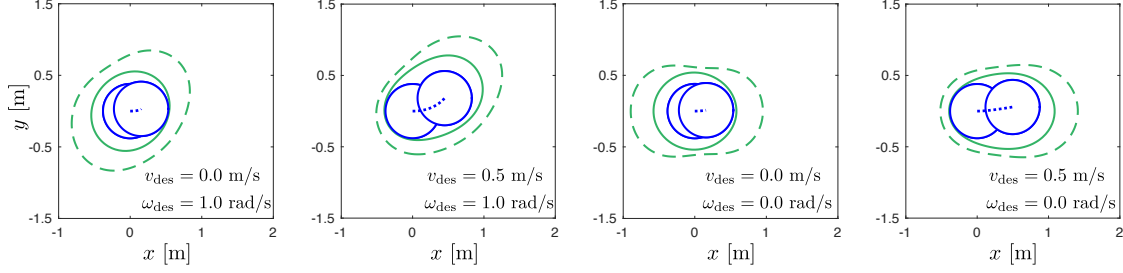


Figure 19: Example trajectories and the corresponding low- and high-speed FRS's for the Segway. The low-speed (resp. high-speed) FRS has a maximum speed of 0.5 m/s (resp. 1.25 m/s). For all of the plots, the Segway's high-fidelity model begins at the initial condition $[x, y, \theta, \omega, v]^T = [0 \text{ m}, 0 \text{ m}, 0 \text{ rad}, 0.5 \text{ rad/s}, 0.5 \text{ m/s}]^T$. The blue circles are the initial condition and final state of the Segway after following each commanded trajectory. The blue dotted line is the trajectory of the Segway's center of mass. The solid green contour is the FRS slice for the low-speed FRS, and the dashed green contour is for the high-speed FRS. Notice that the low-speed FRS contours lie fully inside the high-speed FRS contours while still encompassing the trajectory for the entire Segway footprint, showing that the low-speed FRS is less conservative than the high-speed FRS.

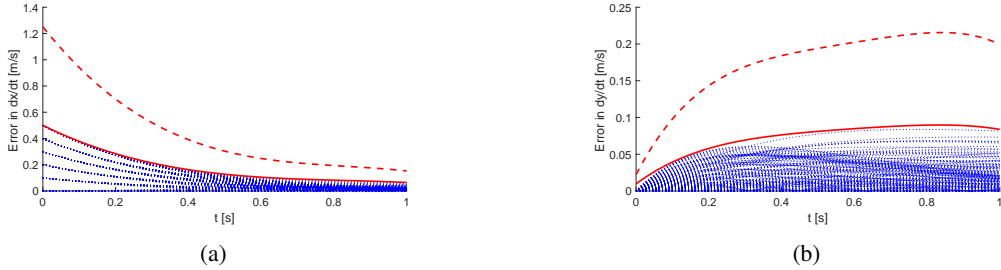


Figure 20: Tracking error in \dot{x} (Subfigure (a)) and \dot{y} (Subfigure (b)) of the Segway's dynamics (4) when tracking Dubins paths as in Example 13, with a max yaw rate $\omega = 1 \text{ rad/s}$ and a max speed $v = 0.5 \text{ m/s}$; the initial conditions are limited to the low-speed FRS. Error is the expression $|f_{hi,i}(t, \zeta_{hi}, u_k(t, \zeta_{hi})) - f_i(t, \zeta, k)|$ in Assumption 10; where i selects the x and y components of ζ_{hi} and ζ . The blue dashed lines are example error trajectories created by sampling possible initial conditions. The solid red lines are the functions g_x and g_y as in (94) in each dimension, which bounds all of the error trajectories from low-speed initial conditions. For comparison, the dashed red lines are the fitted error function for the high-speed FRS (see Figure 3 and (93)). Notice that the tracking error is larger for the high-speed FRS.

If η_{down} is less than or equal to the top speed of the low-speed FRS and initial conditions with velocity equal to η_{up} are captured by the error function for the high-speed FRS, then safety is preserved when we swap to the other FRS. The thresholds and the window length τ of the moving average are determined empirically. For the Segway, $\tau = 1.5 \text{ s}$, $\eta_{\text{up}} = 0.45 \text{ m/s}$, and $\eta_{\text{down}} = 0.1 \text{ m/s}$.